Mechanical Properties of Layer-by-Layer Assembled Thin Film Nano-Composites Using Brillouin Light Scattering

by
Lang Sui

A dissertation submitted in partial fulfillment
of the requirements for the degree of
Doctor of Philosophy
(Materials Science and Engineering)
in The University of Michigan
2011

Doctoral Committee:

Professor John Kieffer, Chair
Professor Peter F. Green
Professor Nicholas A. Kotov at to
Associate Professor Jinsang Kim

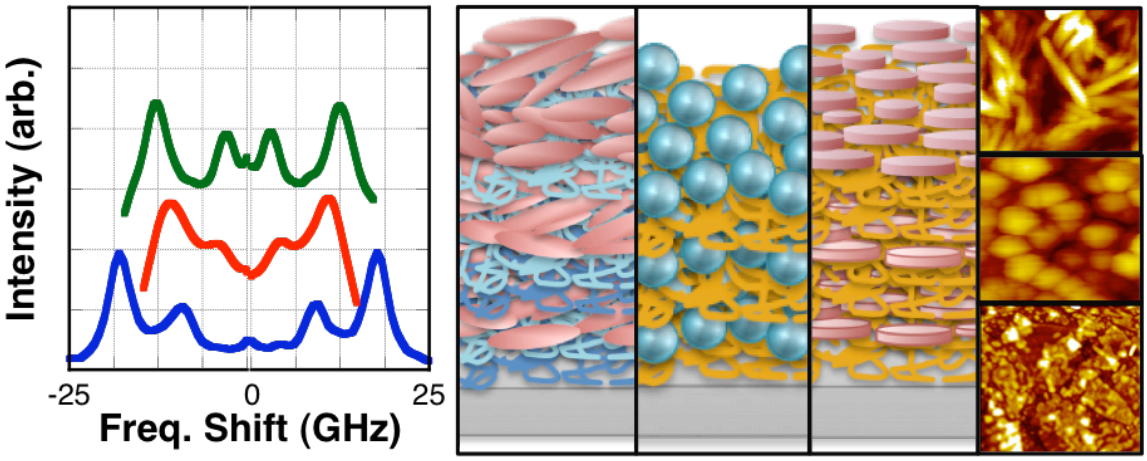
Intensity (arb.)
-25
0
25
Freq. Shift (GHz)

DEDICATION

我的爸爸妈妈

－ 朗朗

My mom and dad

- Lang

ACKNOWLEDGEMENTS

First and foremost I would like to than my advisor, Professor John Kieffer, who I've known since my undergraduate days here at Michigan. Over the years, he has provided me with countless guidance and encouragements on my work as a graduate student. I feel fortunate to have him as my thesis advisor and friend. I also appreciate the advice and assistance I have received from the members of my committee: Prof. Nicholas Kotov, Prof. Peter Green, and Prof. Jinsang Kim. Prof. Kotov, especially, was extremely generous in allowing me to use his facilities.

Over the years of my Ph. D career, I have worked with a number of intellectually stimulating and helpful individuals who have made the process of getting a Ph. D more manageable. Particularly the experimentalists in my group: Arthur, Prof. Liping Huang, Michael and Gerri, as well as Paul, Bongsup, Jian, Ming and Huanan from Prof. Kotov's group and finally Amit and Keqin from Prof. Arruda's group. I would also like to thank my friends I have made over the years, old and new; above all, Kate, Shen, and Stephen who've stuck with me through all these years. Finally, I would like to thank my parents and Andy, your support has meant so much to me.

TABLE OF CONTENTS

LIST OF FIGURES

LIST OF TABLES

ABSTRACT

Recently there has been a surge of interest in layer-by-layer (LBL) assembled thin films for a variety of applications, ranging from high-strength materials to multi-functional composites. In contrast to traditional composites, in which reinforcing particles are incorporated spatially homogeneously into a polymeric matrix, LBL assembled composites are distinct because of their stratified structure, the precise positioning of reinforcing element in at least one dimension, and the nanoscopic size of these particles. Thin films with very high particle loading have been assembled using this technique, leaving only thin polymer layers to provide cohesiveness. Despite the strong interest in LBL materials, the relationship between structure and mechanical properties is poorly understood. To tackle this issue, we studied the mechanical properties of LBL films using Brillouin light scattering (BLS).

This dissertation addresses how variations in the particle-matrix interface, particle size, geometry, and volume fraction affect the mechanical properties of LBL assembled thin film materials. Films are primarily assembled using the linear-growth LBL method, which results in a layered structure with distinct interfaces. Particles with rod-like, sphere-like and plate-like geometries are incorporated in between polymer layers at various volume fractions. The volume fraction is adjusted by using different polymers and precursors with variable polymer concentration. In addition, one set of films is assembled using exponentially grown LBL, which results in the formation of diffuse

interfaces, to study the role of interface definition. In these films, fumed silica aggregates are added during deposition to mark the location of the original interfaces.

In LBL composites with rod-shaped nano-fillers, the in-plane elastic modulus increases continuously as a function of particle loading, whereas the out-of-plane modulus tails off or even reaches a maximum. The decrease in rigidity in this direction is due to the lack of continuous wetting of fibers by the polymer. Incorporation of spherical fillers results in a larger out-of-plane than in-plane modulus, which is due to the more effective particle-polymer-particle connections and load transfer as a direct consequence of the deposition process. Porosity in these films affects the in-plane Load transmission more prominently. For LBL nano-composites with plate-like particles, the beneficial effect of adding reinforcing particles tapers off because of the transmission of shear forces between particles becomes less efficient with thinner polymer layers. In the latter, structural relaxation occurs more rapidly and they respond more compliantly as a result. Diffuse interface between LBL layers result in the orientation of polymer chains in the film growth direction. As a result, the out-of-plane elastic modulus is higher than the in-plane modulus, and transport of small molecules across layers is facilitated. Addition of nano-particles neither improves nor deteriorates mechanical properties in these films.

This work is the first of its kind to provide these new insights into the mechanics of layered thin films.

CHAPTER 1

Background and Introduction

1.1 Motivation and Project Overview

The concept of composites has long been pursued as a way to combine the best characteristics of several materials into one, and thus create a amalgam whose properties are superior to those of any of its constituents taken individually. Recently, fabrication techniques shift away from large scale mixing and instead focus more on building up structures from micro- or nano-scale structural units. Layer-by-layer (LBL) assembly is such a refined manufacturing technique. The description of the mechanical properties of materials with nano-scale features models that differ from those that govern conventional bulk composites. These nanocomposites differ significantly from materials with larger-scale heterogeneities, not only because of the superbly controlled placement of reinforcing particles within a stratified matrix, but also because of the strong interactions between the matrix and filler. In order to fabricate stronger and more stable LBL films, we need to understand how the processing parameters, such as solution chemistry, conditions during deposition, and post-deposition chemical and thermal treatments, affect their mechanical properties. However, despite the recent surge of interest in LBL

assembled films, a detailed understanding of how deposition conditions affect the structural stability and mechanical properties of such films is still lacking.[1,2]

One reason for this lack of knowledge may be the difficulties associated with probing the mechanical response of LBL assembled materials truly at the pertinent length scales. In this respect, Brillouin light scattering (BLS) is an effective method for measuring the elastic constants of thin films and multilayered thin films. In fact, this method provides some unique advantages that are particularly useful for probing the adhesion between individual layers of LBL assembled films. BLS results from the interactions between light and propagating thermal phonons. Analysis of the spectrum of scattered light reveals the complex elastic modulus of the scattering medium. Although sampling of scattering events is done over volumes of several μm^3, in terms of the elastic modulus, the experiment is equivalent to the cyclic tensile testing of a specimen that measures ~50 nm in length. The direction of this deformation can be chosen to be either parallel or perpendicular to the interface between layers. The loss modulus derived from this measurement reveals the amount of energy dissipated in the aperiodic motions of molecular building blocks. Finally, the measurement of mechanical properties is done without mechanical contact and The amount of energy exchanged between elastic and electromagnetic waves is so minute that the sample can be considered in thermodynamic equilibrium at all times. The characteristics of our principal measurement technique allowed us to explore nano-composites in an unprecedented way.

Based on this technique we carried out a systematic investigation of LBL nano-composites in which the principal experimental variables are:

- the shape and size of the reinforcing nano-particle

- ❖ the strength of adhesion between embedded particle and polymer matrix
- ❖ the relaxational response of the polymer matrix, and
- ❖ the definition of the interfaces between adjacent layers.

1.2 Composite and Nanocomposites Systems

A composite can be described as combination of two mechanically and chemically different materials, i.e., a fiber embedded in a polymer matrix. Composites can exist both in natural in the forms of bone, mollusk shells and wood, or synthetic derived. Engineered composites range from the more primitive bricks made of mud and straw to ultra and lightweight epoxy based carbon fiber composites.[3] The basic concept of engineered composites is establish a combination of properties that is not present in any single material. Modern composites can be divided into metal matrix composites, ceramic matrix composites, and polymer matrix composites. These synthetic composite materials are made by mixing or blending two or more distinct constituents together, as a result of this mixing, their mechanical behavior typically deviate from each of the constituents. Stiffness of these materials can vary because of a number of factors, some of which include the stiffness of the matrix and filler, geometric and the spatial arrangement of the filler material(s).[3,4] In many cases, the longitudinal and transverse modulus can be described using the idea of springs in parallel and in series, respectively, along with the rules of mixture.[3] Earlier works expanded upon these equations, most famously by Halpin, Tsai,[3] Voigt, Reuss,[5,6] Cox,[7] and Krenchel,[8] to account for filler length and orientation.

1.2.1 Effects of Particle Geometry and Interfaces

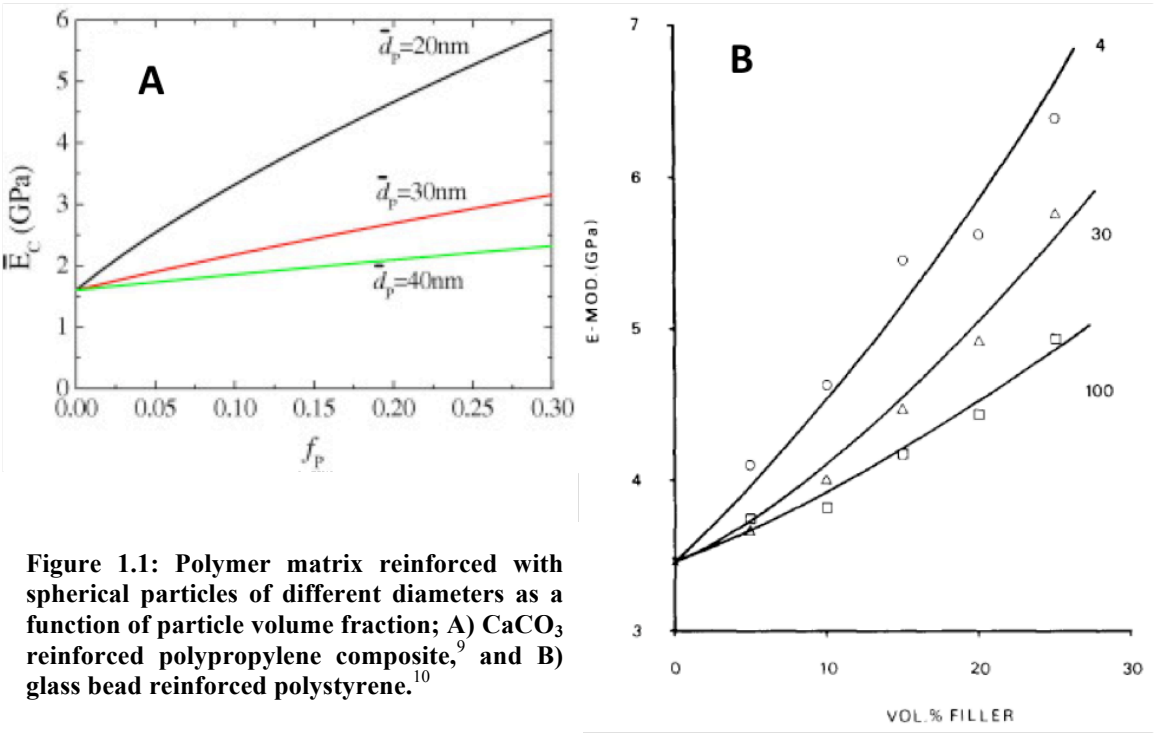

Figure 1.1: Polymer matrix reinforced with spherical particles of different diameters as a function of particle volume fraction; A) $CaCO_3$ reinforced polypropylene composite,[9] and B) glass bead reinforced polystyrene.[10]

The effect of particle geometry in composite materials and the fiber-matrix interface have been a point of interest long before the advent of nanocomposites. The performance of the composite can be described by the ability of the reinforcement phase to bear load, which in turn is determined by the effectiveness of load transfer between the matrix and the reinforcement agent. Therefore, the geometry of the filler material is of particular interest.[11-13] The effect of particle geometry on the longitudinal stiffness of the composite has been studied extensively.[9-26] Typically the reinforcement material are fibrous,[11-13,27-32] platelet,[11,15,16,22,24,33,34] spherical,[9-13,17,19,26,35] or irregular in shape, they can be arranged either randomly or preferentially aligned within a matrix. Figures 1.1 – 1.3 are examples of the effect of the volume fraction of reinforcement agent on longitudinal stiffness for the various type of filler geometry. While it is evident that the stiffness increases with

increasing amount of filler material, the effect is not limited to filler concentration; other parameters such as particle size and geometry also have pronounced effect on the stiffness as well. The typical trend is that the stiffness of the composite is proportional to fiber length and inversely proportional to disc and sphere diameters.[11-13] Furthermore, a thicker interfacial region also helps improve the stiffness of the material as shown in Figure 1.3A-C.[11]

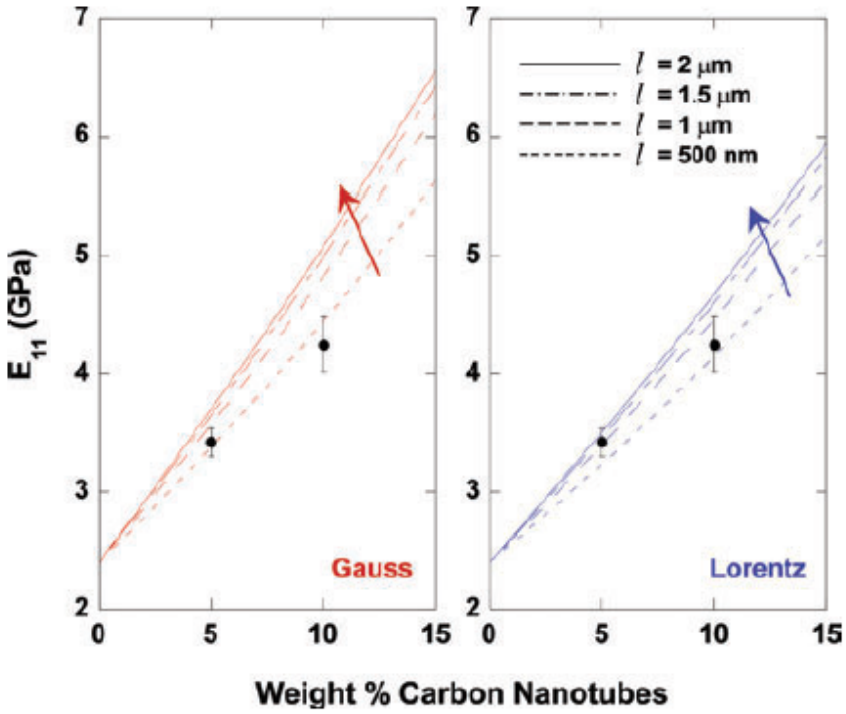

Figure 1.2: Young's modulus of carbon nanotube composites as a function of carbon nanotube concentration.[32]

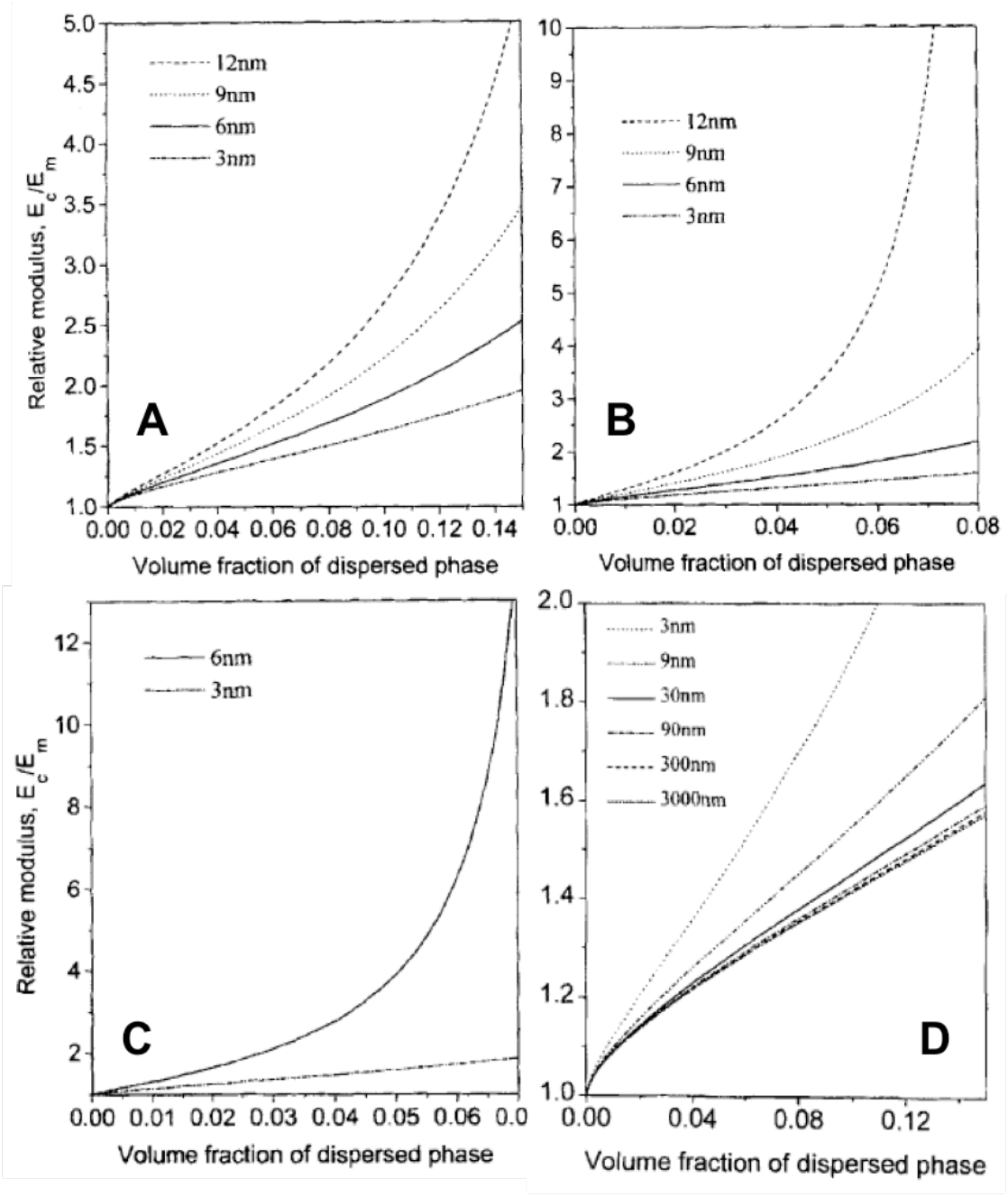

Figure 1.3: Relative modulus for A) fiber, B) plate, and C) sphere based composites where the length parameter refers to the thickness of the interfacial region for particles with radial size of 3 nm; D) relative modulus as a function of volume fraction for plate-like particles.[11]

However, with the contemporary need for smaller and more portable devices as well as the ability to tailor layers down to nanometers in scale, the traditional sense of the composite materials and their stiffness have also taken on a new delineation. Recently

developed materials processing techniques allow one to create structural modulation at the nano-scale. Currently, several method are used to fabricate ultrathin nanocomposite films, namely self-assembled monolayer (SAM),[36-38] Langmuir-Blodgett (LB),[39-41] and LBL self assembly.[16,21,22,42-49] While there are advantages to each of the three techniques, for assembly of thin, multilayer films, LBL offers additional flexibility over SAM and LB. Specifically, the layer-by-layer technique provides the means to fabricate thin polymer films containing nano- to micro-scale fibers. Films can be produced with controlled composition and high fiber loading.[21,44,45]

1.3 Layer-by-Layer Assembly

Decher introduced layer-by-layer assembly in the 90s as a more flexible alternative to the Langmuir-Blogett technique.[42] Through LBL, one is capable of manipulating composite structures down to the single-molecular layer. Initial work by Decher showed the pairing of long chained polyelectrolyte with a polymer electrolyte of the opposite charge can create layered thin films,[42] since then, LBL has become a popular method for assembling composite thin films. These later experiments demonstrated that a diverse number of combinations can be created using both organic and inorganic "fillers"; some of the most common ones include the pairing of long chained polyelectrolyte with clay platelet,[16,22,23,33,34,50,51] nanofibers or tubes,[12,21,22,45,46,48,49,52] spherical colloids,[12,26,33,43,44,53-58] virus,[59-61] and protein.[43,47,62,63] LBL assembly can be employed to an extensive number of practical applications, ranging from phononic crystals[54] to biosensors.[52]

The most common type of LBL film assembly is through deposition of oppositely charged polyelectrolyte or colloids; in the case of strongly charged electrolytes, films build up is typically proportional to the lateral dimensions of the incorporated polymer or particles, this type of assembly is dubbed linearly grown LBL or *l*-LBL. Alternatively, if a strongly charged electrolyte is exposed to weakly charged polyelectrolyte or two weakly charged polyelectrolytes are used, an "exponential" build up of polymer occurs. The rate of film growth is extremely fast compared to the lateral dimensions of the constituents used where the rate typically accelerates with the number of bilayers deposited. The thickness as a function of number of layers or bilayers, however, does not necessarily follow a truly exponential curve. While the use of "exponential" here is somewhat of a misnomer, nevertheless, "exponentially" grown LBL or *e*-LBL, is still the most common nomenclature for this type of mechanism. In this dissertation, *l*-LBL will generally be referred to as LBL unless otherwise indicated, and exponential LBL will follow conventions of *e*-LBL.

1.3.1 Linear Growth Layer-by-Layer Assembly

Linear growth LBL typically involves deposition of strongly charged polyelectrolyte on to a substrate surface. Figure 1.4 illustrates a film buildup process involving a polymer electrolyte and a colloidal electrolyte; in Figure 1.4, the substrate is first exposed to a positively charged polymer solution for an allotted time, followed by rinsing with deionized water or a solvent and drying using compressed air or nitrogen, then the same substrate is exposed or dipped into a second solution of negatively charged colloids for a similar allotted time followed by rinsing and drying. These steps can be repeated until

the desired thickness is achieved, films can be as thin as a couple of nanometers (after 2 layers of polymer deposition) or several microns.

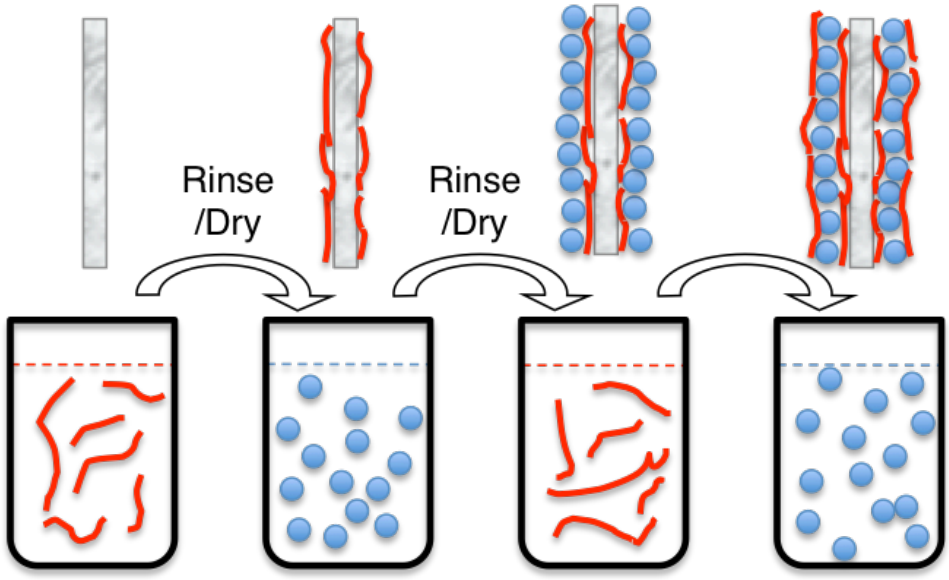

Figure 1.4: Linear growth layer-by-layer assembly process; red polyelectrolyte indicates positively charged polymer solution and blue spherical colloids indicates negatively charged colloid solution.

The principle behind LBL is relatively simple, film build up depends on the electrostatic attraction of oppositely charged polymer or particle: the first layer of the film deposits because of the attraction between the positively charged polymer and the negative surface charge of the substrate. Once complete coverage of the substrate is achieved, the newly positively charged surface layer repeals further adsorption. Rinsing and drying allows for excessive or weakly bonded polymer to be washed away and reduces the roughness of the film, leaving a layer of positively charged polymer on top of the substrate. The deposition of the second layer occurs in a similar manner. Now the negatively charged polyelectrolyte or colloid is attracted to the positively charged polymer layer, and a new negative colloid layer is formed on top of the polymer layer. Likewise, after total coverage of the surface the negatively charged colloid layer repels

further attachment of colloids. Therefore, only a single layer of each constituent is deposited, and the film layer thickness depends largely on the radial dimensions of the polymer and colloid. As a result, the final film structure consists of discreet layers and multiple interfaces between layers.

1.3.2 Exponential Growth Layer-by-Layer

An alternative to linearly grown LBL system is exponential growth LBL; unlike *l*-LBL, *e*-LBL allows films to grow at a much faster rate. Similar to *l*-LBL, the method involves two or more polymers or particles to be repeatedly deposited on top of a substrate surface; however, the deposition mechanism is substantially different. The commonly accepted theory behind the main driving force for *e*-LBL is through diffusion of polymer into previously deposited layer.[20,64] For simplicity sake, we will consider the case of two weakly charged polymers, A and B. Figure 1.5 illustrates the diffusion mechanism for *e*-LBL. Following the deposition of the first layer A, the substrate is dipped into the second polyelectrolyte solution B, because of weak electrostatic charge of polymer A, the first layer swells while the substrate is in solution B. The swollen layer allows for the diffusion of polymer B into polymer A, Figure 1.5-*2*, and this produces a blended layer of A and B polymers where the top layer is predominately polymer B, Figure 1.5-*3*. As this substrate is placed back into solution A, Figure 1.5-*4*, the film swells once again, allowing for polymer A to diffuse into the. Therefore, because each deposition step involves the diffusion of large amounts of polymer, the repetitive dipping of the substrate into solutions A and B produces relatively thick films with few deposition layers. In addition, the resulting structure is relatively homogenous as compared to the discreet interfaces of *l*-LBL, Figure 1.5-*5*. Deposition requires one or more weakly

charged polymer(s), in the case where only one weakly charged polymer is present, the strongly charged constituent does not diffuse.

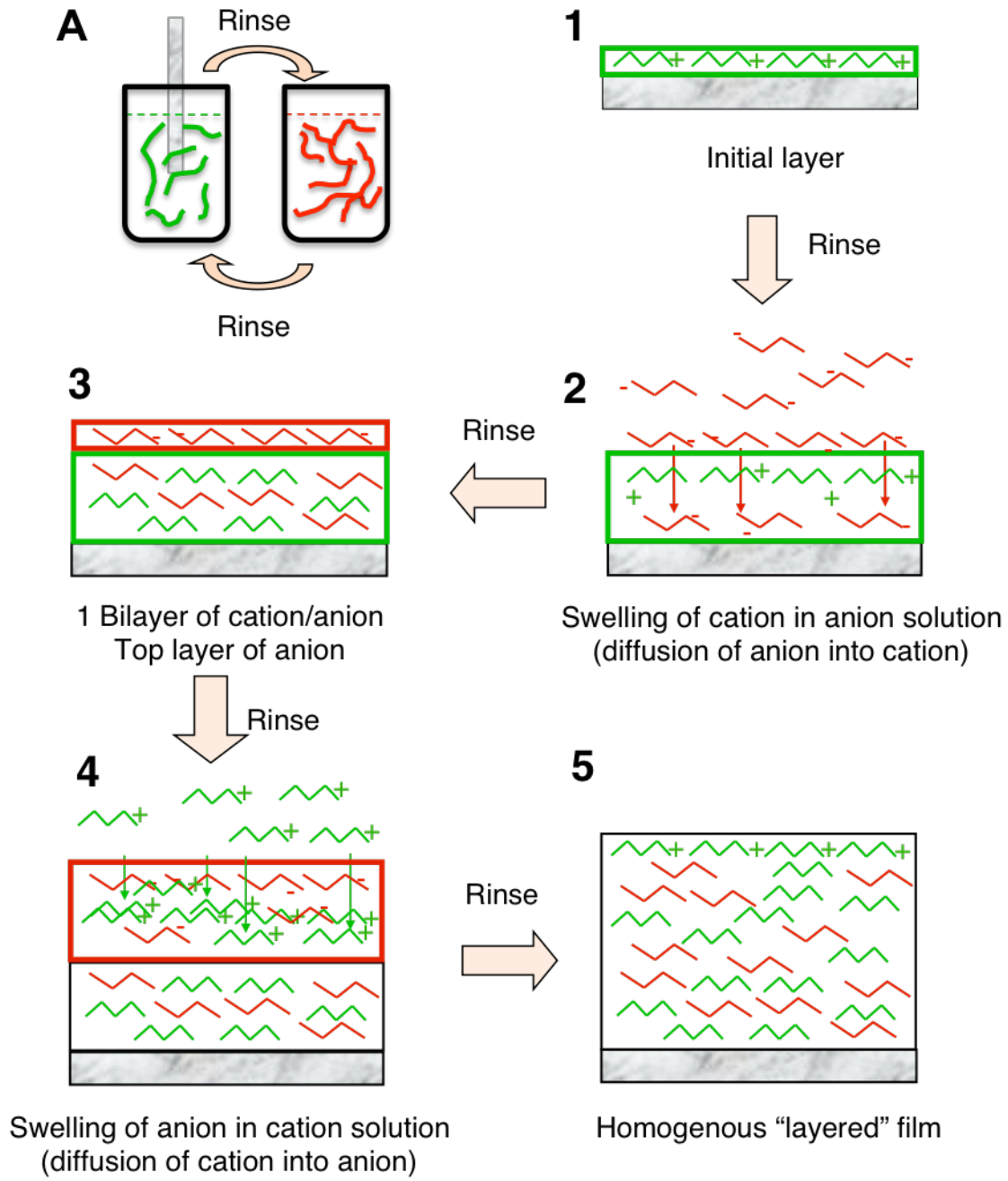

Figure 1.5: Basic deposition procedure of two different solutions onto a substrate; 1 - 5: diffusion mechanism of weakly charged polyelectrolytes for *e*-LBL.

1.3.3 Deposition Parameters and Variations

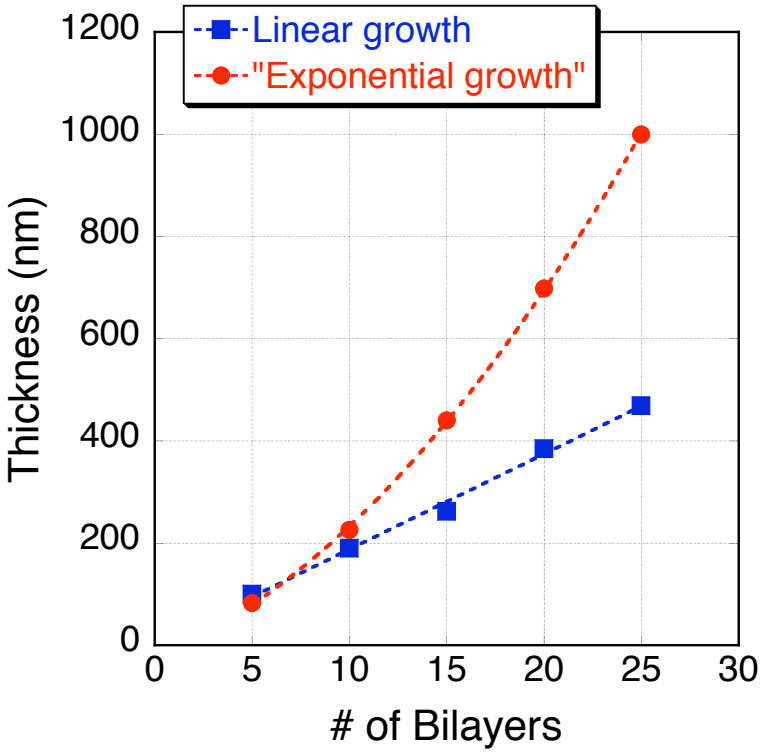

Figure 1.6: Film thickness vs. number of bilayers for linear (PDDA/cellulose) and exponentially (PDDA/PAA) grown films; films were grown on Si wafers and characterized using ellipsometry.

Figure 1.6 is an example of film thickness as a function of number of bilayers, for linear and exponential grown LBL films of PDDA/cellulose nanocrystal and PDDA/PAA, respectively, where PDDA and PAA are poly(dimethyldiallylammonium) and poly(acrylic acid). The initial growth at 5 and 10 bilayers show similar film thicknesses, however further depositions showed that the growth rate of exponentially grown films is much faster than that of linear grown films; after 25 bilayers the thickness of the *e*-LBL film is more than twice the amount of *l*-LBL film. The thickness vs. number of bilayer data for the *e*-LBL shows the positive curvature that led to coining the term "exponential" growth. The structures of *l*-LBL and *e*-LBL assembled films are typically characterized using scanning electron and confocal scanning microscopy, as seen in Figures 1.7 and 1.8. The layered stratus of *l*-LBL assembled is apparent in Figure

1.7A, while no clear interfaces can be seen for *e*-LBL assembled film (Figure 1.7B).[22,23] Also for similar number of bilayers, the *e*-LBL grown film is more than 10 times the thickness of *l*-LBL. The structure of *e*-LBL assembled films can also be seen using confocal laser scanning microscopy imaging of fluorescence-labeled chitosan/hyaluronan deposited as shown in Figure 1.8. In this case, the last deposition layer of weakly charged chitosan and strongly charged hyaluronan are tagged with green and red dyes, respectively.[64] It is evident that chitosan (green) diffused through the entire cross-section of the film, while hyaluronan (red) remained at the top layer of the film.

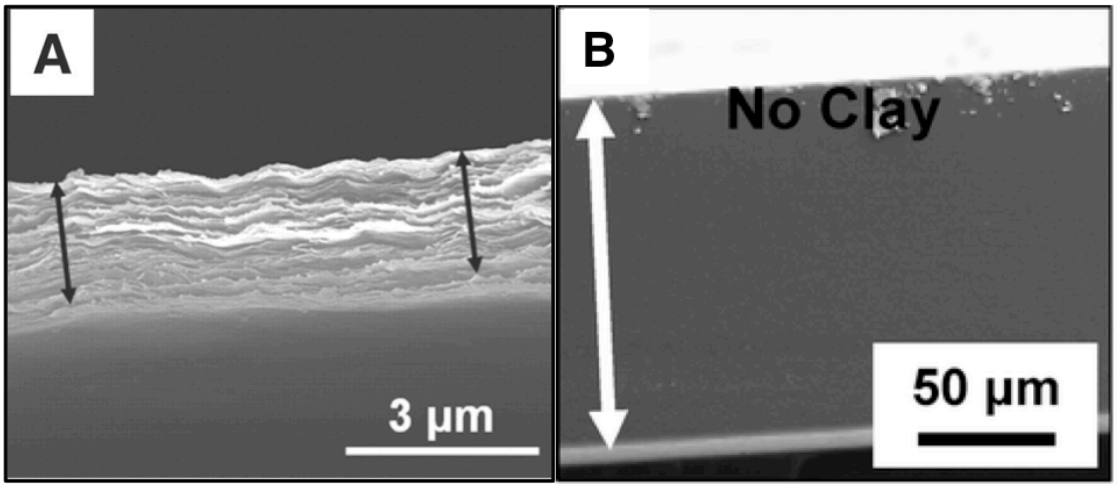

Figure 1.7: Scanning electron microscopy image of A) 300 bilayers of *l*-LBL assembled poly(vinyl alcohol)/clay;[22] B) 200 bilayers of *e*-LBL grown poly(ethyleneimine)/poly(acrylic acid);).[23] the arrows indicate the thickness of the films.

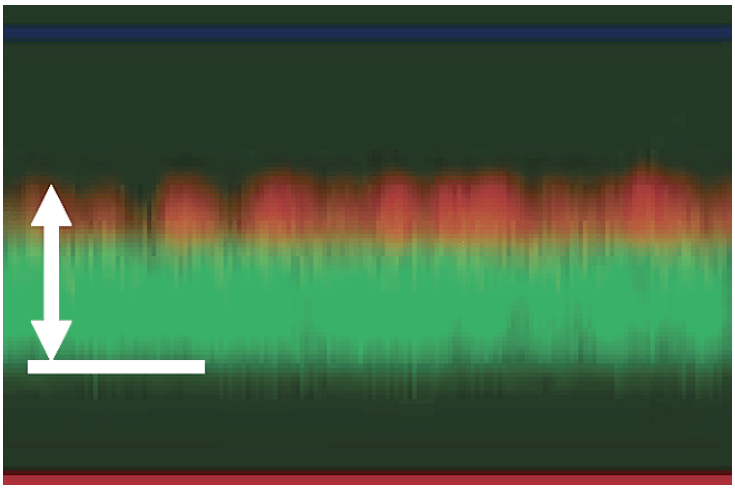

Figure 1.8: Confocal Scanning Microscopy image of [chitosan/hyaluronan]$_{36}$ where layer 36 of chitosan and hyaluronan are tagged with green and red florescent dyes, respectively; arrow and bar indicates 2.4 µm.[64]

Film morphology is most frequently changed by using different types of polymers and colloids. However, many other parameters can be varied in LBL fabrication in order to fine tune features of the film. As mentioned earlier, different types of polyelectrolytes can be used along with various types of suspended colloids. Variations in deposition parameters include deposition time, solution concentration and pH,[20,64,65] addition of salt or other solvents,[49,64] and rinsing agent,[66,67] are some common methods used to change the resulting film structure in terms of thickness or roughness. In addition, more complicated structures can be manufactured using different combinations of electrolyte layering,[68,69] coating of nanoparticles,[43] and patterning.[70] Fabrication style typically involve hand dipping or machine dipping of substrate into a deposition solution,[22,42,65,71] spinning[72-74] and spray[75,76] coating have also been studied.

1.3.4 Material Selection and Applications

To study the geometric effect of fiber, disc or sphere-like particles in LBL assembled nanocomposites, we chose cellulose nanocrystals (fiber), montmorillonite (MTM) clay (disc), and silica nanoparticles (sphere); in addition, fumed silica was used to study the effect of particle aggregates. The reasoning behind these material selections was in part economical – all four materials are readily available at very low cost, but they also belong to a class of materials that are commonly used in composite manufacturing.[26,27,34,51,77-83]

Cellulose and MTM clay composites are particularly of interest in the area of bio-inspired materials. The structures of the crystalline portion of cotton cellulose and a layer of MTM clay can be seen in Figure 1.9A and B. Cellulose is a low-density polysaccharide biopolymer typically found in plant walls, such as wood or cotton. A fibril of cellulose is composed of crystalline regions separated by amorphous layers. During hydrolysis, the amorphous regions are burnt off to create fiber-like cellulose nanocrystals. Depending on the source of cellulose, the aspect ratio may range from 40 to over 1000. Similarly, montmorillonite clay has a large aspect ratio as well, but the structure of MTM clay resembles stacked thin sheets separated d-spacings of variable distance.[16,34,80] In water, these sheets or plates can be partially or completely "exfoliated" to reveal a few or individual clay sheets. With an increase in environmental awareness, natural fiber reinforced composites appear to be an interesting candidate in replacing traditional glass, carbon or aramid fiber composites. Currently, biofillers have already been used in the automotive industry; other transportation industries such as railways, aircraft and irrigation, along with furniture and leisure items are some potential applicants researching the use of biopolymers as filler material.[77,79] MTM clay have recently been

used to mimic ultrastrong structures found in nature, such as the laminar stacking of organic and inorganic materials in nacre as seen in Figure 1.10.

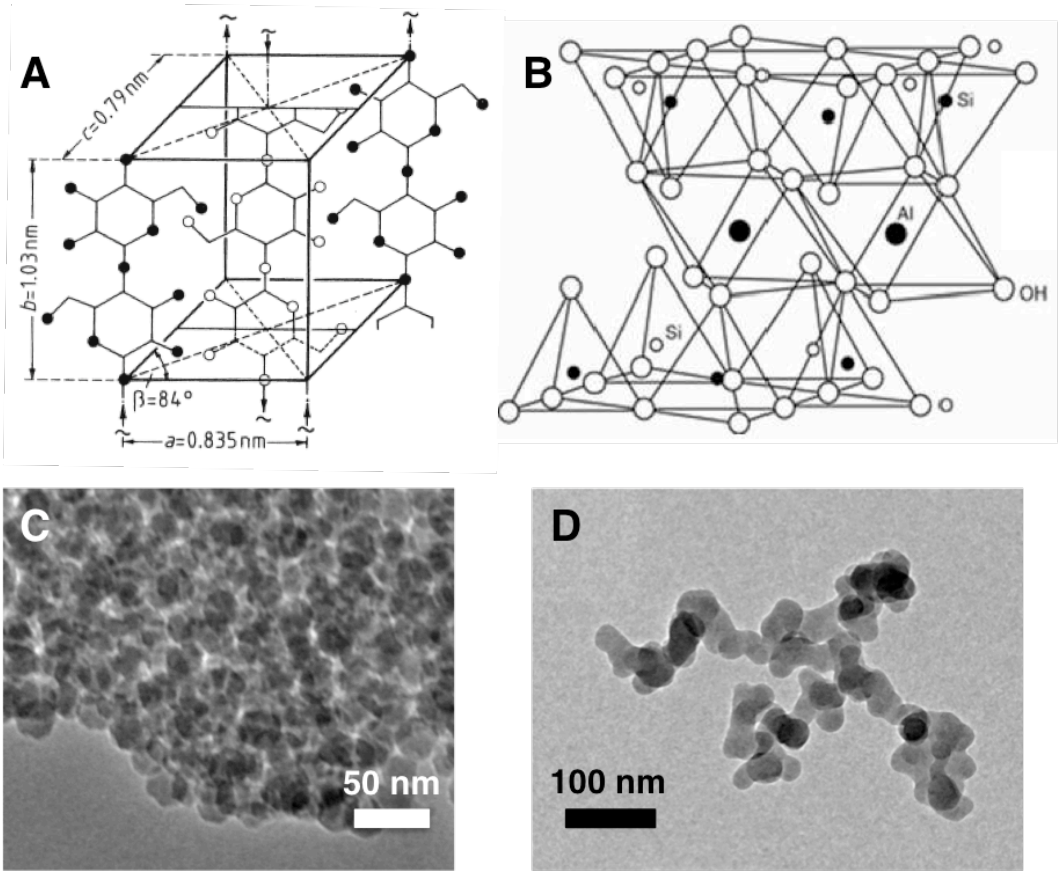

Figure 1.9: A – B) Structures of crystalline portion of cotton cellulose and layered silicate;[4,80] C – D) TEM images of silica nanoparticles and fumed silica.[84]

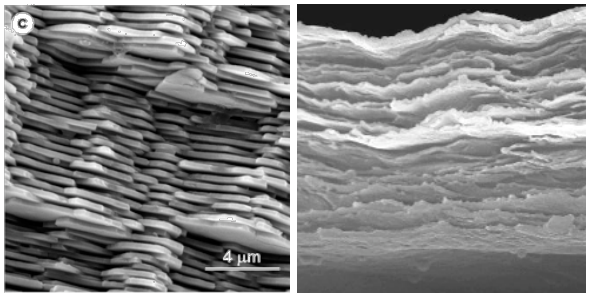

Figure 1.10: Layered structure of aragonite and clay platelets from cross sections of nacre[85] (right) and PVA/MTM clay (left), [22] respectively.

While composites are perhaps best known in the context of structural materials, e.g., to reduce material density without comprising its mechanical strength, nanocomposites can be used in a variety of applications for which mechanical properties are of secondary importance. For example, spherical nanoparticles based composites have been utilized as bio/mechanical-sensors,[86,87] photonic and phononic crystals,[54,88] anti-reflective (AR) coatings,[82,89,90] nanoparticle templating[68,70] and superhydrophobic films.[82] Similarly, fumed silica can be potentially used as ion-conducting electrolytic membrane,[78,91,92] automotive coatings, and to improve polymer rheology and strength.[77,93] Although the goal of many of these products is not to create extra strong and low-weight materials, their mechanical properties are still important for their intended use, particularly in the case of coatings and structural reinforcement. Figure 1.9C and D are examples of nano-particulate and amorphous silica structures, respectively.

1.4 Inelastic Light Scattering

1.4.1 Brillouin Scattering

For LBL nanocomposites, structural features are manifest at the micro to nano-scale, i.e., the characteristic spacing between disparate phases is of the order of micro or nanometers. The structural design and the optimization of the processing conditions for such nano-composites calls for techniques of investigation that allow one to characterize structural and mechanical properties at the molecular level. Therefore the need to characterize the structural and mechanical impact of nano-scale interfaces is of particular interest. Léon Brillouin first described the phenomenon of inelastic scattering of light from propagating phonons in matter in 1922.[94] The phenomenon arises when light is

scattered by condensed matter as a result of spatial fluctuations in the refractive index, which in a first approximation can be mapped to density fluctuations. Thus, the plane wave deformations associated with acoustic phonons not only provides for scattering, but as a result of their periodicity they also establish diffraction conditions that allow one to identify the phonon propagation direction from the scattering geometry. Furthermore, the propagation of the density waves causes inelastic scattering events that result in the frequency of the scattered light to be slightly different from that of the incident light, in a manner similar to Doppler shifts. This frequency shift in the scattered light can be directly related to the velocity of sound, and consequently, to the elastic properties of the material.

This technique has traditionally been used to determine the viscoelastic properties of condensed materials. Some of the most common BLS experiments involve determining a set of elastic constants of transparent inorganic compounds and semiconductor thin films,[54,95-100] or measuring the viscosity and glass transition temperature of liquids, gels, and polymer melts.[101-106] More recently it has been employed in the areas of determine phonon band gap in phononic crystal as well.[54,96,107] Since measurements take place at some distance away from the instrument, the non-invasive nature BLS offers many advantages over the traditional invasive methods including tensile testing, differential scanning calorimetry, and rheology that are typically used to determine mechanical properties. Samples may be subject to greatly variable conditions; they may be exposed to conditions such as at extreme temperatures[108,109] or pressures,[108,110-112]. For thin polymeric films, samples may be on a substrate,[54,96,97,100,113,114] free standing,[115,116] or submerged in another medium.[113,117-119] Because specimen are probed using a laser,

sample size is constrained by the size of the focal spot of the beam; while an experimental setup using conventional optics allows one to measure sample with 0.5 μm thickness, measurements can be made on films as thin as 40 nm using more complex optical configurations or micro-Brillouin set up.[113,120,121]

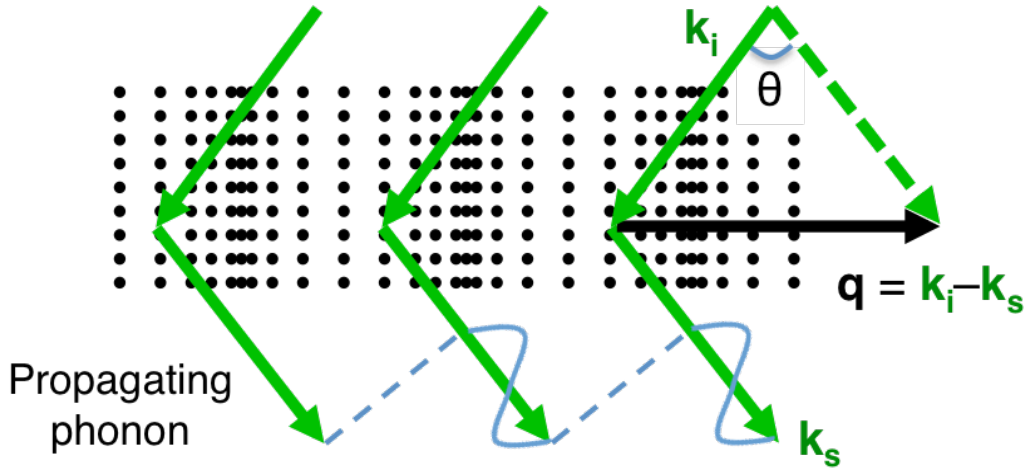

Figure 1.11: Light scattering mechanism for Brillouin light scattering; here k_i and k_s describe the scattering geometry off of propagating phonon (q) and θ indicates the angle between them.

As mentioned previously, acoustic phonons correspond to periodic atom vibrations that propagate through a medium. In the bulk, the two methods of propagation are longitudinal (LA) and transverse acoustic (TA) waves, where the phonons propagate parallel and perpendicular to the direction of motion, respectively. Depending on how light is polarized relative to direction of motion, one can discern between LA and TA modes. Figure 1.11 shows the general scattering mechanism for bulk acoustic phonons; when a beam of monochromatic light ($\mathbf{k_i}$) enters a medium, phonons will act as optical scattering centers. Brillouin suggested that when the incident light strikes a phonon propagating with wavevector **q**, the scattered light leaves the medium with a change in frequency ($\Delta\omega$) and wavevector of $\mathbf{k_s}$. Here the phonon wavevector **q** can be described

using Equation 1.1, where the wavelength corresponding to q is on the order of 200 nanometers and thus probing elastic properties at the molecular or nanometer scale. Since the energy exchange between light and matter is small, it can be assumed that $|\mathbf{k_i}| \cong |\mathbf{k_s}|$. Therefore, Equation 1.1 can be rewritten as Equation 1.2.

$$\mathbf{q} = \mathbf{k_i} - \mathbf{k_s}, \tag{1.1}$$

$$q = 2k_s \sin(\theta/2), \tag{1.2}$$

here, θ is the angle between the $\mathbf{k_i}$ and $\mathbf{k_s}$. For isotropic materials, the frequency shift of the scattered light can be related to the longitudinal sound velocity (υ_L) inside the medium using Equation 1.3, with a single refractive index n,

$$\upsilon_L = \frac{\lambda \cdot \Delta\omega}{2n \sin\frac{\theta}{2}}, \tag{1.3}$$

where λ is the wavelength of the incident beam. The longitudinal sound velocity can also be related to the Young's, bulk, and shear modulus (E, K, and G, respectively) using Equations 1.4 and 1.5,

$$\upsilon_L = \sqrt{\frac{K + \frac{4G}{3}}{\rho}}, \text{ and} \tag{1.4}$$

$$\upsilon_L = \sqrt{\frac{E}{\rho}\left(1 + \frac{2\nu^2}{1 - \nu - 2\nu^2}\right)}. \tag{1.5}$$

Here ρ and ν are the material density and Poisson's ratio, respectively. A schematic of a Brillouin spectrum can be seen in Figure 1.12.

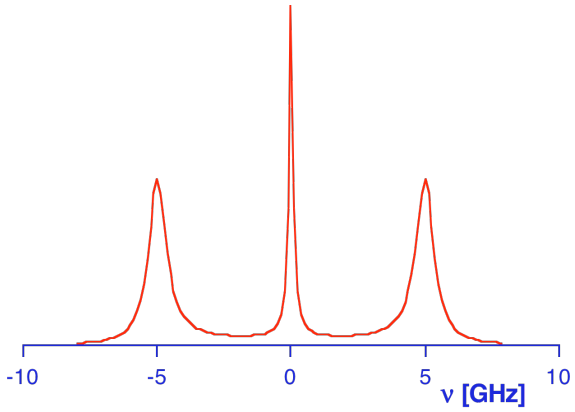

Figure 1.12: Schematic of a Brillouin spectrum. The central peak is the Rayleigh peak; the left and right peaks are the Stokes and anti-Stokes, respectively.

1.4.2 Raman Scattering

In Raman spectroscopy, electromagnetic waves interact with the local vibrations of molecules. Similar to BLS, an inelastic collision between photons and molecular vibration results in an energy change in the scattered light. In the case of Raman scattering, however, the absorption of a photon causes excitation of vibronic states of the bonding electrons, which are associated with the change in polarizabilities during molecular vibrations. Light is typically re-emitted within less than an oscillatory period of a molecule, and the frequency of the scattered light is reflective of the momentary difference in polarizability.

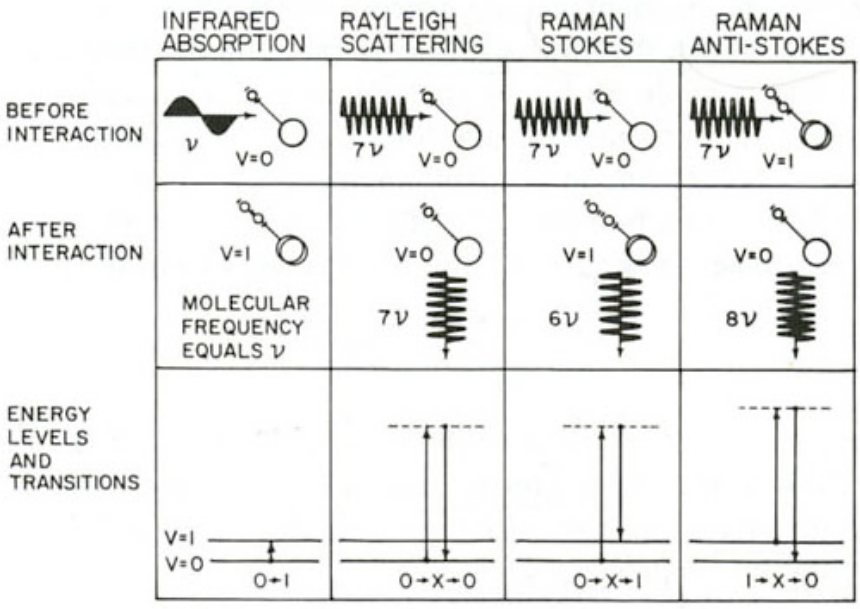

Figure 1.13: Energy transitions relative to different scattering phenomena[21]

When an incident beam of monochromatic light with energy of (hv_i) strikes a molecule in the ground state, the molecule will absorb the light causing the he energy of the molecule raise initially to an unstable higher energy state, here one of three events will happen.[122] In most situations, the molecule will return to the ground state; since the vibrational or rotational energy of the molecule remains unchanged. This collision is elastic; the scattered light will have the same energy and frequency as the incident light ($hv_s = hv_i$), this is known as Rayleigh scattering. However, another case may be the molecule falls to a different energy state; in this case, the energy of the molecule will be changed by ΔE_m as shown in Equation 6;[122] this is known as Raman scattering. A schematic of Raman and Rayleigh scattering can be seen in Figure 1.13.

$$\Delta E_m = hv_i - hv_s \tag{1.6}$$

If the molecule falls to a higher energy state ($v_i > v_s$), the ΔE_m will be positive; here the Raman spectrum will produce a Stokes line. If molecule falls to a lower energy state ($v_i < v_s$), the ΔE_m will be negative; the Raman spectrum will produce an anti-Stokes line. The latter case can only occur if the molecule was initially at a higher energy level. Since there are usually fewer molecules at a higher energy, the intensity of the anti-Stokes line is typically lower than that of Stokes line. Because changes in polarizability, and hence the excitation of vibronic states, are linked to specific vibrational modes, Raman scattering only occurs at the frequencies corresponding to these modes. Hence, the presence of certain structural units is identified based on the spectral features associated with the underlying molecular symmetries. Conversely, changes in the molecular structure yields shifts in the Raman peaks.

1.5 Thesis Outline

In our research, we explore the LBL deposition technique to fabricate thin polymer films and examined the outcomes using Brillouin light scattering. The objective was to understand how processing parameters affect the structural developments during film assembly and mechanical characteristics of the resulting films. In Chapter 2 we will describe, in detail, film deposition methods using *l*-LBL and *e*-LBL as well as the process for making mechanical measurements using BLS. Accordingly, we systematically varied the processing parameters; films were reinforced by nanoparticles with a variety of geometries including nano-scale fibrils, platelets, spheroids, and irregular shape. Furthermore, different polymers, solution concentration, filler volume fraction and size effect were explored as well. Chapters 3 – 6 will discuss the effect on mechanical

properties of LBL film as a result of changes in these elements, and Chapter 7 will compare the results of films made using the four particle geometries. Finally, there will be a brief conclusion in Chapter 8 as well as an outlook for future studies of the mechanical properties of LBL thin films using BLS. Hopefully, these new developments in BLS studies of LBL nanocomposites will provide a deeper understanding of the relationship between polymer – particle interaction in LBL films, this in turn will allow one to build stronger and more stable thin film nanocomposites.

References

[1] Bertrand, P.; Jonas, A.; Laschewsky, A.; Legras, R. "Ultrathin polymer coatings by complexation of polyelectrolytes at interfaces: suitable materials, structure and properties," *Macromol Rapid Comm* **2000**, *21*, 319-348.

[2] Hammond, P.T. "Form and function in multilayer assembly: New applications at the nanoscale," *Adv Mater* **2004**, *16*, 1271-1293.

[3] Matthews, F.L.; Rawlings, R. D. *Composite Materials: Engineering and Science*; Woodhead Publishing Limited: Abington Hall, 1999.

[4] Sperling, L.H. *Introduction to Physical Polymer Science*; John Wiley & Sons, Inc.: Hoboken, 2006.

[5] Reuss, A. "Account of the liquid limit of mixed crystals on the basis of the plasticity condition for single crystal," *Z Angew Math Mech* **1929**, *9*, 49-58.

[6] Voigt, W. "The relation between the two elastic moduli of isotropic materials," *Ann Phys* **1889**, *38*.

[7] Cox, H.L. "The Elasticity and Strength of Paper and Other Fibrous Materials," *Brit J Appl Phys* **1952**, *3*, 72-79.

[8] Krenchel. *Fibre Reinforcement*; Akademisk Forlag: Copenhagen, 1964.

[9] Jiang, Y.P.; Tohgo, K.; Yang, H. "Study of the Effect of Particle Size on the Effective Modulus of Polymeric Composites on the Basis of the Molecular Chain Network Microstructure," *Comp Mater Sci* **2010**.

[10] Vollenberg, P.H.T.; Dehaan, J.W.; Vandeven, L.J.M.; Heikens, D. "Particle-Size Dependence of The Young Modulus of Filled Polymers: 2. Annealing And Solid-State Nuclear Magnetic-Resonance Experiments," *Polymer* **1989**, *30*, 1663-1668.

[11] Ji, X.L.; Jing, J.K.; Jiang, W.; Jiang, B.Z. "Tensile modulus of polymer nanocomposites," *Polym Eng Sci* **2002**, *42*, 983-993.

[12] Schaefer, D.W.; Justice, R.S. "How nano are nanocomposites?," *Macromolecules* **2007**, *40*, 8501-8517.

[13] Sudduth, R.D. "Influence of nanoscale fibres and discs on intrinsic modulus and packing fraction of polymeric particulate composites and suspensions," *Mater Sci Tech-lond* **2003**, *19*, 1181-1190.

[14] Cho, J.; Sun, C.T. "A molecular dynamics simulation study of inclusion size effect on polymeric nanocomposites," *Comp Mater Sci* **2007**, *41*, 54-62.

[15] Hbaieb, K.; Wang, Q.X.; Chia, Y. H.J.; Cotterell, B. "Modelling stiffness of polymer/clay nanocomposites," *Polymer* **2007**, *48*, 901-909.

[16] Kaushik, A.K.; Podsiadlo, P.; Qin, M.; Shaw, C.M.; Waas, A.M.; Kotov, N.A.; Arruda, E.M. "The Role of Nanoparticle Layer Separation in the Finite Deformation Response of Layered Polyurethane-Clay Nanocomposites," *Macromolecules* **2009**, *42*, 6588-6595.

[17] Llorca, J.; Elices, M.; Termonia, Y. "Elastic properties of sphere-reinforced composites with a mesophase," *Acta Mater* **2000**, *48*, 4589-4597.

[18] McGee, S.; McCullough, R.L. "Prediction Of Elastic Properties of Particulate Filled Polymers and Foams," *Abstr Pap Am Chem S* **1981**, *182*, 177-POLY.

[19] Odegard, G.M.; Clancy, T.C.; Gates, T.S. "Modeling of the mechanical properties of nanoparticle/polymer composites," *Polymer* **2005**, *46*, 553-562.

[20] Picart, C.; Mutterer, J.; Richert, L.; Luo, Y.; Prestwich, G.D.; Schaaf, P.; Voegel, J. C.; Lavalle, P. "Molecular basis for the explanation of the exponential growth of polyelectrolyte multilayers," *P Natl Acad Sci Usa* **2002**, *99*, 12531-12535.

[21] Podsiadlo, P.; Choi, S.Y.; Shim, B.; Lee, J.; Cuddihy, M.; Kotov, N. . "Molecularly engineered nanocomposites: Layer-by-layer assembly of cellulose nanocrystals," *Biomacromolecules* **2005**, *6*, 2914-2918.

[22] Podsiadlo, P.; Kaushik, A.K.; Arruda, E.M.; Waas, A.M.; Shim, B.S.; Xu, J.D.; Nandivada, H.; Pumplin, B.G.; Lahann, J.; Ramamoorthy, A.; Kotov, N.A. "Ultrastrong and stiff layered polymer nanocomposites," *Science* **2007**, *318*, 80-83.

[23] Podsiadlo, P.; Michel, M.; Lee, J.; Verploegen, E.; Kam, N.W.S.; Ball, V.; Lee, J.; Qi, Y.; Hart, A.J.; Hammond, P.T.; Kotov, N.A. "Exponential growth of LBL films with incorporated inorganic sheets," *Nano Lett* **2008**, *8*, 1762-1770.

[24] Pozsgay, A.; Frater, T.; Szazdi, L.; Muller, P.; Sajo, I.; Pukanszky, B. "Gallery structure and exfoliation of organophilized montmorillonite: effect on composite properties," *Eur Polym J* **2004**, *40*, 27-36.

[25] Pukanszky, B.; Belina, K.; Rockenbauer, A.; Maurer, F.; et al."Effect of Nucleation, Filler Anisotropy and Orientation on the Properties of PP Composites," *Composites* **1994**, *25*, 205-214.

[26] Wu, C.L.; Zhang, M.Q.; Rong, M.Z.; Friedrich, K. "Silica nanoparticles filled polypropylene: effects of particle surface treatment, matrix ductility and particle species on mechanical performance of the composites," *Compos Sci Technol* **2005**, *65*, 635-645.

[27] Bledzki, A.K.; Faruk, O. "Wood fiber reinforced polypropylene composites: Compression and injection molding process," *Polym-plast Technol* **2004**, *43*, 871-888.

[28] Fu, S.Y.; Lauke, B. "Effects of fiber length and fiber orientation distributions on the tensile strength of short-fiber-reinforced polymers," *Compos Sci Technol* **1996**, *56*, 573-582.

[29] Karmaker, A.C.; Youngquist, J.A. "Injection molding of polypropylene reinforced with short jute fibers," *J Appl Polym Sci* **1996**, *62*, 1147-1151.

[30] Rizov, V.; Harmia, T.; Reinhardt, A.; Friedrich, K. "Fracture toughness of discontinuous long glass fiber reinforced polypropylene: An approach based on a numerical prediction of fiber orientation in injection molding," *Polym Polym Compos* **2005**, *13*, 121-130.

[31] Salvetat, J.P.; Briggs, G.A.D.; Bonard, J.M.; Bacsa, R.R.; Kulik, A.J.; Stockli, T.; Burnham, N.A.; Forro, L. "Elastic and shear moduli of single-walled carbon nanotube ropes," *Phys Rev Lett* **1999**, *82*, 944-947.

[32] Thostenson, E.T.; Chou, T.W. "On the elastic properties of carbon nanotube-based composites: modelling and characterization," *J Phys D Appl Phys* **2003**, *36*, 573-582.

[33] Fendler, J.H. "Self-assembled nanostructured materials," *Chem Mater* **1996**, *8*, 1616-1624.

[34] Luo, J.J.; Daniel, I.M. *Characterization and modeling of mechanical behavior of polymer/clay nanocomposites*; Northwestern Univ, Robert R McCormick Sch Engn & Appl Sci, Evanston, IL 60208 USA, 2003.

[35] Chen, C.G.; Justice, R.S.; Schaefer, D.W.; Baur, J.W. "Highly dispersed nanosilica-epoxy resins with enhanced mechanical properties," *Polymer* **2008**, *49*, 3805-3815.

[36] Love, J. C.; Estroff, L.A.; Kriebel, J.K.; Nuzzo, R.G.; Whitesides, G.M. "Self-assembled monolayers of thiolates on metals as a form of nanotechnology," *Chem Rev* **2005**, *105*, 1103-1169.

[37] Schwartz, D.K. "Mechanisms and kinetics of self-assembled monolayer formation," *Annu Rev Phys Chem* **2001**, *52*, 107-137.

[38] Ulman, A. "Formation and structure of self-assembled monolayers," *Chem Rev* **1996**, *96*, 1533-1554.

[39] Kim, F.; Kwan, S.; Akana, J.; Yang, P.D. "Langmuir-Blodgett nanorod assembly," *J Am Chem Soc* **2001**, *123*, 4360-4361.

[40] Maoz, R.; et al. "On the Formation and Structure of Self-Assembling Monolayers.1. A Comparative Atr-Wetability Study of Langmuir-Blodgett and Adsorbed Films on Flat Substrates and Glass Microbeads," *J Colloid Interf Sci* **1984**, *100*, 465-496.

[41] Petty, M.C. "Langmuir-Blodgett Films," *Endeavour* **1983**, *7*, 65-69.

[42] Decher, G. "Fuzzy nanoassemblies: Toward layered polymeric multicomposites," *Science* **1997**, *277*, 1232-1237.

[43] Elbakry, A.; Zaky, A.; Liebkl, R.; Rachel, R.; Goepferich, A.; Breunig, M. "Layer-by-Layer Assembled Gold Nanoparticles for siRNA Delivery," *Nano Lett* **2009**, *9*, 2059-2064.

[44] Mamedov, A.A.; Kotov, N.A. "Free-standing layer-by-layer assembled films of magnetite nanoparticles," *Langmuir* **2000**, *16*, 5530-5533.

[45] Mamedov, A.A.; Kotov, N.A.; Prato, M.; Guldi, D.M.; Wicksted, J.P.; Hirsch, A. "Molecular design of strong single-wall carbon nanotube/polyelectrolyte multilayer composites," *Nat Mater* **2002**, *1*, 190-194.

[46] Olek, M.; Ostrander, J.; Jurga, S.; Mohwald, H.; Kotov, N.; Kempa, K.; Giersig, M. "Layer-by-layer assembled composites from multiwall carbon nanotubes with different morphologies," *Nano Lett* **2004**, *4*, 1889-1895.

[47] Shang, L.B.; Liu, X.J.; Zhong, J.; Fan, C.H.; Suzuki, I.; Li, G.X. "Fabrication of ultrathin, protein-containing films by layer-by-layer assembly and electrochemical characterization of hemoglobin entrapped in the film," *Chem Lett* **2003**, *32*, 296-297.

[48] Shim, B. S.; Kotov, N.A. "Single-walled carbon nanotube combing during layer-by-layer assembly: From random adsorption to aligned composites," *Langmuir* **2005**, *21*, 9381-9385.

[49] Shim, B. S.; Podsiadlo, P.; Lilly, D.G.; Agarwal, A.; Leet, J.; Tang, Z.; Ho, S.; Ingle, P.; Paterson, D.; Lu, W.; Kotov, N.A. "Nanostructured thin films made by dewetting method of layer-by-layer assembly," *Nano Lett* **2007**, *7*, 3266-3273.

[50] Eckle, M.; Decher, G. "Tuning the performance of layer-by-layer assembled organic light emitting diodes by controlling the position of isolating clay barrier sheets," *Nano Lett* **2001**, *1*, 45-49.

[51] Li, Y.C.; Schulz, J.; Mannen, S.; Delhom, C.; Condon, B.; Chang, S.; Zammarano, M.; Grunlan, J.C. "Flame Retardant Behavior of Polyelectrolyte-Clay Thin Film Assemblies on Cotton Fabric," *Acs Nano* **2010**, *4*, 3325-3337.

[52] Guo, M.L.; Chen, J.H.; Li, J.; Nie, L.H.; Yao, S.Z. "Carbon nanotubes-based amperometric cholesterol biosensor fabricated through layer-by-layer technique," *Electroanal* **2004**, *16*, 1992-1998.

[53] Promnimit, S.; Dutta, J. "Synthesis and Electrical Characterization of Multilayer Thin Films Designed by Layer-by-Layer Self Assembly of Nanoparticles," *J Nano Res-sw* **2010**, *11*, 1-6.

[54] Gomopoulos, N.; Maschke, D.; Koh, C.Y.; Thomas, E.L.; Tremel, W.; Butt, H.J.; Fytas, G. "One-Dimensional Hypersonic Phononic Crystals," *Nano Lett* **2010**, *10*, 980-984.

[55] Lee, D.; Rubner, M.F.; Cohen, R.E. "All-nanoparticle thin-film coatings," *Nano Lett* **2006**, *6*, 2305-2312.

[56] Luther, J.M.; Law, M.; Beard, M.C.; Song, Q.; Reese, M.O.; Ellingson, R.J.; Nozik, A.J. "Schottky Solar Cells Based on Colloidal Nanocrystal Films," *Nano Lett* **2008**, *8*, 3488-3492.

[57] Liu, Y.J.; Wang, Y.X.; Claus, R.O. "Layer-by-layer ionic self-assembly of Au colloids into multilayer thin-films with bulk metal conductivity," *Chem Phys Lett* **1998**, *298*, 315-319.

[58] Yu, H.H.; Wu, H.B.; Li, X.F.; Zhu, Y.Z.; Jiang, D.S. "Self-assembly and optical properties of silica nanoparticulate thin films," *Acta Phys-chim Sin* **2001**, *17*, 1057-1061.

[59] Lvov, Y.; H, H.; Decher, G.; Mowald, H.; Mikhalilov, A.; Mtchedilishvily, B.; Morgunova, E.; Vainshtein, B. "Successive Deposition Of Alternate Layers Of Polyelectrolytes And A Charged Virus," *Langmuir* **1994**, *10*, 4232-4236.

[60] Nam, K. T.; Kim, D. W.; Yoo, P.J.; Chiang, C.Y.; Meethong, N.; Hammond, P. T.; Chiang, Y. M.; Belcher, A. M. "Virus-enabled synthesis and assembly of nanowires for lithium ion battery electrodes," *Science* **2006**, *312*, 885-888.

[61] Toellner, L.; Fischlechner, M.; Ferko, B.; Grabherr, R.M.; Donath, E. "Virus-coated layer-by-layer colloids as a multiplex suspension array for the detection and quantification of virus-specific antibodies," *Clin Chem* **2006**, *52*, 1575-1583.

[62] Caruso, F.; Schuler, C. "Enzyme multilayers on colloid particles: Assembly, stability, and enzymatic activity," *Langmuir* **2000**, *16*, 9595-9603.

[63] Zhao, J.Q.; Liu, B.H.; Zou, Y. L.; Xu, C.H.; Kong, J.L. "Photoelectric conversion of photosynthetic reaction center in multilayered films fabricated by layer-by-layer assembly," *Electrochim Acta* **2002**, *47*, 2013-2017.

[64] Richert, L.; Lavalle, P.; Payan, E.; Shu, X.Z.; Prestwich, G.D.; Stoltz, J.F.; Schaaf, P.; Voegel, J.C.; Picart, C. "Layer by layer buildup of polysaccharide films: Physical chemistry and cellular adhesion aspects," *Langmuir* **2004**, *20*, 448-458.

[65] DeLongchamp, D.M.; Hammond, P.T. "Highly ion conductive poly(ethylene oxide)-based solid polymer electrolytes from hydrogen bonding layer-by-layer assembly," *Langmuir* **2004**, *20*, 5403-5411.

[66] DeLongchamp, D.M.; Hammond, P.T. "Multiple-color electrochromism from layer-by-layer-assembled polyaniline/Prussian Blue nanocomposite thin films," *Chem Mater* **2004**, *16*, 4799-4805.

[67] Serizawa, T.; Hamada, K.; Kitayama, T.; Fujimoto, N.; Hatada, K.; Akashi, M. "Stepwise stereocomplex assembly of stereoregular poly(methyl methacrylate)s on a substrate," *J Am Chem Soc* **2000**, *122*, 1891-1899.

[68] Li, Q.; Quinn, J.F.; Wang, Y.; Caruso, F. "Preparation of Nanoporous Polyelectrolyte Multilayer Films via Nanoparticle Templating," *Chem. Mater* **2006**, *18*, 5480-5485.

[69] Onda, M.; Lvov, Y.; Ariga, K.; Kunitake, T. "Sequential reaction and product separation on molecular films of glucoamylase and glucose oxidase assembled on an ultrafilter," *J Ferment Bioeng* **1996**, *82*, 502-506.

[70] Hua, F.; Shi, J.; Lvov, Y.; Cui, T. "Patterning of layer-by-layer self-assembled multiple types of nanoparticle thin films by lithographic technique," *Nano Letters* **2002**, *2*, 1219-1222.

[71] Podsiadlo, P.; Sui, L.; Elkasabi, Y.; Burgardt, P.; Lee, J.; Miryala, A.; Kusumaatmaja, W.; Carman, M.R.; Shtein, M.; Kieffer, J.; Lahann, J.; Kotov,

N.A. "Layer-by-layer assembled films of cellulose nanowires with antireflective properties," *Langmuir* **2007**, *23*, 7901-7906.

[72] Cho, J.; Char, K. "Effect of layer integrity of spin self-assembled multilayer films on surface Wettability," *Langmuir* **2004**, *20*, 4011-4016.

[73] Lee, S.S.; Hong, J.D.; Kim, C. H.; Kim, K.; Koo, J.P.; Lee, K.B. "Layer-by-layer deposited multilayer assemblies of ionene-type polyelectrolytes based on the spin-coating method," *Macromolecules* **2001**, *34*, 5358-5360.

[74] Lee, S. S.; Lee, K. B.; Hong, J.D. "Evidence for spin coating electrostatic self-assembly of polyelectrolytes," *Langmuir* **2003**, *19*, 7592-7596.

[75] Bruening, M.; Dotzauer, D. "Just spray it," *Nat Mater* **2009**, *8*, 449-450.

[76] Izquierdo, A.; Ono, S.S.; Voegel, J.C.; Schaaf, P.; Decher, G. "Dipping versus spraying: Exploring the deposition conditions for speeding up layer-by-layer assembly," *Langmuir* **2005**, *21*, 7558-7567.

[77] Herrmann, A.S.; Nickel, J.; Riedel, U. "Construction materials based upon biologically renewable resources - from components to finished parts," *Polym Degrad Stabil* **1998**, *59*, 251-261.

[78] Walls, H.J.; Zhou, J.; Yerian, J.A.; Fedkiw, P.S.; Khan, S.A.; Stowe, M.K.; Baker, G.L. "Fumed silica-based composite polymer electrolytes: synthesis, rheology, and electrochemistry," *J Power Sources* **2000**, *89*, 156-162.

[79] Zadorecki, P.; Michell, A.J. "Future-prospects for wood cellulose as reinforcement in organic polymer composites," *Polym Composite* **1989**, *10*, 69-77.

[80] Pinnavaia, T. J.; Beall, G. W. *Polymer-clay nanocomposites*; Wiley: Hoboken, 2000.

[81] Glasser, W.G.; Taib, R.; Jain, R.K.; Kander, R. "Fiber-reinforced cellulosic thermoplastic composites," *J Appl Polym Sci* **1999**, *73*, 1329-1340.

[82] Bravo, J.; Zhai, L.; Wu, Z.; Cohen, R.E.; Rubner, M.F. "Transparent superhydrophobic films based on silica nanoparticles," *Langmuir* **2007**, *23*, 7293-7298.

[83] Luo, J.T.; Wen, H.C.; Chang, Y.M.; Wu, W.F.; Chou, C.P. "Mesoporous silica reinforced by silica nanoparticles to enhance mechanical performance," *J Colloid Interface Sci* **2007**, *305*, 275-279.

[84] Boldridge, D. "Morphological Characterization of Fumed Silica Aggregates," *Aerosol Sci Tech* **2010**, *44*, 182-186.

[85] Li, X.D.; Chang, W.C.; Chao, Y.J.; Wang, R.Z.; Chang, M. "Nanoscale structural and mechanical characterization of a natural nanocomposite material: The shell of red abalone," *Nano Lett* **2004**, *4*, 613-617.

[86] Ai, H.; Jones, S.A.; Lvov, Y.M. "Biomedical Applications of Electrostatic Layer-by-Layer Nano-Assembly of Polymers, Enzymes, and Nanoparticles," *Cell Biochemistry and Biophysics* **2003**, *23*, 23-43.

[87] Lvov, Y.; Munge, B.; Giraldo, O.; Ichinose, I.; Suib, S.L.; Rusling, J.F. "Films of Manganese Oxide Nanoparticles with Polycations or Myoglobin from Alternate-Layer Adsorption†," *Langmuir* **2000**, *16*, 8850-8857.

[88] Kurt, P.; Banerjee, D.; Cohen, R.E.; Rubner, M.F. "Structural color via layer-by-layer deposition: layered nanoparticle arrays with near-UV and visible reflectivity bands," *Journal of Materials Chemistry* **2009**, *19*, 8920-8927.

[89] Kim, S.H.; Cho, Y.S.; Jeon, S.J.; Eun, T.H.; Yi, G.R.; Yang, S.M. "Microspheres with tunable refractive index by controlled assembly of nanoparticles," *Advanced Materials* **2008**, *20*, 3268-3273.

[90] Krogman, K. C.; Druffel, T.; Sunkara, M. K. "Anti-reflective optical coatings incorporating nanoparticles," *Nanotechnology* **2005**, *16*, S338.

[91] Khan, S.A.; Baker, G.L.; Colson, S. "Composite polymer electrolytes using fumed silica fillers - rheology and ionic-conductivity," *Chem Mater* **1994**, *6*, 2359-2363.

[92] Raghavan, S.R.; Riley, M.W.; Fedkiw, P.S.; Khan, S.A. "Composite polymer electrolytes based on poly(ethylene glycol) and hydrophobic fumed silica: Dynamic rheology and microstructure," *Chem Mater* **1998**, *10*, 244-251.

[93] Zhou, S.X.; Wu, L.M.; Shen, W.D.; Gu, G.X. "Study on the morphology and tribological properties of acrylic based polyurethane/fumed silica composite coatings," *J Mater Sci* **2004**, *39*, 1593-1600.

[94] Brillouin, L. "Diffusion de la lumière et des rayons X par un corps transparent homogène, influence de l'agitation thermique," *Ann Phys* **1922**, *17*.

[95] Hillebrands, B.; Lee, S.; Stegeman, G.; Cheng, H.; Potts, J.E.; Nizzoli, F. "Evidence For The Existence of Guided Longitudinal Acoustic Phonons in ZnSe Films on GaAs," *Phys Rev Lett* **1988**, *60*, 832-835.

[96] Koblinger, O.; Mebert, J.; Dittrich, E.; Dottinger, S.; Eisenmenger, W.; Santos, P. V.; Ley, L. "Phonon stop bands in amorphous superlattices," *Phys Rev B* **1987**, *35*, 9372-9375.

[97] Nizzoli, F.; Hillebrands, B.; Lee, S.M.; Stegeman, G.I.; et al. "Determination of the Whole Set of Elastic Constants of a Polymeric Langmuir-Blodgett Film by Brillouin Spectroscopy," *Physical Review B* **1989**, *40*, 3323-3328.

[98] Rubio-Zuazo, J.; Jimenez-Rioboo, R.J.; Rodriguez-Canas, E.; Prieto, C.; Palacios, T.; Calle, F.; Monroy, E.; Sanchez-Garcia, M.A. "Brillouin characterization of the acousticwaves phase-velocity in $Al_xGa_{1-x}N$ epilayers," *Mat Sci Eng B-solid* **2002**, *93*, 168-171-PII S0921-5107(02)00020-X.

[99] Wittkowski, T.; Distler, G.; Jung, K.; Hillebrands, B.; Comins, J.D. "General methods for the determination of the stiffness tensor and mass density of thin films using Brillouin light scattering: Study of tungsten carbide films," *Phys Rev B* **2004**, *69*.

[100] Fioretto, D.; Carlotti, G.; Socino, G.; Palamieri, L.; et al. "Absorption and Velocity Dispersion of Acoustic Waves in Polybutylacrylate Films," *Ultrasonics Symposium* **1992**, 925-928.

[101] Asenbaum, A.; Aschauer, R.; Theisen, C.; Fritsch, T.; Wilhelm, E. "Brillouin scattering in liquid sulfur dioxide," *J Mol Liq* **2007**, *134*, 55-57.

[102] Kieffer, J. "Structural transistions in glasses and glassforming liquids," *Am Ceram Soc Bull* **2002**, *81*, 73-78.

[103] Ng, S.; Hosea, T. J.C.; Teh, H.C.; Gan, L.M. "Determination of the sol-gel transition-temperature and phase-diagram of a gelation system by brillouin spectroscopy," *J Phys E Sci Instrum* **1985**, *18*, 250-252.

[104] Pezeril, T.; Klieber, C.; Andrieu, S.; Nelson, K.A. "Optical Generation of Gigahertz-Frequency Shear Acoustic Waves in Liquid Glycerol," *Phys Rev Lett* **2009**, *102*.

[105] Tao, N.J.; LI, G.; Cummins, H.Z. "Brillouin-scattering study of the liquid-glass transition in supercooled aqueous lithium-chloride solutions - generalized hydrodynamics and mode-coupling analyses," *Phys Rev B* **1991**, *43*, 5815-5830.

[106] Xu, J. F.; Ren, X. B.; Gong, W. P.; Dai, R.; Liu, D. H. "Measurement of the bulk viscosity of liquid by Brillouin scattering," *Appl Optics* **2003**, *42*, 6704-6709.

[107] Still, T.; Cheng, W.; Retsch, M.; Jonas, U.; Fytas, G. "Colloidal systems: a promising material class for tailoring sound propagation at high frequencies," *J Phys-condens Mat* **2008**, *20*.

[108] Jiang, F.M.; Gwanmesia, G.D.; Dyuzheva, T.I.; Duffy, T.S. "Elasticity of stishovite and acoustic mode softening under high pressure by Brillouin scattering," *Phys Earth Planet In* **2009**, *172*, 235-240.

[109] Ko, J. H.; Kojima, S.; Koo, T.Y.; Jung, J.H.; Won, C.J.; Hur, N.J. "Elastic softening and central peaks in BaTiO3 single crystals above the cubic-tetragonal phase-transition temperature," *Appl Phys Lett* **2008**, *93*.

[110] Ahart, M.; Somayazulu, M.; Ye, Z.G.; Cohen, R.E.; Mao, H.K.; Hemley, R.J. "High-pressure Brillouin scattering of Pb(Mg1/3Nb2/3)O-3," *Phys Rev B* **2009**, *79*.

[111] Gorelli, F.A.; Santoro, M.; Scopigno, T.; Krisch, M.; Bryk, T.; Ruocco, G.; Ballerini, R. "Inelastic x-ray scattering from high pressure fluids in a diamond anvil cell," *Appl Phys Lett* **2009**, *94*.

[112] Stevens, L.L.; Orler, E.B.; Dattelbaum, D.M.; Ahart, M.; Hemley, R.J. "Brillouin-scattering determination of the acoustic properties and their pressure dependence for three polymeric elastomers," *J Chem Phys* **2007**, *127*.

[113] Forrest, J. A.; Dalnoki-Veress, K.; Stevens, J. R.; Dutcher, J. R. "Effect of Free Surfaces on the Glass Transition Temperature of Thin Polymer Films," *Physical Review Letters* **1996**, *77*, 2002-2005.

[114] Rioboo, R.J.J.; Souto, J.; de Saja, J.A.; Prieto, C. "Elastic Properties of Langmuir− Blodgett Films. A New Brillouin Spectroscopic Strategy," *Langmuir* **1998**, *14*, 6625-6627.

[115] de, G., PG. "Glass transitions in thin polymer films," *Eur Phys J E* **2000**, *2*, 201-203.

[116] Mattsson, J.; Forrest, J.A.; Borjesson, L. "Quantifying glass transition behavior in ultrathin free-standing polymer films," *Phys Rev E* **2000**, *62*, 5187-5200.

[117] Amer, M. S.; Bennett, M.; Maguire, J. F. "A Brillouin scattering study of C-60/toluene mixtures," *Chem Phys Lett* **2008**, *457*, 329-331.

[118] Galindez, C.; Madruga, F. J.; Lopez-Higuera, J. M. "Brillouin frequency shift of standard optical fibers set in water vapor medium," *Opt Lett* **2010**, *35*, 28-30.

[119] Lee, S. A.; Lindsay, S. M.; Powell, J. W.; Weidlich, T.; Tao, N. J.; Lewen, G. D.; Rupprecht, A. "A Brillouin-scattering study of the hydration of Li-DNA and Na-DNA films," *Biopolymers* **1987**, *26*, 1637-1665.

[120] Ike, Y.; Hashimoto, E.; Aoki, Y.; Kanazawa, H.; Kojima, S. "Micro-Brillouin scattering study of low temperature elastic properties of protein crystals," *J Mol Struct* **2009**, *924-26*, 157-160.

[121] Li, Y.; Lim, H. S.; Ng, S. C.; Wang, Z. K.; Kuok, M. H.; Vekris, E.; Kitaev, V.; Peiris, F. C.; Ozin, G. A. "Micro-Brillouin scattering from a single isolated nanosphere," *Appl Phys Lett* **2006**, *88*.

[122] Colthup N.B., Daly L.H., Wiberley S.E. *Introduction to Infrared and Raman Spectroscopy*; Academic Press, Inc: San Diego, 1990.

CHAPTER 2

Experimental

2.1 Materials Used and Preparation

2.1.1 Polyelectrolyte Solution Preparation

For these explorations, polyelectrolytes used included chitosan (chit), poly(styrene sulfonate) (PSS), poly(diallyldimethylammonium) (PDDA), polyurethane (PU), polyethylene oxide (PEO), and polyacrylic acid (PAA). Solutions of 1 wt% PDDA (M_w = 200,000 – 400,000, ρ = 1.04 g/cm^3), PSS (M_w = 200,000, ρ = 0.80 g/cm^3), PEO (M_w = 400,000, ρ = 1.13 g/cm^3) and PAA (M_w = 250,000, ρ = 1.14 g/cm^3) were made by diluting a concentrated stock of 20 wt% PDDA or 35 wt% PAA solutions or dissolving PSS or PEO powders using 18 MΩ deionized (DI) water, respectively; the solutions were stirred for 1 h or until incorporated. Solutions of 0.25 wt% chitosan (M_w = 6.3 million, ρ = 0.15 – 0.3 g/cm^3) were made from dissolving flakes of ≥75% deacetylated chitosan in a 3% acetic acid solution; the solutions were stirred vigorously until all the flakes dissolved and a clear, homogenous solution was obtained. Polyurethane (PU) with a molecular weight of 90,000 was diluted from a stock solution of 30 wt% PU by 2.5x, 3x, 5x, 17x, 43x, and 80x using DI water to create 11.7, 10.0, 6.0, 1.8, 0.7, 0.38 wt% solutions of PU, respectively. PDDA, PSS powder, chitosan flakes, and acids used were purchased from

Sigma-Aldrich, and PU was obtained from HEPCE CHEM Co. Ltd. (Kyungki-Do, Korea), all solutions made by dissolving as-received solutions.

2.1.2 Particle Solution Preparation

The rod-like, spherical and platelet filler particles are derived from cellulose nanocrystals (cellN), silica nanoparticles (SiO_2-NP, with diameters of 7, 12, and 22 nm) and Na^+-montmorillonite (MTM), respectively. Whatman's No.1 filter paper (98% cotton, ρ_{cellN} = 1.61 g/cm^3)[1] purchased from Fisher Scientific was used to make the cotton cellN solutions.[2] The filter paper was pulverized using a coffee grinder until a fluffy cotton-like texture is achieved. 99.9% sulfuric acid was poured into a beaker of 18 MΩ DI water to create a 100 mL solution of 64 w/v% sulfuric acid solution (*sulfuric acid is highly exothermic when mixing with water!*), this solution was allowed to stand until it is cooled to 45 ºC (45 – 60 min). 5 g of the blended filter paper is slowly placed into the 100 mL solution, and allowed to hydrolyze for 1 h at 45°C under vigorous stirring. The supernant was decanted from solution through centrifugation, followed by three subsequent washings and centrifugations, the supernant is finally diluted in 18 MΩ DI water to produce a solution of 5% w/v cellN; this solution is stored in a refrigerator at 4 ºC until needed. The solution was sonicated using a Ultrasonic Processor probe sonicator by Cole Parmer for 1 min on ice with 3 s sonications followed by 2 s rests at 30% amplitude prior to use.

Monodispersed Ludox® silica nanoparticles (SiO_2-NP) from Sigma-Aldrich with diameters of 7, 12 and 22 nm were diluted from original stock of 30 – 40 wt% to 5% w/v using 18 MΩ DI water and stirred until incorporated. Na^+-Montmorillonite (MTM) clay

with diameters of 100 – 1000 nm and a density of 2.86 g/cm^3 was purchased from Southern Clay Products. 5 g of MTM clay was dissolved into 1 L of 10 MΩ, the clay particles were allowed to exfoliate into silicate layers by vigorous stirring for one week. 0.5 g of Cab-O-Sil M5 fumed silica from Cabot GmbH (Hanau, Germany) was dispersed in 100 mL DI water by sonication at high frequency using a probe sonicator; the solution was sonicated for 30 minutes with 3 s sonications followed by 2 s rests at 30% amplitude.

2.1.3 Florescence Tagging of PEO and PAA

For exponentially grown LBL films, one set of PEO/PAA films was made using PEO and PAA tagged with florescent dyes. PEO were functionalized with fluorescein isothiocyanate (FITC) that fluoresces green light with excitation and emission wavelengths of 492 and 519 nm, respectively. To tag the ends of PEO chains, 1 mg FITC was dissolved first in a 1 mL solution of 99.9% dimethyl sulfoxide (DMSO) and then combined with 100 mL of 1 wt % PEO solution; this solution was then stirred for 24 hrs in the dark to allow for functionalization of –OH groups. PAA were functionalized with rhodamin B (Rh B), this dye fluoresces red light with excitation and emission wavelengths of 540 and 625 nm, respectively. To tag the PAA, 0.1 g Rh B was dissolved in 2 mL solutions of DMSO and then combined with 100 mL solution of 1 wt % PAA solution; similarly this solution was stirred for 24 hrs in the dark, every other –OH groups along the backbone of PAA was tagged. Following functionalization, both solutions underwent dialysis for one week in order to remove the excess unfunctionalized dye. PEO and PAA solutions were poured into cellulose membrane tubing where the ends were clip shut, the bags were then submerged in large baths of 18 MΩ DI water under slow stirring; the water bath was refreshed every 4 – 5 hours to avoid saturation of

dialysis water and for speedier dialysis. Following dialysis, the solutions were removed from dialysis bags and used as is for LBL deposition. FITC, Rh B dyes, and DMSO were purchased from Sigma-Aldrich, and cellulose membrane tubing was purchased from Fisher Scientific.

2.2 Film Synthesis

2.2.1 Linear Growth Layer-by-Layer Assembly

Table 2.1:Deposition parameters for LBL films created

Films	Electrolyte Solution (charge)	Dep. Time (min)	Rinse Time (sec)	Dry Time (min)	Method of Fabrication
Polymer/cellN	PDDA (+) Chitosan (+) PSS (–) CellN (–)	1 1 1 1	30 30 30 30	1 1 1 1	Hand made or Nanostrata
PU/MTM	PU (+) MTM (–)	5 5	120 120	1 1	Nanostrata or stainer
PU/SiO_2-NP	PU SiO_2-NP (–)	5 5	30 30	1 1	Hand made
PEO/PAA/SiO_2-*f*	PEO (N/A) PAA (weak –) SiO_2-*f* (–)	10 10 10	2 2 2	– – –	Stainer

[Polymer/particle] LBL films were fabricated by hand-dipping substrates into electrolyte solutions or machine dipped using a StratoSequence IV from Nanostrata Inc. (Tallahassee, FA). Films were deposited either on Si wafers (University Wafers), glass slides (Fisher Scientific), or Teflon tape (Ted Pella); prior to use, substrates were cleaned using a 3:1 H_2SO_4:H_2O_2 (piranha, *highly exothermic reaction*) solution for 1 h and rinse with DI water before use. LBL composites were made through a series of deposition and cleaning steps: the substrate is (1) submerged into the cationic solution with a deposition

time of typically between 1 – 5 min, (2) rinsed with DI water for 1 min, and (3) dried using compressed air; this is followed by dipping the same substrate into a (4) anionic solution followed by (5) rinsing and (6) drying using the same allotted time as cationic deposition. Steps 1 – 6 were repeated until a desired thickness of between 0.5 – 3 µm is achieved. Table 2.1 lists the deposition time for all combinations of films and schematics of cross sectional views of these films can be seen in Figure 2.1. For cellN films, one set of samples was broken in half, and one of the halves was heat-treated at 120°C for 24 hours. For comparison, pure polymeric films were cast in to a Petri dish and dried over night at 80°C in a convection oven.

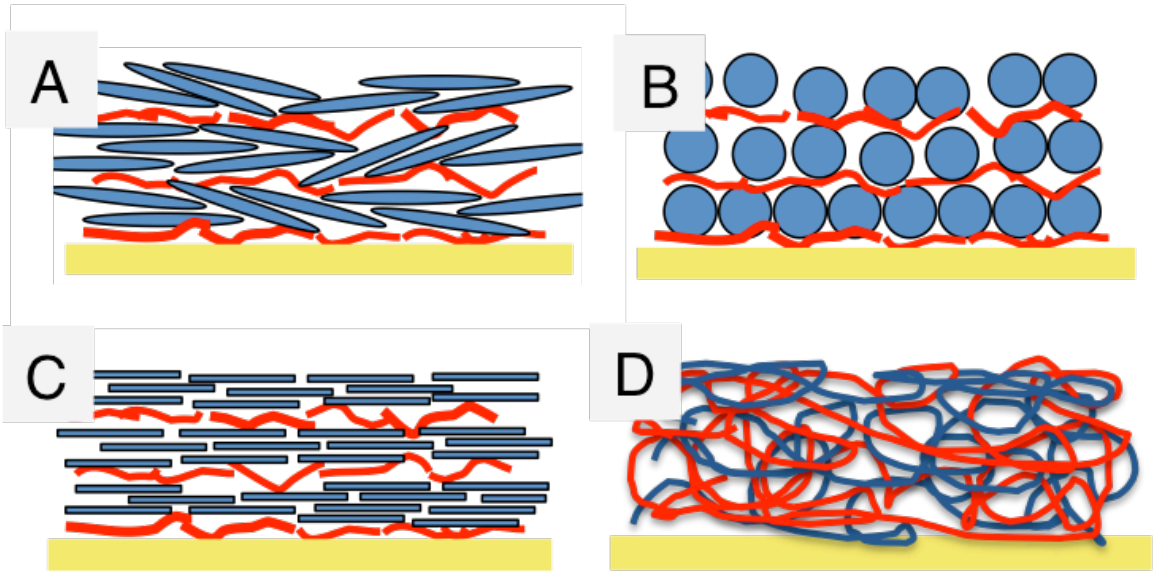

Figure 2.1: Schematic of cross-sectional view of LBL assembled films. A - C) linearly grown LBL films using cellN, SiO_2-NP and MTM clay, respectively; D) exponentially grown PEO/PAA film.

Films nomenclature typically follows the form of $[polymer/particle]_{x,}$ where polymer/particle refers to the repeating structure and "x" indicates the number of layers. For example, $[PDDA/cellN]_{30}$ indicates 30 repeating layers of PDDA and cellN where one bilayer is one PDDA/cellN repeating layer. For more complicated films,

nomenclature may include solution concentration, particle size, and stacking of different combinations of polyelectrolytes. For example, $[PU\text{-}80x/MTM]_{30}$, and PU/SiO_2-12, the 80x refers to the dilution of PU, SiO_2-12 refers to the 12 nm diameter of the SiO_2 particles, whereas the nomenclature $[(PDDA/cellN)_1/(PDDA/PSS)_9]_{100}$, indicates PDDA/PSS is repeated 9 times following one bilayer of PDDA/cellN, this structure is then repeated 100 times.

The volume fractions of particles were varied by changing the thickness of the polymer layers. For cellN films, PSS was substituted for cellN to a variable degree. The resulting film structures are described by $[(polymer/cellN)_x/(polymer/PSS)_y]_z$, where the polymer is either chitosan or PDDA. For example, in [chit/cellN/chit/PSS] every other layer of cellN is replaced by a layer of PSS. Five film structures were made: [polymer/PSS], $[(polymer/cellN)_1/(polymer/PSS)_9]$, [polymer/cellN/polymer/PSS], $[(polymer/cellN)_4/(polymer/PSS)_1]$, and [polymer/cellN]. For PU/MTM clay and PU/SiO_2-NP films, different concentration of PU solutions (as mentioned previously) were used where more concentrated PU solutions produced thicker films and vice versa. For $[PU/MTM]_{300}$ made on glass slides, the films were detached by scoring the sides of the films using a razor and placed in solutions of 1% hydrofluoric (HF) acid (*extremely corrosive!*). The detached film was treated using isopropanol overnight and dried in a convection oven at 60 ºC.

2.2.2 Exponential Growth Layer-by-Layer Assembly

For *e*-LBL assembly, Teflon substrates were dipped into the PEO solution for 10 min followed by rinsing using DI water for 2 min then dipped into the PAA solution for 10

min followed by rinsing with DI water for 2 min. For PEO/PAA/SiO_2-*f* films, the substrate was dipped into SiO_2-*f* solutions for 10 min then rinsed for 2 min between PAA and PEO depositions. Following film fabrication, the samples were dried in a convection oven for 1 hr at 80 ºC. Since samples were made on Teflon, no chemical detachment is necessary; samples were detached after drying by scoring the sides of the films using a razor and peeled off using a pair of tweezers. Six sets of *e*-LBL films were created using a Midas II automatic slide stainer where each set was grown to have a total of 30 PEO/PAA bilayers: $[PEO/PAA]_{30}$, $[PEO/PAA/SiO_2\text{-}f]_{30}$, $[(PEO/PAA)_2/SiO_2\text{-}f]_{15}$, $[(PEO/PAA)_3/SiO_2\text{-}f]_{10}$, $[(PEO/PAA)_5/SiO_2\text{-}f]_6$, and $[(PEO/PAA)_{10}/SiO_2\text{-}f]_3$; this way the volume fraction of SiO_2-*f* was varied.

2.3 Film Characterization

2.3.1 Film Growth

The growths of these films were monitored using ellipsometry, UV-vis and quartz crystal microbalance (QCM). Film thickness was measured using J.A. Woollam BASE-160 Spectroscopic Ellipsometer following deposition of each layer or bilayer of the film on silicon wafer. The equipment was calibrated each time using a clean silicon wafer, and the calculations were fitted using a Cauchy model. The refractive indices of the films were determined using a Nanofilm Technologie GmBH Ellipsometer with a laser wavelength of 532 nm for films deposited on Si wafer; measurements were taken at ~100 nm. A four-zone analysis between angles of 55 – 76º was done and the results were fitted using a Cauchy model. Film adsorption was also monitored using an 8453 UV-vis Chem Station Spectrophotometer from Agilent Technologies. For UV-vis absorption,

measurements were taken after the deposition of each bilayer of PDDA/SiO_2-NP on a clean glass slide. Mass adsorption of LBL films were measured using a QCM200 Quartz Crystal Microbalance (QCM) by Stanford Research Systems. Polymer or cellN were allowed to deposit onto a 5 MHz AT-cut quartz crystal, the frequency of the crystal was recorded after rinsing and drying step of each layer deposition. The crystal was cleaned using a 5% sodium chloride solution after each use.

2.3.2 Thermogravimetric Analysis

The weight fractions of PU/MTM clay and PEO/PAA/SiO_2-*f* were analyzed using a thermo-gravimetric analyzer (TGA) Pyris 1 from Perkin Elmer (Waltham, MA). Detached PU/MTM clay and PEO/PAA/SiO_2-*f* films were cut into small pieces weighing between 0.5 – 2 mg as the load cell for TGA is very sensitive to excessive mass. The samples were then heated under air flow with a rate of 10 mL/min using the following cycle: (1) hold at 20 ºC for 10 min; (2) heat to 110 ºC at a rate of 10 ºC/min; (3) hold at 110 ºC for 10 min; (4) heat to 1000 ºC at a rate of 10 ºC/min. Following the heating cycle, the remainder weight reflects the amount of the MTM clay or the SiO_2-*f* incorporated into the LBL films.

2.3.3 Film Imaging

One bilayer of PDDA/cellN, PDDA/SiO_2-22nm and PU/clay was deposited on Si wafer for imaging using a NanoScope IIIa atomic force microscopy (AFM) in tapping mode from Veeco Instruments (Santa Barbara, CA). PDDA/SiO_2-NP was also imaged using JEOL 3011 HREM transmission electron microscopy (TEM). One bilayer of PDDA/SiO_2-NP with 7, 12, 22 nm diameters was deposited onto a copper grid then

imaged using JEOL 3011 HREM TEM. PEO/PAA films were imaged using an XL30 Philips Scanning Electron Microscope (SEM); because of non-conductive nature of LBL films, the samples were sputtered with a few nanometer thick layer of gold prior to imaging. The cross-sectional view of dye-tagged $[PEO/PAA]_{30}$ film was imaged using a Leica SP2 confocal laser scanning microscope (CLSM).

2.3.4 Density and Volume Fraction Determinations

The densities of the cellN and SiO_2-NP LBL films are calculated using the Sauerbrey equation,[3]

$$\frac{\Delta m}{A} = \frac{-\Delta f \sqrt{\rho_q \mu_q}}{2 f_0^2}, \tag{2.1}$$

which allows us to calculate the change in mass (Δm) per unit area (A) from the measured change in frequency (Δf) with knowledge of the resonant frequency (f_0), density (ρ_q = 2.648 g/cm^3) and shear modulus (μ_q = 2.947×10^{11} gcm^{-1}s^{-2}) of the quartz crystal. The density of the film can then be calculated using the thickness, t, determined from ellipsometry according to

$$\rho_s = \frac{\Delta m}{A}\frac{1}{t}. \tag{2.2}$$

Figure 2.2 illustrates in the information that can be derived from ellipsometry and QCM data for density and volume fraction calculations.

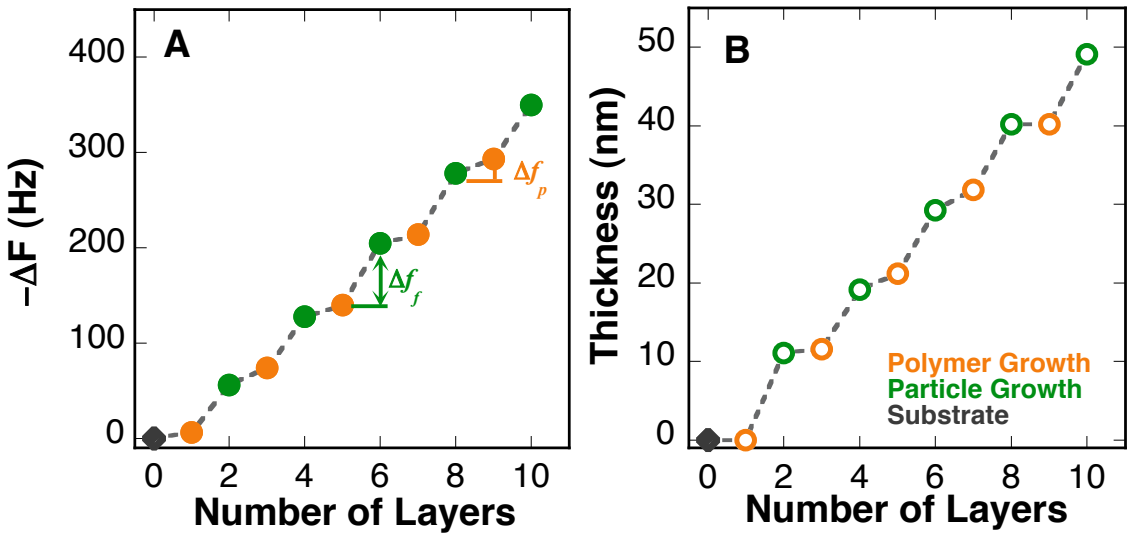

Figure 2.2: A) QCM and B) ellipsometry data of PU/SiO_2-NP growth

The volume fraction of polymer or fiber ($\phi_{p,f}$) can be defined as the ratio of volume occupied by polymer or fiber ($V_{p,f}$) and the entire sample volume (V_T),

$$\phi_{p,f} = \frac{V_{p,f}}{V_T}. \tag{2.3}$$

Using the densities of the raw polymer or fiber, i.e. 1.02 and 2.2 g/cm^3 for PU and SiO_2, the volume of the polymer or fiber can be derived using the mass required for that particular density:

$$V_{p,f} = \frac{m_{p,f}}{\rho_{p,f}}, \tag{2.4}$$

here $m_{p,f}$ and $\rho_{p,f}$ represent the mass and densities of polymer or fiber. Equation 2.3 then can be rewritten as

$$\phi_{p,f} = \frac{m_{p,f}}{\rho_{p,f}}\frac{1}{V_T} \text{ or } \frac{m_{p,f}}{\rho_{p,f}}\frac{1}{At}. \tag{2.5}$$

Note that Equation 2.5 is very similar to that of Equation 2.2 with the exception that instead using the total change in mass, mass change for individual constituent is used. This can be calculated using the summation of change in frequencies after the deposition of polymer or fiber ($\Delta f_{p,f}$). Therefore by combining Equations 2.1 – 2.5 the volume fraction of polymer or fiber is

$$\phi_{p,f} = \frac{1}{\rho_{p,f}} \frac{\sum \Delta f_{p,f} \sqrt{\rho_q \mu_q}}{2 f_0^2 t}. \tag{2.6}$$

Finally, the porosity (ϕ_{pore}) is simply,

$$\phi_{pore} = 1 - \left(\phi_p + \phi_f \right). \tag{2.7}$$

The volume fractions of MTM and SiO_2-*f* in PU/MTM or PEO/PAA/SiO_2-*f* films were calculated using the measured weight fraction w_f of the filler material determined from TGA and Equation 2.8,[4]

$$\phi_f = \frac{w_f \rho_p}{\rho_f \left(1 - w_f\right) + w_f \rho_p}, \tag{2.8}$$

where, ρ_f and ρ_p are the densities of the MTM clay and polymer, respectively.

2.4 Brillouin Light Scattering

A Coherent Verdi solid-state laser with a wavelength of 532 nm was used to illuminate the samples at incident powers of less than 10 mW. For dry measurements, the laser light was focused onto the film deposited on the polished side of the Si wafer. The scattered light was collected over a period of 20 – 60 min, and analyzed using a Sandercock tandem 6-pass Fabry-Perot interferometer. For dehumidifying experiments,

a dry sample is used to focus the beam and replaced with a fully humidified sample during measurements. Measurements were taken at ~1 min increments for 20 mins and 5 min increment after that; these samples were monitored for a total of 35 – 45 mins.

A schematic of this scattering setup can be seen in Figure 2.3. The scattering intensity from the polymer film is significantly stronger than that from silicon. In fact, for the chosen incident powers and collection times, scattering from the silicon substrate is negligible in comparison to that from the polymer film. Consequently, the collected spectra remain devoid of any signal from silicon and all peaks can be attributed to the polymer film. Note that during measurement, the energy imparted by the probing laser is negligibly small. Scattering is the result of thermal phonons that exist in any material at finite temperature. The measurement is therefore non-invasive and the specimen remains in thermodynamic equilibrium at all times. The scattered light is typically sampled from a small volume (i.e., a spot ~50 μm in diameter and ~1 μm thick), as defined by the collection optics, providing remarkable spatial resolution. By moving the focal point, the elastic modulus of any given specimen was measured multiple times for each sample, ensuring accuracy and repeatability.

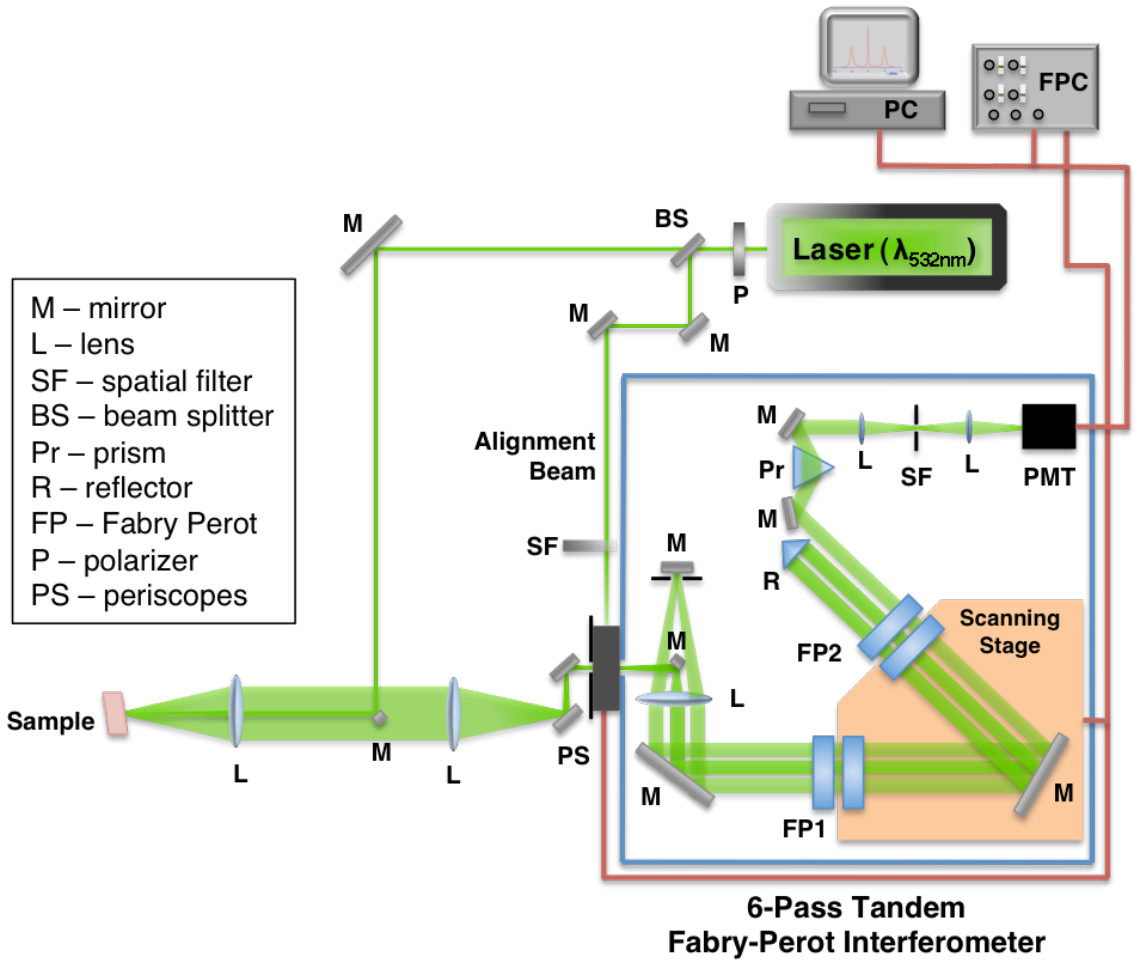

Figure 2.3: Optical table set up for back scattering geometry, the green lines indicate incident laser or scattered light paths and red lines indicate wires leading up to control units; PMT – photomultiplier tub, PC – personal computer, FPC – Fabry-Perot Controller.

Brillouin spectra were collected with external optics configured in 180° backscattering geometry, with an incident direction slightly inclined by an angle α with respect to the surface normal to avoid flooding the detector with excess reflected light. A close up of the scattering geometries is shown in Figure 2.4. This method provides some unique advantages that are particularly useful for probing the adhesion between individual layers of LBL assembled films; one is able to measure both the elastic constants within the plane of the film and perpendicular to it, i.e., in growth direction (or

out of plane).[5-7] The propagation direction of the phonons probed in this measurement can be derived from the momentum balance construct shown in Figure 2.4. Prior to reaching the sample surface the incident light follows the direction $\mathbf{k}_{i,e}$, which upon entering the polymer film reorients to $\mathbf{k}_i$ due to refraction Light that scatters from phonons propagating in the $\pm\mathbf{q}^{180}$ direction, which is either parallel or anti-parallel to $\mathbf{k}_i$, exits along the exact same path as the incident light and constitutes the backscattered radiation. For transparent materials some incident light reflects off the back surface of the film and continues along the direction $\mathbf{k}'_i$. For as long as the specimen is thin, additional scattering points (marked by the small circles) will lie within the focal volume of the collection optics. Hence, scattered light exiting the specimen along the $\mathbf{k}_{s,e}^{2\alpha}$ direction is collected at the same time as the backscattered light ($\mathbf{k}_{s,e}^{180}$). Accordingly, two peaks are observed in the Brillouin spectrum, the 180° peak and a so-called 2α peak.[7,8]

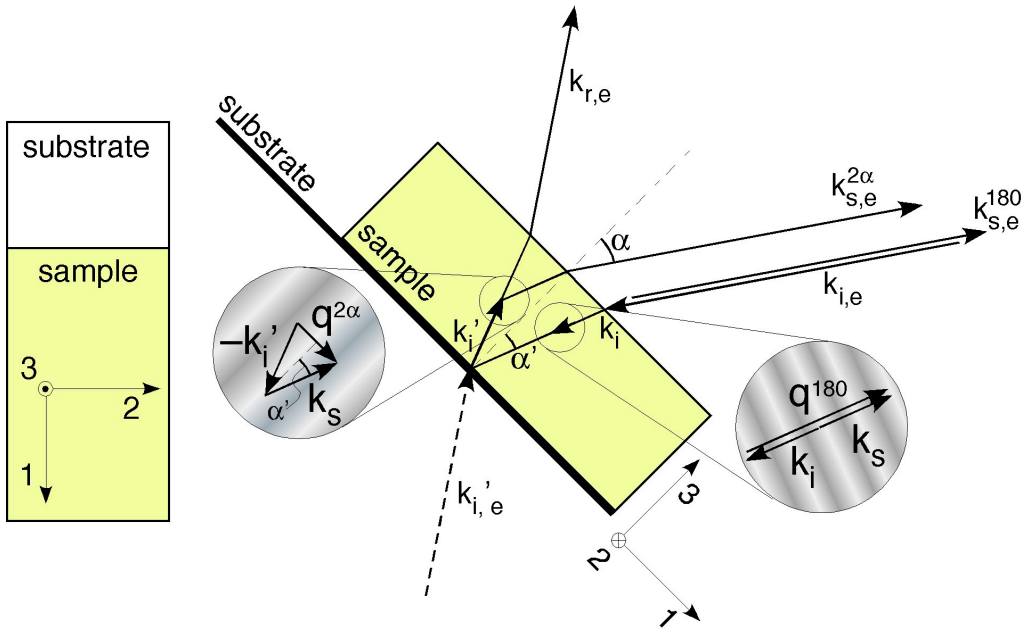

Figure 2.4: Brillouin light scattering in backscattering geometry. Here k_i, k_s, and k_r are the incident, scattered, and reflected beams; 1 and 2 directions are in the growth plane of the sample, and direction 3 is normal to the growth plane; α is the angle k_i makes with the 3 direction; q is the phonon propagation direction.

As can be seen from the wavevector diagram in Figure 2.4, the 2α peak results from light scattering from phonons propagating within the growth plane, i.e., along $\mathbf{q}^{2\alpha}$. Note that the light path giving rise to the 2α scattering is equivalent to the platelet geometry,[8] which would be achieved by replacing the reflected beam $\mathbf{k}'_i$ by one that entered the film on the substrate side following the direction indicated by $\mathbf{k}'_{i,e}$. In platelet geometry the surfaces through which the light enters and exits the sample are parallel, and the directions of the incident and scattered light form the same angle with respect to the surface normal. The sample surface, and any plane parallel to it, bisect the angle formed by $\mathbf{k}'_{i,e}$ and $\mathbf{k}_{s,e}^{2\alpha}$. Once we have identified the wavevectors of the phonons probed, we can determine their propagation velocities, according to $v = \Delta\omega/q$, where $\Delta\omega$ is the frequency shift in the Brillouin spectrum between incident and scattered light for the corresponding scattering mode. Hence, for the phonons contained within the growth plane of the sample this relationship is

$$v_{2\alpha} = \frac{\lambda \cdot \Delta\omega_{2\alpha}}{2\sin\alpha}, \tag{2.9}$$

and for the backscattering mode it is

$$v_{180} = \frac{\lambda \cdot \Delta\omega_{180}}{2n}. \tag{2.10}$$

In these relationships, λ is the wavelength of the incident beam and n is the refractive index of the sample. In case of the 2α mode, the refractive index of the scattering medium is eliminated using Snell's law, $n \cdot \sin\alpha' = \sin\alpha$. The precise location of the peaks is obtained by fitting Lorentzian functions to the measured spectra, from which we evaluate the peak center and its full-width half maximum. From the sound velocities and

the sample density, ρ_s, and the elastic constants, c_{xx}, of the thin films can be calculated according to

$$c_{xx} = \rho_s \upsilon_x^2. \tag{2.8}$$

By combining Equations 2.1 – 2.2 and 2.6 – 2.8, the longitudinal elastic constants in the growth plane (c_{11}) and in the growth direction (c_{33}) can be determined.

Hence, using a single light scattering measurement we can determine the elastic modulus in two different directions, in plane and nearly perpendicular to it. The elastic modulus in growth direction is of particular interest, as it is difficult to determine by other means, and therefore provides new insights into the influence of interfaces between deposited layers on the overall mechanical properties of these films. This method may be applicable to a variety of thin transparent films. The 2α peak can be observed in both supported and free standing films; in the case of supported films, the substrate acts as a reflective surface, whereas for free standing films, the change in refractive indices between the sample and air causes total internal reflection beyond a specific angle α.

2.5 Raman Scattering

Raman spectra were collected using a TriVista TR777 triple monochromator. Each stage has a focal length of 750 mm. The three monochromators were configured in subtractive mode for laser line suppression. The backscattering scattering geometry was used for Raman spectroscopy as well, the setup is similar to that of BLS except a mirror is placed between the focusing lens and collimator to guide the scattered light towards the Raman spectrometer. Each spectrum was collected over 1-5 minutes and analyzed using FITYK.

References

[1] Sperling, L. H. *Introduction to Physical Polymer Science*; John Wiley & Sons, Inc.: Hoboken, 2006.

[2] Fengel, D. "Degradation Structures in Partially Hydrolyzed Cellulose," *Holz Roh Werkst* **1984**, *42*, 276-276.

[3] Sauerbrey, G. "Verwendung Von Schwingquarzen Zur Wagung Dunner Schichten Und Zur Mikrowagung," *Z Phys* **1959**, *155*, 206-222.

[4] Kaushik, A. K.; Podsiadlo, P.; Qin, M.; Shaw, C. M.; Waas, A. M.; Kotov, N. A.; Arruda, E. M. "The Role of Nanoparticle Layer Separation in the Finite Deformation Response of Layered Polyurethane-Clay Nanocomposites," *Macromolecules* **2009**, *42*, 6588-6595.

[5] Carlotti, G.; Fioretto, D.; Socino, G.; Verona, E. "Brillouin-Scattering Determination of the Whole Set of Elastic-Constants of a Single Transparent Film of Hexagonal Symmetry," *J Phys-condens Mat* **1995**, *7*, 9147-9153.

[6] Gomopoulos, N.; Saini, G.; Efremov, M.; Nealey, P. F.; Nelson, K.; Fytas, G. "Nondestructive Probing of Mechanical Anisotropy in Polyimide Films on Nanoscale," *Macromolecules* **2010**, *43*, 1551-1555.

[7] Hillebrands, B.; Lee, S.; Stegeman, G.; Cheng, H.; Potts, J. E.; Nizzoli, F. "Evidence For The Existence of Guided Longitudinal Acoustic Phonons in ZnSe Films on GaAs," *Phys Rev Lett* **1988**, *60*, 832-835.

[8] Rioboo, R. J. J.; Souto, J.; de Saja, J. A.; Prieto, C. "Elastic Properties of Langmuir− Blodgett Films. A New Brillouin Spectroscopic Strategy," *Langmuir* **1998**, *14*, 6625-6627.

[9] Cheng, W.; Sainidou, R.; Burgardt, P.; Stefanou, N.; Kiyanova, A.; Efremov, M.; Fytas, G.; Nealey, P. F. "Elastic properties and glass transition of supported polymer thin films," *Macromolecules* **2007**, *40*, 7283-7290.

[10] Gomopoulos, N.; Cheng, W.; Efremov, M.; Nealey, P. F.; Fytas, G. "Out-of-Plane Longitudinal Elastic Modulus of Supported Polymer Thin Films," *Macromolecules* **2009**, *42*, 7164-7167.

CHAPTER 3

Elastic Modulus of Rod-like Particles in LBL Films

Engineering materials derived from renewable, natural resources are becoming more important with the increase in environmental awareness; one such biomaterial is cellulose. Natural cellulose is derived predominately from plant cell walls. In its nanocyrstalline form, cellulose nanocrystals are rod-like with dimensions of 5 nm in diameter and 200 – 400 nm in length, here they will be abbreviated as cellN.[1] CellN also have a very high stiffness; a single cellN has a reported axial Young's modulus of 100 – 160 GPa, depending on its degree of crystallinity,[2,3] and a transverse Young's modulus of ~30 GPa.[3] As one of the most abundant natural fibers, cellulose is also cheap, light-weight, biodegradable, and a renewable resource,[1,4] thus making it a desirable candidate for composite filler.

Podsiadlo et al. demonstrated a way to incorporate cellN into thin films using hydrolyzed cotton cellulose in combination with the layer-by-layer (LBL) fabrication method.[5] In this chapter, we report the mechanical properties of LBL polymer/cellN composite films measured using Brillouin light scattering. This allows for the measurement of elastic moduli at a microscopic level and in specific directions, therefore yielding information about the orientation of the nanocrystals within the layered structure of these materials.

3.1 Film Growth and Characterization

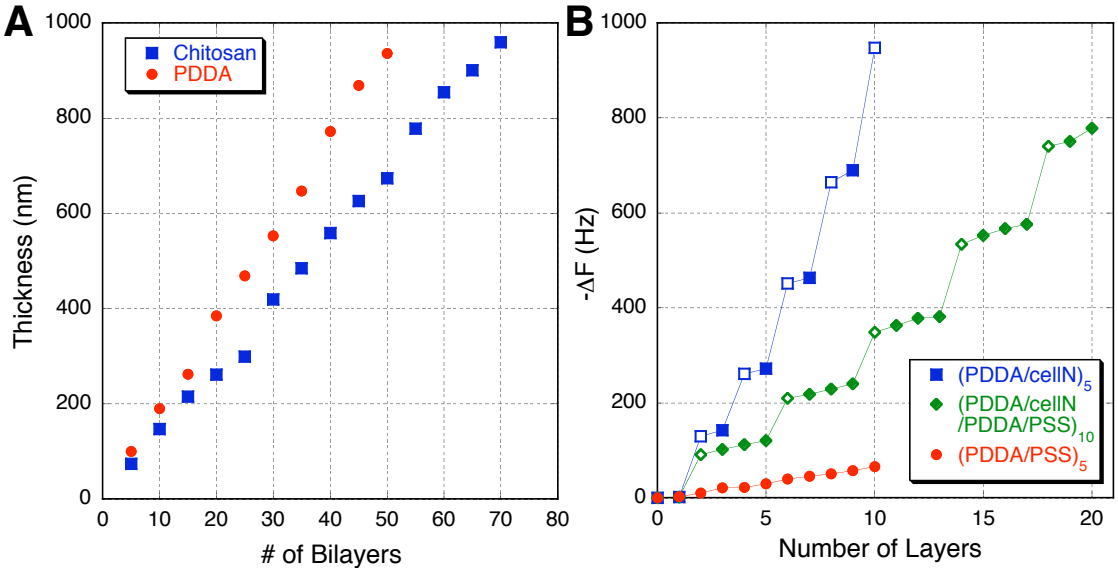

Figure 3.1: A) Film thickness as a function of the number of bilayers for chitosan/cellN and PDDA/cellN layer-by-layer films; B) change in frequency as a function of number of layers for select PDDA/cellN films, the solid points indicate polymer growth and open points indicate cellN growth.

PDDA and chitosan polyanions were selected because prior work[5,6] showed fast film growth and high particle loading capacity. To monitor the growth of the films and to determine the elastic moduli of the LBL films as a function of thickness, the film thickness was measured every five bilayers (BL), up to 1 μm as shown in Figure 3.1A. Linear trends are observed for both chit/cellN and PDDA/cellN films with average growth rates of 14 and 19 nm/BL, respectively. For these films the surface roughness increases with thickness, which compromises the accuracy of ellipsometry measurements. Hence, for films thicker than one μm we determined their thickness by extrapolating the data in Figure 3.1A according to the number of bilayers deposited. It should also be noted that the diameter of cellN is roughly 5 nm while a typical polymer chain lying flat on a surface would occupy a space perpendicular to that surface

measuring between 1 and 2 nm. Hence, assuming monolayers of polymer and cellN, the minimum thickness of a bilayer would be 6–7 nm, leaving 8–13 nm of unaccounted growth per bilayer. We attribute this extra growth predominantly to the agglomeration of cellNs, as will be discussed later. Films were grown up to 3 μm to show the change of elastic properties as a function of film thickness; Figure 3.2 is an example of Brillouin spectrum of the anti-Stokes peaks for $[PDDA/cellN]_{95}$.

Film growth was also monitored using QCM. Figure 3.1B shows the change in resonant frequency of the quartz crystal after each deposition step for PDDA/cellN, PDDA/cellN/PDDA/PSS and PDDA/PSS films. The closed symbols indicate the change in frequency after polymer deposition and the open symbols indicate the change in frequency after cellulose deposition. According to the Sauerbrey equation (Eq. 2.1) a larger change in the frequency of the crystal corresponds to a larger change in mass. Figure 3.1B illustrates that compared to the polymer layers, the cellN layers contribute significantly more to the increase in mass. Therefore, increasing the relative number of cellN layers, or volume fraction of cellN, should result in an increase in film density, and this has indeed been found as shown in Table 3.1.

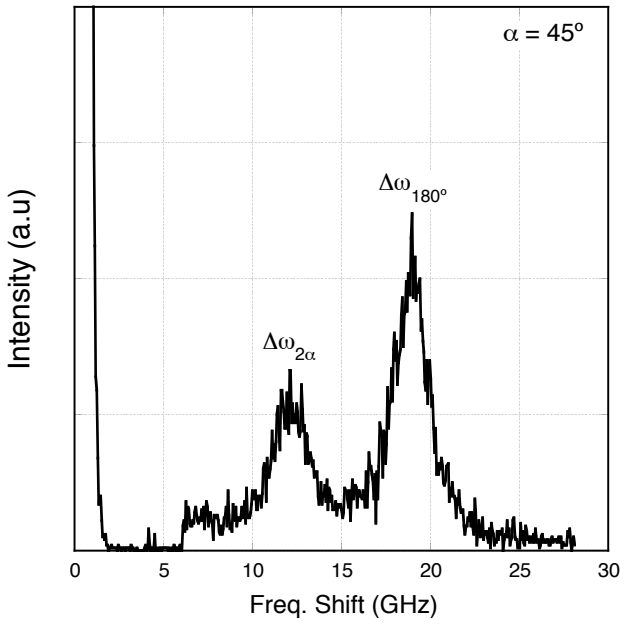

Figure 3.2: An exemplary Brillouin spectrum for chit/cellN on a Si wafer taken in the backscattering geometry. Peaks correspond to frequency shifts from 2α and 180° longitudinal acoustic phonons[a].

Table 3.1: Refractive indices and density of (polymer/cellN)$_x$/(polymer/PSS)$_y$ LBL composites

		x = 0 y = 1	x = 1 y = 9	x = 1 y = 1	x = 4 y = 1	x = 1 y = 0
Chit	n	1.54	1.56	1.47	1.50	1.56
	ρ (g/cm^3)	1.06±0.04	1.16±0.04	1.29±0.017	1.30±0.024	1.36±0.022
	% V_f	0	28.4±1.42	66.1±2.83	69.4±1.8	73.8±2.73
PDDA	n	1.60	1.46	1.55	1.55	1.55
	ρ (g/cm^3)	0.87±0.018	1.21±0.006	1.38±0.023	1.40±0.015	1.44±0.076
	% V_f	0	37.1±0.18	68.4±2.92	79.4±0.77	84±0.9

3.2 Effect of thickness on Elastic Modulus of Rod-like LBL Films

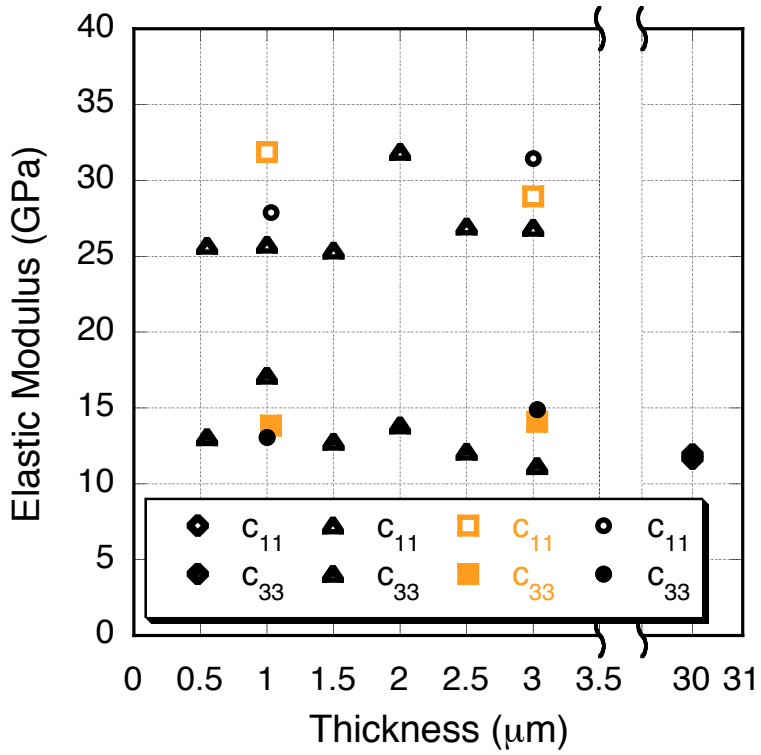

Figure 3.3: Elastic modulus of chit/cellN films as a function of thickness for as-is and heat-treated films.

◇ ◆ - Cast chitosan film

△ ▲ - chit/cellN set A

□ ■ - chit /cellN set B

□ ■ - chit /cellN set B after heat-treatment

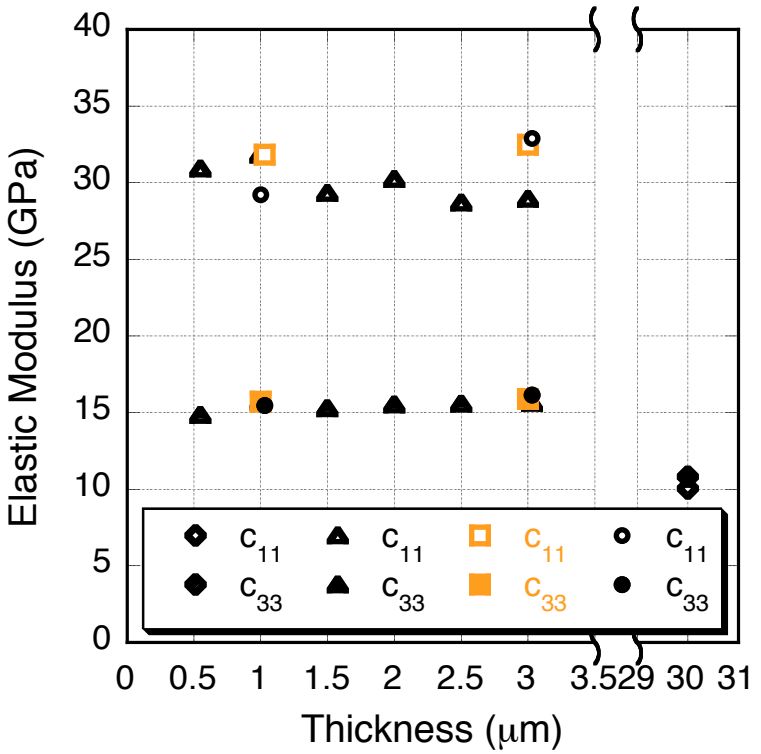

Figure 3.4: Elastic modulus of PDDA/cellN films as a function of thickness for as-is and heat-treated films.

◇ ◆ - Cast PDDA film

△ ▲ - PDDA/cellN set A

□ ■ - PDDA/cellN set B

□ ■ - PDDA/cellN set B after heat-treatment

Figures 3.3 and 3.4 show the elastic moduli of chit/cellN and PDDA/cellN composites, containing 73.8 and 84 vol. % cellN, respectively, as a function of film thickness between 0.5 – 3 μm. Recall that c_{xx} represent the longitudinal elastic moduli in x-direction as defined in Figure 2.2, i.e., c_{11} is the elastic modulus in the growth plane of the film and c_{33} is the one in the growth direction. Our measurements reveal significant anisotropy between the elastic responses of LBL films in-plane and in growth direction. To verify whether this anisotropy is the result of the LBL structure or whether it is inherent to the polymer itself, we cast pure PDDA and chitosan films of approximately 30 μm thickness and measured their elastic moduli. For comparison, the corresponding data points are juxtaposed in Figures 3.3 and 3.4 to those that characterize the various LBL films.

We find that the elastic modulus ratios, c_{11}/c_{33}, for cast PDDA and chitosan films are approximately 1, suggesting that the cast films of pure polymer are indeed elastically isotropic. If there was any unidirectional setting and drying of cast films it did not result in any significant elastic anisotropy. In comparison, for LBL films containing cellN the stiffness in the growth plane is approximately a factor of two larger than in the growth direction for both the chitosan and PDDA system. Within the layers stiffness is enhanced due to the spatial overlap between the high-modulus embedded fibers in the direction of strain, i.e., any arbitrary cross-section perpendicular to this direction will intersect fibers, while the polymer in adjacent layers serves to transmit load between fibers, both laterally and end-to-end. In general terms, we should therefore expect the in-plane modulus to be that of elastic components acting in parallel, i.e., an appropriately weighted average of the polymer and fibers moduli. Conversely, in the growth direction, the fibers do not

stretch across all layers, and their load-bearing ability is distinctly interrupted by the polymer layers. In this direction we would expect the elastic response of the film to be dominated by the most compliant constituent, as expected for components with different stiffness configured in series, where the reciprocals of the moduli of polymer and fibers, prorated according to their relative effective proportions, are additive. A detailed numerical model describing the elastic behavior of these films is derived in section 4.4.

However, first we note that here are significant differences in the extents to which these anisotropies are manifest in LBL films, depending whether they involve PDDA or chitosan polymer layers. The elastic moduli in the growth planes (c_{11}) are about 2 and 3 times that of the corresponding cast films for chit/cellN and PDDA/cellN, respectively. The average c_{33} for PDDA/cellN films is about 50% higher than that of cast PDDA film, whereas the average c_{33} for chit/cellN films is roughly the same as for the cast chitosan film. Addition of cellN fibers therefore has a significantly more dramatic effect on both the in-plane and out-of-plane elastic properties of PDDA/cellN LBL films than those of chit/cellN films. Presumably, this is the result of the differences in adhesion between fiber and polymer facilitating a better fiber-to-matrix load transfer in the case of PDDA/cellN composites, either through larger contact areas or stronger bonding. This interpretation of the elastic modulus data is consistent with observations made from mass adsorption using the QCM. The average change in resonance frequency per added polymer layer is ~5.2 Hz for chit/cellN, while it is ~11.2 Hz for PDDA/cellN, indicating that more than twice the amount of PDDA adheres to the cellN (surface of the film) per deposition step. Similarly, the average per-layer change in resonance frequency for cellN is ~116 and 162 Hz for chit/cellN and PDDA/cellN, respectively. Other processing

parameters, such as cellN solution used, film thickness, and heat-treatment do not have a significant effect on the stiffness for either film. The invariance of the modulus as a function of film thickness is in agreement with previous findings of isotropic and layered thin films using BLS.[7,8]

3.3 Effect of cellN Volume Fraction on Elastic Modulus

Several factors can contribute to the contrasting elastic responses of nano-composites in which otherwise identical fibers are sandwiched between PDDA or chitosan layers. These include differences in wetting or bonding behavior between fiber and polymer, the formation of different in interfacial structures, or dissimilar permeation of the solution into previously deposited layers upon dip coating, possibly resulting in different fiber orientation. To gain further insight and possible explanations for the observed behaviors, we measured the elastic moduli as a function of cellN volume fraction, and analyzed the results in terms of simple mechanical models. Layers of PSS were incorporated to create $[(\text{polymer/cellN})_x/(\text{polymer/PSS})_y]$ structures (referred to as polymer/cellN/PSS films here) with variable number of cellN layers, while the total thickness of the films was held modulus at 1 μm; in other words, the individual polymer layer thickness varies while the cellN layer thickness remains the same.

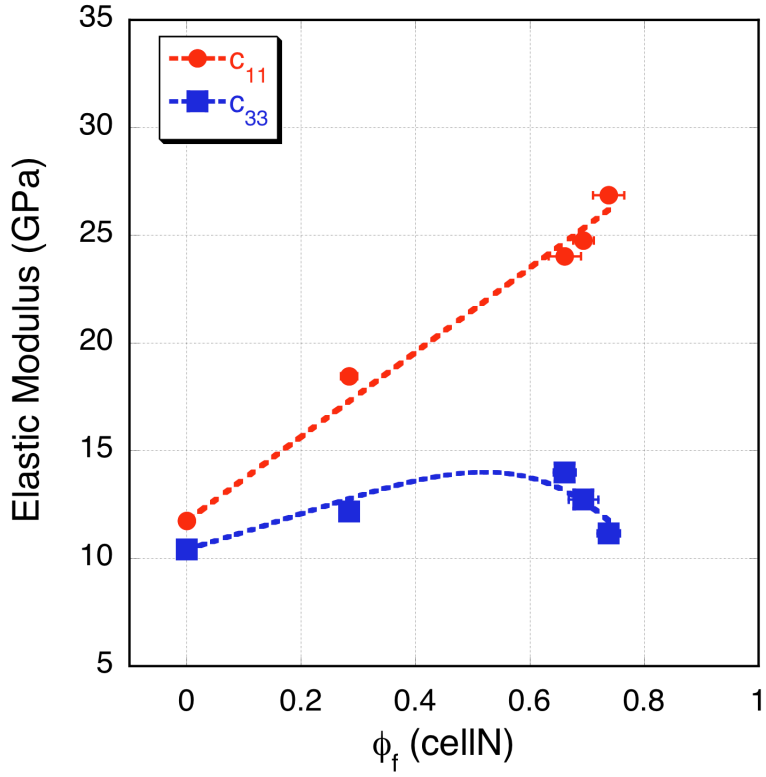

Figure 3.5: Elastic modulus of $[(chit/cellN)_x/(chit/PSS)_y]$ films as a function of cellN volume fraction

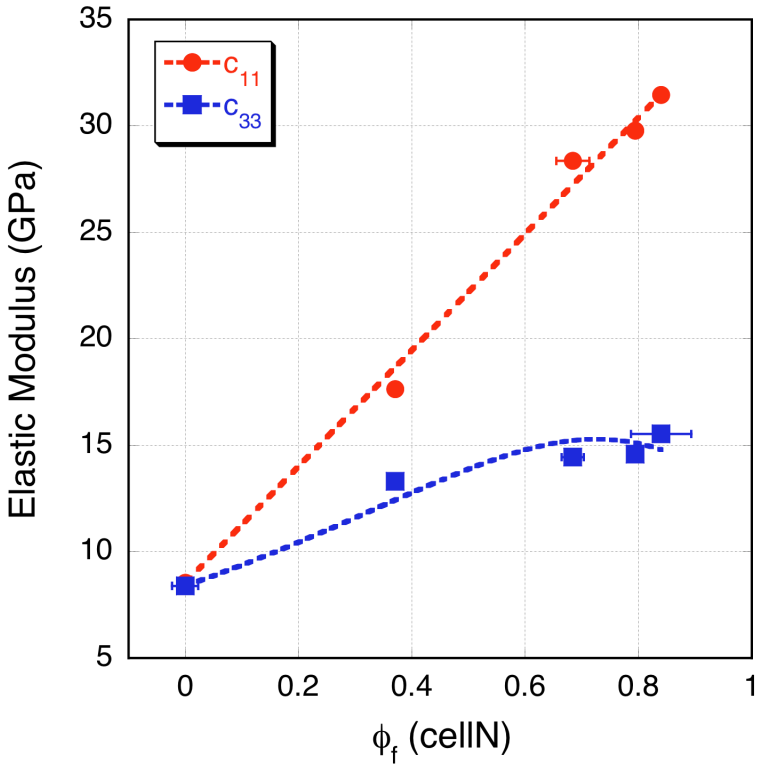

Figure 3.6: Elastic modulus of $[(PDDA/cellN)_x/(PDDA/PSS)_y]$ films as a function of cellN volume fraction

Figures 3.5 and 3.6 show the in- and out-of-plane elastic moduli of [(polymer/cellN)$_x$/(polymer/PSS)$_y$] as a function of cellN volume fraction, ϕ_f, where 'polymer' refers to either chitosan or PDDA. Therefore for $\phi_f = 0$, the LBL film is a polymeric film of either PDDA/PSS or chit/PSS bilayers without any fibers added and at $\phi_f = 1$ the system contains no polymer; the fibers held together solely by Van der Waals forces or chemical bonding in case fibers were not fully separated during hydrolysis. c_{11} increases fairly linearly with increasing amount of cellN, this effect is observed previously for mixed cellulose or cellN reinforced polymer composites, where the in-plane modulus grew from 1.5 GPa to 20 GPa with increasing amount of cellulose.[9-13] c_{33} increases with increasing amounts of cellN as well for both systems, but at a rate that is slower than that of c_{11}. Accordingly, the addition of cellN always provides an initial increase in stiffness in the growth direction. However, the beneficial effect on the composite stiffness due to increasing the amount of cellN eventually subsides for lack of sufficient bonding agent linking the fibers. This can be observed particularly in the case of chit/cellN/PSS films where the out-of-plane elastic modulus (c_{33}) reaches a maximum and starts to tail off at around 60% fiber volume concentration. By contrast, a decrease in c_{33} for PDDA/cellN films is not observed within the achievable range of fiber loadings. This supports our earlier claim that a better fiber-to-matrix load transfer occurs in the PDDA/cellN films because a higher density of contact points is achieved in the thicker individual PDDA layers.

3.4 Modeling of Concentration Dependence on Elastic Modulus

In order to interpret our data in terms of the structural definition of the interfaces in these multi-layer films, specifically the degree of intermixing of polymer and cellN layers, we explored various approaches for modeling the observed elastic characteristics. The model that best describes our findings is derived in the following. As stated above, the initial premise for this model was that the in-plane modulus could be closely described by elastic elements in parallel, whereas the out-of-plane modulus would more likely involve elastic elements in series. We then refined the corresponding expression to account for deviations from these simplified assumptions based on our perception of the structural developments that take place during LBL deposition. Hence, we begin with the expressions

$$c_{11} = \phi_f M_f^{//} + \left(1-\phi_f\right) M_p^{//}, \text{ and} \tag{3.1}$$

$$c_{33} = \left(\frac{\phi_f}{M_f^{\perp}} + \frac{\left(1-\phi_f\right)}{M_p^{\perp}} \right)^{-1}, \tag{3.2}$$

where $M_f^{//}$ and $M_p^{//}$ are the effective longitudinal elastic moduli of the fiber and the polymer layers, respectively, as they contribute to the in-plane composite modulus, while $M_f^{\perp}$ and $M_p^{\perp}$ are the effective moduli of the two layers as they contribute to the out-of-plane composite modulus. Note that by assuming the polymer volume fraction to be $\phi_p = 1-\phi_f$ we ignore the porosity of the film in the material balance. However, the effect of porosity is implicitly accounted for upon evaluating the magnitudes of the fiber and polymer layer moduli.

Because of its amorphous structure, the properties of the polymer phase are isotropic and the elastic modulus is independent of direction, thus, $M_p^{//} = M_p^{\perp} = M_p$. On the other hand, the elastic properties of a single cellN are anisotropic; the axial modulus of the fiber is much higher than the radial one.[3] During LBL deposition, fibers are deposited so that their length axes orient randomly within the space defined by the two in-plane dimensions.[5] Even though that would still provide for an isotropic modulus within the plane, its magnitude deviates from the axial modulus of the fiber. There are a number of models, most notably the Voigt-Reuss,[14,15] Halpin-Tsai,[16] and Cox models,[17] that describe the stiffness of randomly oriented short fibers embedded in a continuous matrix as a function of the fiber concentration. Cox's shear-lag concept provides a correction η_L to the effective modulus of a composite to account for the incomplete load transmission between fiber and matrix, as these strain by different amounts due to their different moduli, i.e.,

$$\eta_L = 1 - \frac{\tanh(\beta l/2)}{\beta l/2}, \tag{3.3}$$

where $\beta = \left[\frac{2G_p}{R^2 M_A \ln(r/R)}\right]^{1/2}$. Here l and R are the length and radius of the fiber, respectively, r is the interfiber spacing, G_p is the shear modulus of the polymer matrix, and M_A = 120 GPa is the axial modulus of the fiber. Krenchel[18] built onto Cox's model and corrected for the effect of non-uniform fiber orientation by introducing the factor

$$\eta_0 = \sum_n a_n \cos^4 \theta_n, \tag{3.4}$$

where a_n is the ratio of fiber with an orientation of angle θ_n. For a 2D system of randomly oriented in-plane fibers with lengths of 300 nm, η_L and η_0 are 0.932 and

0.375, respectively. Unlike traditional composites, however, in our LBL films cellN fibers are only partially embedded in the polymer of the adjacent layers. Within the fiber layer there may be regions of overlapping fibers and incomplete polymer penetration. The stiffness reduction due to this porosity is accounted for by introducing the factor η_P. The expression for the in-plane modulus then adjusts to

$$c_{11} = \phi_f \eta_p \eta_0 \eta_L M_A + \left(1-\phi_f\right) M_p . \tag{3.5}$$

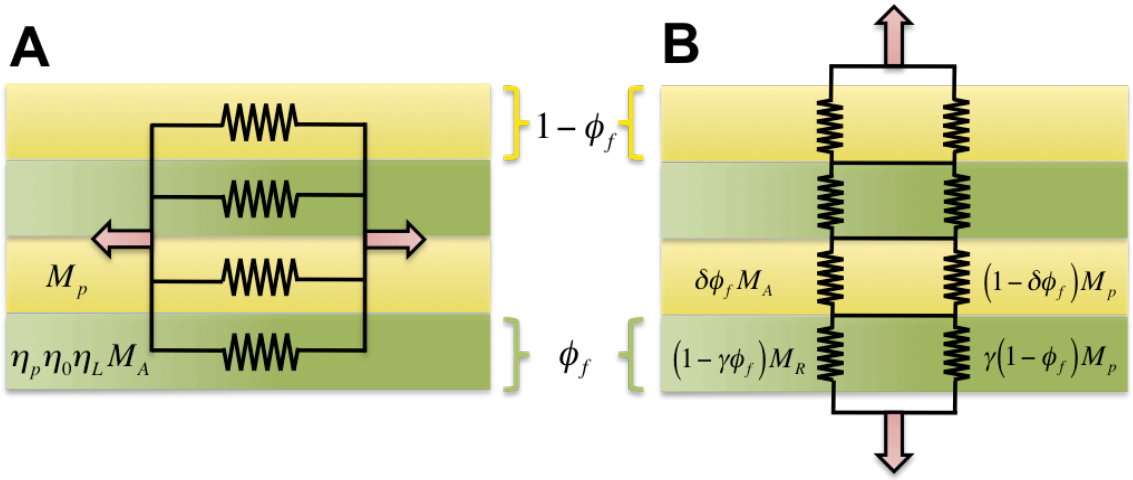

Figure 3.7: A) Springs in parallel for elastic modulus in the growth plane; B) springs in series with mixed springs in parallel (as a function of volume fraction) for elastic modulus in the growth direction where the yellow and green are the volume fractions of the polymer and fiber, respectively.

While this expression for the in-plane stiffness is entirely compatible with the traditional rules-of-mixture for elastic elements in parallel, i.e., it describes a linear dependence of elastic modulus on the volume fraction of fibers, the observed out-of-plane stiffness deviates from what a combination of elastic elements in series would predict, especially for chit/cellN where the modulus decreases at high fiber loading. We attribute this to the fact that the individual layers deposited during the LBL process do not form a sharply defined interface with each other, but that there are high levels of interpenetration of fibers into the polymer layer and polymer into the fiber layer. To

account for this mixing of elastic properties, we model the effective moduli for each type of layer in the out-of-plane direction as an appropriately weighted set of elastic elements in parallel, an illustration of the mixed elastic properties can be seen in Figure 3.7. The polymer that infiltrates the fiber layer is assumed to enhance the load transmission between cellN fibers to an extent that is proportional to the overall polymer volume fraction, i.e., the polymer contributes a factor $\gamma\left(1-\phi_f\right)$ of its modulus to $M_f^{\perp}$, so that

$$M_f^{\perp} = \left(1-\gamma\phi_f\right)M_R + \gamma\left(1-\phi_f\right)M_p, \tag{3.6}$$

where M_R is the stiffness of cellN in the radial direction (30 GPa). As ϕ_f approaches unity, i.e., little or no polymer is available to transmit load between fibers, weak dispersive interactions between fibers take over. This is reflected by the factor $\left(1-\delta\phi_f\right)$. Similarly, the polymer layers benefit from the stiffness of the fibers to an extent that is proportional to overall volume fraction of fibers, i.e., $\delta\phi_f$. As ϕ_f approaches zero, the contribution from fibers to the stiffness vanishes while that from polymer increases as $\left(1-\delta\phi_f\right)$. Consequently,

$$M_p^{\perp} = \delta\phi_f M_A + \left(1-\delta\phi_f\right)M_p. \tag{3.7}$$

The expression for the out-of-plane elastic modulus can then be written as,

$$c_{33} = \left\{\frac{\phi_f}{\left(1-\gamma\phi_f\right)M_R + \gamma\left(1-\phi_f\right)M_p} + \frac{1-\phi_f}{\delta\phi_f M_A + \left(1-\delta\phi_f\right)M_p}\right\}^{-1}. \tag{3.8}$$

Table 3.2: Effective elastic moduli of chit/cellN and PDDA/cellN composites

	η_P	γ	δ
Chit/cellN	0.24	0.914	9.85×10^{-4}
PDDA/cellN	0.28	0.594	0.023

The curves representing the best fits of Eqs. 3.5 and 3.8 to the measured data are shown in Figures 3.5 and 3.6 for chit/cellN and PDDA/cellN films, respectively. Table 3.2 gives a list of the fitting parameters η_P, γ, and δ, respectively. In general, γ assumes larger values than δ, which we interpret to mean that the polymer enhances the stiffness of the fiber layer more significantly than fibers affect that of the polymer layer. This makes sense in that we expect the fiber layer to have some porosity, allowing for the polymer to infiltrate the fibers. γ is larger for chit/cellN/PSS than for PDDA/cellN/PSS films, suggesting that it is easier for chitosan to penetrate the fiber layer than for PDDA. This is also supported by the QCM data, according to which the average deposition rate for a cellN layer is lower for that of chit/cellN films, indicating a more porous cellN layer and thus allowing for more polymer penetration. The situation is, however, reversed as far as the magnitude of δ is concerned. Accordingly, during deposition the fibers become more deeply embedded in PDDA than in chitosan, and in fact, the fiber axes deviate more strongly from the in-plane orientation in the PDDA composite. We can therefore expect that the interface between fibers and polymer for PDDA is more diffuse and intermixed, and overall forming a mechanically stronger connection than for chitosan. This would also explain why at high fiber loadings the out-of-plane modulus in the PDDA system is larger than that of pure PDDA, while this is not the case for the chitosan system. The small values of δ for both systems suggests that eq. (13) in combination with $M_p^{\perp}$; M_p may be sufficient to describe the data for $c_{\perp}$. However, eq. (14) was introduced to

account for the possibility that, depending on the sequence of layer depositions, polymer infiltrating the fiber layer may result in a different structure than fibers immersing into the polymer layer. This asymmetry is preserved by eq. (14), which indeed provides a better fit to the data for the PDDA/cellN system, especially at low fiber volume fractions.

3.5 Summary

Brillouin light scattering was used to determine the in-plane and out-of-plane elastic moduli of LBL films with different thicknesses and cellN concentrations, in backscattering geometry. It was found that the incorporation of cellN increases the stiffness of polymer films more significantly in the in-plane direction as compared to the out-of-plane direction, resulting in elastic anisotropy. Interestingly, for the highest fiber loadings, the out-of-plane moduli for PDDA/cellN films show an improvement from cast PDDA while the out-of-plane moduli for chit/cellN films was similar to that of cast chitosan film. This suggests a better adhesion and therefore better load transfer between PDDA and cellN. This is the case independent of the cellN contents of the composites. The difference between the elastic responses of chitosan and PDDA based composites is attributed to the quality and definition of the interface between fiber and polymer layers. In case of the PDDA system this interface is believed to be more diffuse and fibers are deviate more from in-plane orientations, so as to stretch across the interface and embed in the polymer layer. In case of the chitosan system the interface is believed to be better defined and more planar, while some polymer separately infiltrates the fiber layer during deposition.

References

[1] Samir, M. A. S. A.; Alloin, F.; Dufresne, A. "Review of recent research into cellulosic whiskers, their properties and their application in nanocomposite field," *Biomacromolecules* **2005**, *6*, 612-626.

[2] Ishikawa, A.; Okano, T.; Sugiyama, J. "Fine structure and tensile properties of ramie fibres in the crystalline form of cellulose I, II, IIII and IVI," *Polymer* **1997**, *38*, 463-468.

[3] Tashiro, K.; Kobayashi, M. "Theoretical Evaluation of 3-Dimensional Elastic-Constants of Native and Regenerated Celluloses - Role of Hydrogen-Bonds," *Polymer* **1991**, *32*, 1516-1530.

[4] Bledzki, A. K.; Gassan, J. "Composites reinforced with cellulose based fibres," *Prog Polym Sci* **1999**, *24*, 221-274.

[5] Podsiadlo, P.; Choi, S. Y.; Shim, B.; Lee, J.; Cuddihy, M.; Kotov, N. A. "Molecularly engineered nanocomposites: Layer-by-layer assembly of cellulose nanocrystals," *Biomacromolecules* **2005**, *6*, 2914-2918.

[6] Bertrand, P.; Jonas, A.; Laschewsky, A.; Legras, R. "Ultrathin polymer coatings by complexation of polyelectrolytes at interfaces: suitable materials, structure and properties," *Macromol Rapid Comm* **2000**, *21*, 319-348.

[7] Gomopoulos, N.; Cheng, W.; Efremov, M.; Nealey, P. F.; Fytas, G. "Out-of-Plane Longitudinal Elastic Modulus of Supported Polymer Thin Films," *Macromolecules* **2009**, *42*, 7164-7167.

[8] Gomopoulos, N.; Saini, G.; Efremov, M.; Nealey, P. F.; Nelson, K.; Fytas, G. "Nondestructive Probing of Mechanical Anisotropy in Polyimide Films on Nanoscale," *Macromolecules* **2010**, *43*, 1551-1555.

[9] Bataille, P.; Ricard, L.; Sapieha, S. "Effects of Cellulose FIbers in Polypropylene Composites," *Polym Composite* **1989**, *10*, 103-108.

[10] Noishiki, Y.; Nishiyama, Y.; Wada, M.; Kuga, S.; Magoshi, J. "Mechanical properties of silk fibroin-microcrystalline cellulose composite films," *J Appl Polym Sci* **2002**, *86*, 3425-3429.

[11] Nishino, T.; Matsuda, I.; Hirao, K. "All-cellulose composite," *Macromolecules* **2004**, *37*, 7683-7687.

[12] Uesaka, T.; Nakane, K.; Maeda, S.; Ogihara, T.; Ogata, N. "Structure and physical properties of poly(butylene succinate)/cellulose acetate blends," *Polymer* **2000**, *41*, 8449-8454.

[13] Yamanaka, S.; Watanabe, K.; Kitamura, N.; Iguchi, M.; Mitsuhashi, S.; Nishi, Y.; Uryu, M. "The Structure and Mechanical-Properties of Sheets Prepared From Bacterial Cellulose," *J Mater Sci* **1989**, *24*, 3141-3145.

[14] Reuss, A. "Account of the liquid limit of mixed crystals on the basis of the plasticity condition for single crystal," *Z Angew Math Mech* **1929**, *9*, 49-58.

[15] Voigt, W. "The relation between the two elastic moduli of isotropic materials," *Ann Phys* **1889**, *38*.

[16] Matthews, F. L.; Rawlings, R. D. *Composite Materials: Engineering and Science*; Woodhead Publishing Limited: Abington Hall, 1999.

[17] Cox, H. L. "The Elasticity and Strength of Paper and Other Fibrous Materials," *Brit J Appl Phys* **1952**, *3*, 72-79.

[18] Krenchel. *Fibre Reinforcement*; Akademisk Forlag: Copenhagen, 1964.

CHAPTER 4

Elastic Modulus of Sphere-like Particles in LBL Films

The ability to layer configurations in LBL films down to the nanometer scale allows one to create highly precise composite structures for a wide variety of applications, ranging from ultra-strong films to photonic crystals.[1,2] In the previous chapter, we have shown that the mechanical properties of LBL films depend on the directionality of the film as well as the deposition parameters. However, film thickness and heat treatment had little effect on the elastic moduli.[3] In this chapter, silica nanoparticles of various sizes were paired with polymers of various thicknesses to study the effects of geometry and packing behavior on the mechanical properties of LBL films.

4.1 Film Growth and Characterization

4.1.1 Particle Size and Distribution

Prior to making the films, the monodispersity of SiO_2-NP was determined using a Zetasizer, which allows one to measure the hydrodynamic size of nanoparticles using dynamic light scattering. It was found that nanoparticles have average diameters of 6.20, 13.38, and 24.17 nm. In this chapter, we will refer to the particle types according to their nominal sizes given by the manufactures, which are 7, 12, and 22 nm, respectively.

Figure 4.1 show TEM images of a single bilayer of PDDA/SiO_2-NP deposited onto a copper grid. The diameters of the SiO_2-NP that can be identified on the TEM images correspond well with those measured using the Zetasizer. The TEM images also provide a qualitative assessment of the non-uniformity in particle sizes. AFM reveals an even and dense coverage for one bilayer of PDDA/SiO_2-22nm, Figures 4.2A-B, it also shows particles of roughly the same size. Similarly, the uniform coverage can be seen in the SEM image of PU/SiO_2-22nm after 133 BL, Figures 4.2C-D.

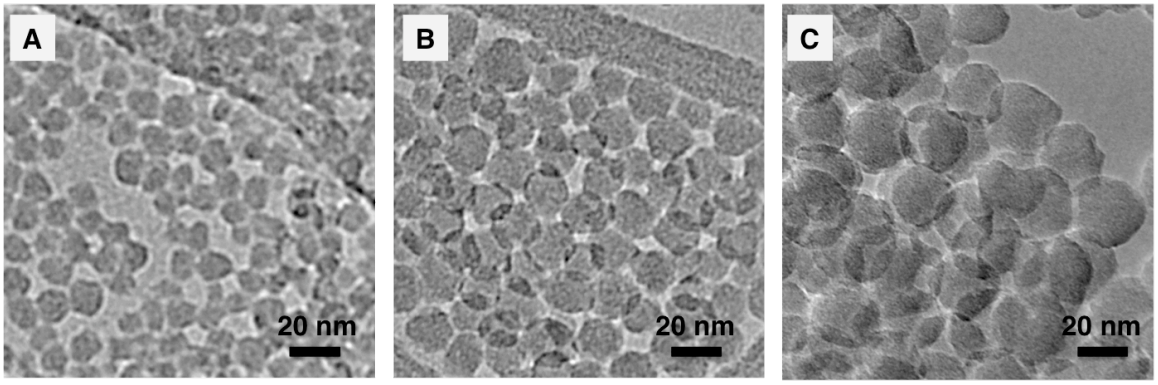

Figure 4.1: TEM of one bilayer of PDDA/SiO_2-NP for 7, 12, and 22 nm SiO_2-NP deposited onto copper grid, respectively.

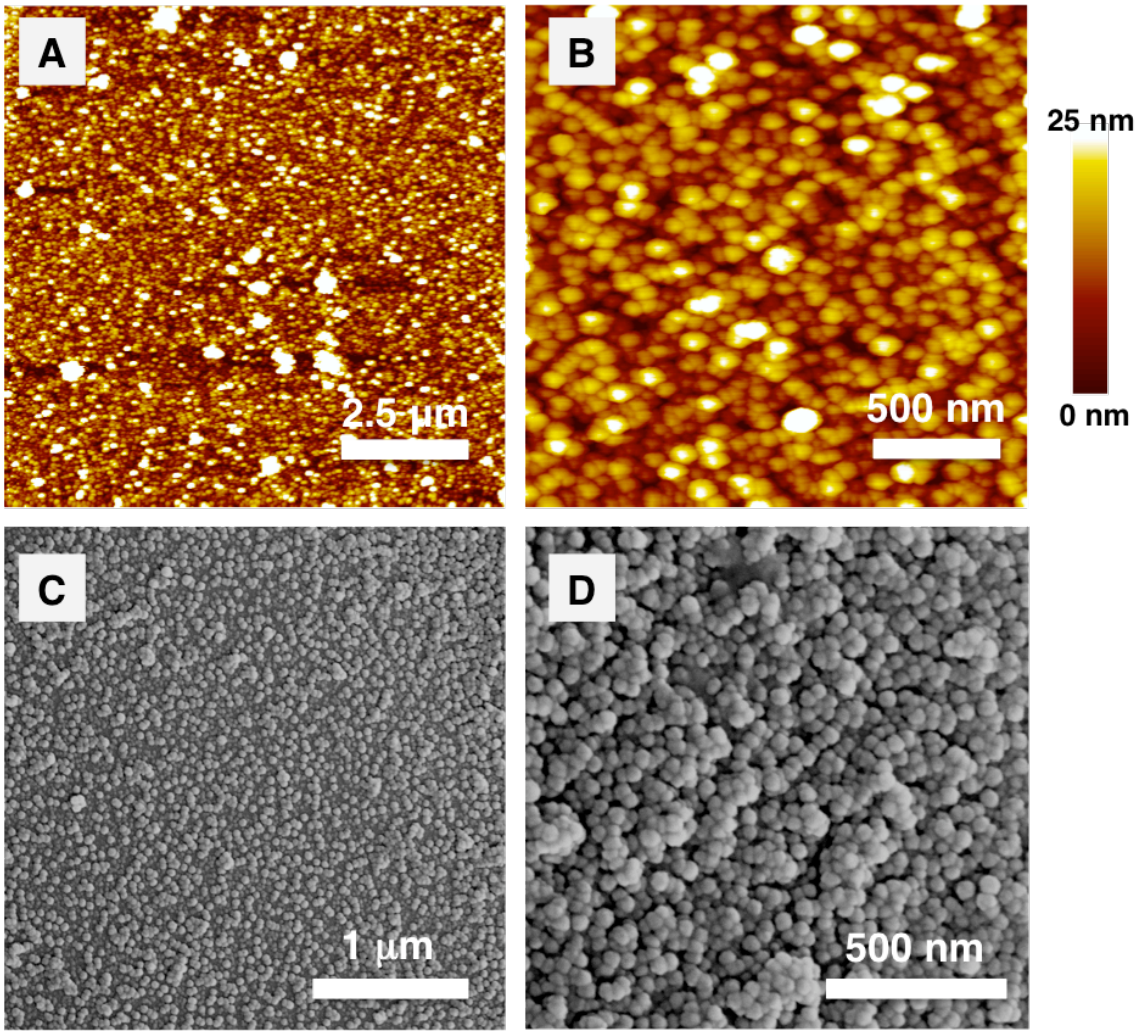

Figure 4.2: Top-down view of SiO_2-NP deposited on Si wafer A-B) AFM image of 1BL of PDDA/SiO_2-22nm and C-D) SEM images of 133 BL of PU/SiO_2-22nm.

4.1.2 UV-Vis Absorbance

The growth of the PDDA/SiO_2-NP films was monitored using UV-vis absorbance, as shown in Figure 4.3A – C. For all three nanoparticle sizes, the absorbance decreased with increasing number of bilayers until it reaches a reversal point, Figure 4.3D, where the absorbance increases with increasing number of bilayers. This trend is typical of materials with anti-reflective (AR) properties.[4-8] The decrease in refractive index is associated with the nanoporous nature of LBL deposited nanoparticle films. For thin film

material, the AR property depends on the thickness of the films. The minima in Figure 4.3D indicate the points of maximum transmittance for each nanoparticle size.

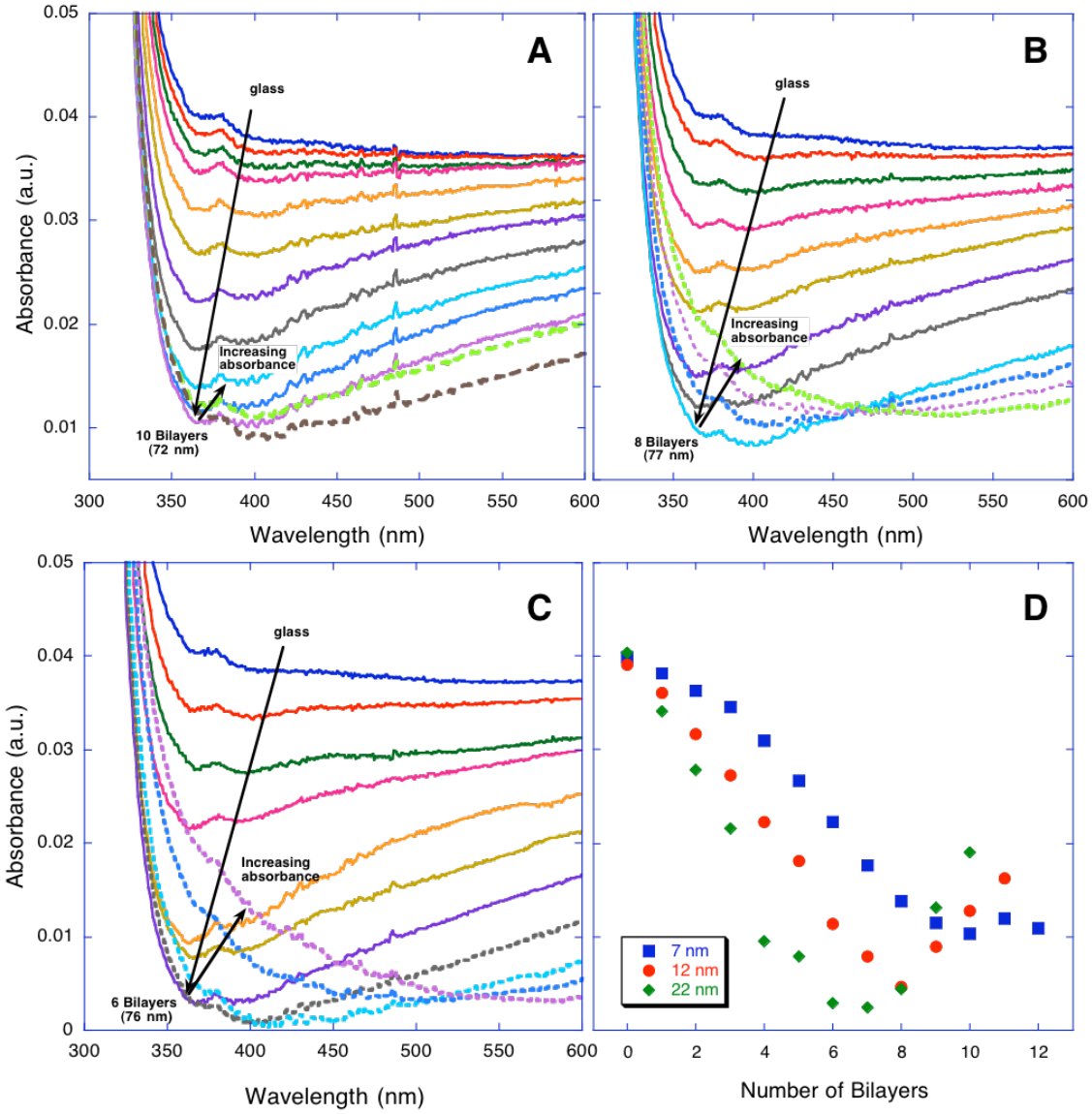

Figure 4.3: A – C) UV-Vis absorption measurements for PDDA/SiO_2-NP with 7, 12, 22 nm diameters. Solid lines: decreasing absorbance with increasing layer thickness. Dotted lines: increasing absorbance with number of bilayers. D) Absorbance at 370 nm as a function of number of bilayers, minimum points can be noticeably seen for each LBL sample.

4.1.3 QCM and Ellipsometry

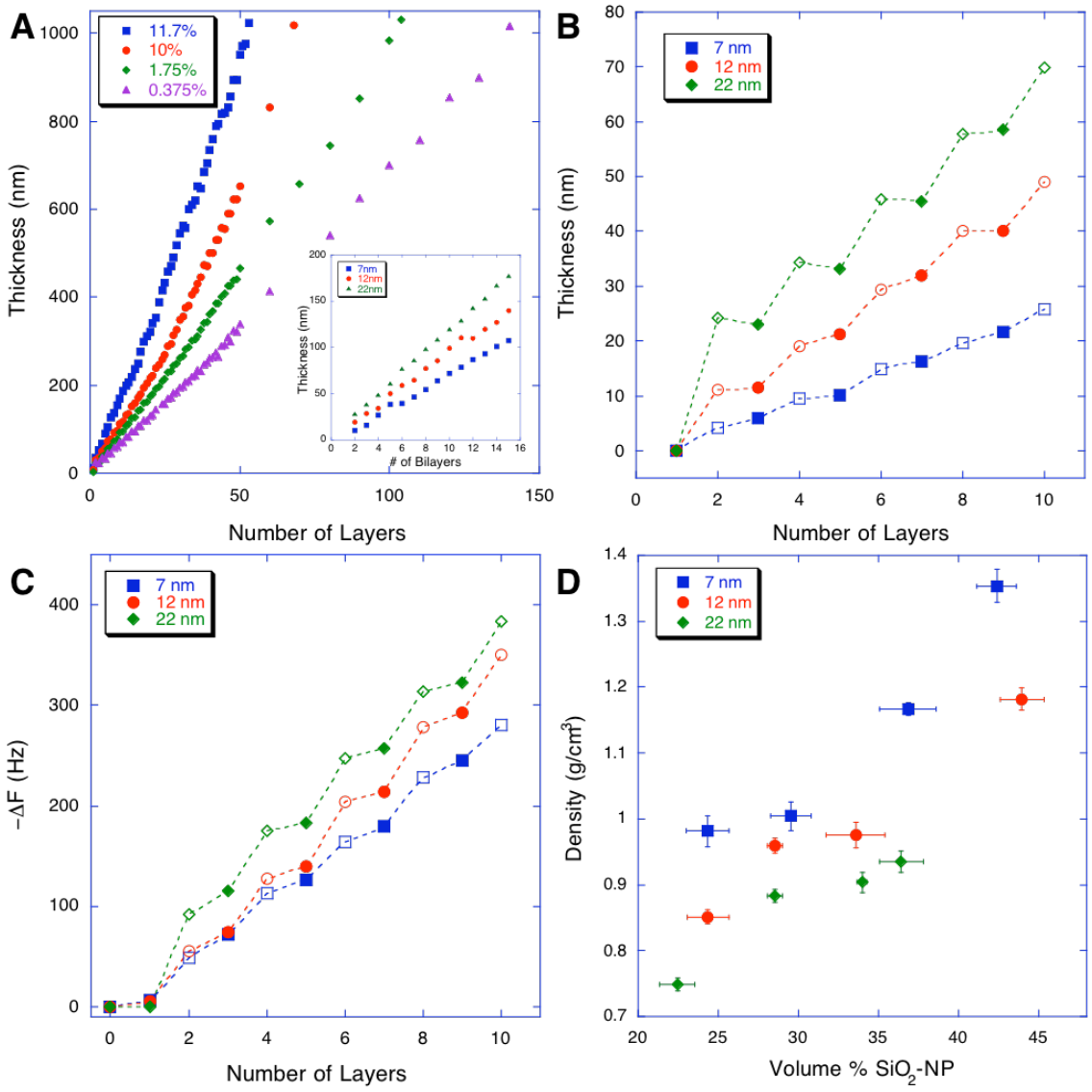

Figure 4.4: A) Thickness vs. the number of layers for PU/SiO_2-22nm, the thickness was obtained using ellipsometry. Insert: thickness measurements as a function of number layers for PDDA/SiO_2-NP samples. B-C) Change in frequency and thickness as a function of number of layers for PU80x/SiO_2-NP, respectively (closed=polymer growth, open=SiO_2-NP growth). D) Film density as a function of SiO_2 volume percent for PU/SiO_2 films.

Film growth was also monitored using ellipsometry and QCM. Figure 4.4A is a plot of film thickness as a function of number of layers for 2.5x, 3x, 17x, and 80x PU dilution (11.7, 10, 1.75, 0.375 wt% PU) and 22 nm SiO_2-NP; a smooth linear growth was

observed for films up to 1 μm in thickness. Similarly, for PDDA/SiO_2-NP with particle sizes of 7, 12, 22 nm in diameter (Figure 4.4A insert) the thickness grows linearly with the number of bilayers. On a per-layer level, the film growth shows more of a "step-ladder" trend; Figure 4.4B shows the film thicknesses of (PU80x/SiO_2-NP)$_5$ as a function of number of layers for all three particle sizes; here the solid symbols indicate the growth after polymer deposition and open symbols the growth after SiO_2-NP deposition. The change in frequency is proportional to the mass of the material deposited in each layer. Accordingly, the deposition of larger SiO_2-NP produces a more rapid increase in film thickness than that of the thinner polymer layer. The thickness increase after the deposition of the SiO_2-NP layer is also proportional to the size of the particles where the average per-layer growth rate is 7.59, 9.51, and 15.2 nm for the 7, 12, and 22 nm sized particles, respectively. For the smallest particle size the thickness that can be attributed to the SiO_2-NP layer is nearly equal to the particle diameter, whereas for the larger particles it is less than their diameters. This could be due to the fact that the larger particles do not cover the substrate surface as densely as the smaller ones upon deposition. While all three particle sizes follow this "step-ladder" trend, the thickness of the film decreases slightly after the deposition of the polymer layer for films created using the 22 nm sized particles. This may be because a new polymer layer does not simply span over the top of the particle layer, but as a result of higher interparticle spacing the polymer solution penetrates into the spaces between SiO_2-NP particles. Thus, the larger SiO_2-NP are also coated on their sides with new polymer. If this coating attaches below the equator, the repulsive forces between this new coating and the previous polymer layer on which the

particles were deposited may cause a small fraction of the SiO_2 spheres to dislodge. This "step-ladder" trend is also reflected in the frequency changes from QCM measurements.

QCM is a common technique used in LBL to determine the amount of material deposited per deposition layer.[9-11] An example of film growth can be seen in Figure 4.4C, the change in frequency is plotted as a function of number of layers for $(PU80x/SiO_2\text{-}NP)_5$. As mentioned previously the change in frequency is directly proportional to the amount of mass deposited for that particular layer. Similar to thickness growth, mass adsorption correlates with expected polymer and SiO_2-NP growth rates. A larger change in frequency is a result of depositing the bigger and heavier SiO_2-NP particles and the deposition of lighter and thinner PU yields a smaller change in frequency. The per-layer mass adsorption increases linearly with the size of the particle: for the 7, 12, and 22 nm sized particles, the average per-layer increase in QCM frequency is 27.6, 49.5, and 82.0 Hz, respectively. Considering the actual average diameter of these particles, this corresponds to a near perfect linear dependence of the per layer mass adsorption on the particle size. Such a dependency would be expected if the packing density of spheres were independent of the particle diameter. Take for example the densest packing of mono-disperse spheres in between two plates that are at a distance equal to the particle diameter. The volume fraction of this space that is occupied by spheres is 0.604, i.e., independent of the particle diameter. The same is true for less densely packed configurations, for as long as the coordinates of the spheres scale with their diameter. Hence, based on the data presented in Figures 4.4B and 4.4C, we can conclude that (i) the SiO_2-NP deposit onto the substrate with self-similar surface coverage density; (ii) this coverage density is significantly lower than closed-packed, and

(iii) the larger the particle diameter, the more the subsequently deposited polymer layer will sag into the gaps between nano-spheres and coat them laterally.

Thickness data paired with QCM data allows us to determine the densities of the films using the Sauerbery equation, as explained in Chapter 2 (Equations 2.1. and 2.2). The volume fractions of SiO_2-NP, polymer, and pores are similarly derived using Equations 2.3-2.8 found in Chapter 2. Figure 4.4D shows the densities of PU/SiO_2-NP as a function of volume percent of SiO_2-NP. The film density increases with increasing SiO_2-NP volume fraction, but decreases as a function of particle size. The increase in density with the amount of SiO_2-NP is to be expected, since more of the higher density constituent is incorporated in the material. However, the decrease of density with increasing particle size suggests that another factor is at play. If we are considering a completely dense material where every particle is surrounded by polymer, at the zero volume percent SiO_2-NP, the density of the material would approach that of pure PU (1.02 g/cm^3) and at 100% SiO_2-NP that of pure SiO_2 (2.2 g/cm^3). However, for all three particle sizes the density dips below the PU density of 1.02 g/cm^3 at a finite volume fraction. This suggests that the films are not fully dense. Instead, there are high levels of porosity associated with the layering aspect of LBL films and this porosity is proportional to the size of the particles. The highly porous nature of nanoparticle LBL films is also supported by the aforementioned anti-reflective properties of nanoporous films from the UV-vis data. A complete listing of volume fractions, refractive indices and densities for each of the films can be found in Table 4.1.

Table 4.1: Volume fraction, refractive indices, and densities of PDDA/SiO_2-NP and PU/SiO_2-NP films

Polymer	Dilution	SiO_2 size (nm)	n	ϕ (SiO_2) ×100	ϕ (poly) ×100	ϕ_{pore} ×100	Density (g/cm^3)
PDDA	1 wt%	7	1.356	48.8	23.3	27.9	1.31
		12	1.313	55.5	15.7	28.8	1.38
		22	1.289	61.6	9.4	29	1.45
		7/22	1.010	48.8	12.9	38.4	1.21
		12/22	1.313	48.2	15.4	37.9	1.22
PU	2.5x	7	1.436	24.3	43.8	31.8	0.98
	3x		1.420	29.5	34.9	35.6	1.00
	17x		1.405	36.9	34.9	28.3	1.17
	80x		1.345	42.4	41.3	16.3	1.35
PU	2.5x	12	1.410	24.5	30.7	44.8	0.85
	3x		1.404	28.5	32.6	38.9	0.96
	17x		1.349	33.6	21.3	45.2	0.98
	80x		1.331	44.0	21.5	34.6	1.18
PU	2.5x	22	1.384	22.5	24.9	52.7	0.75
	3x		1.346	28.5	25.1	46.4	0.88
	17x		1.266	34.0	15.3	50.7	0.90
	80x		1.261	36.4	13.0	50.6	0.94

4.2 Elastic Modulus of SiO_2-NP Films

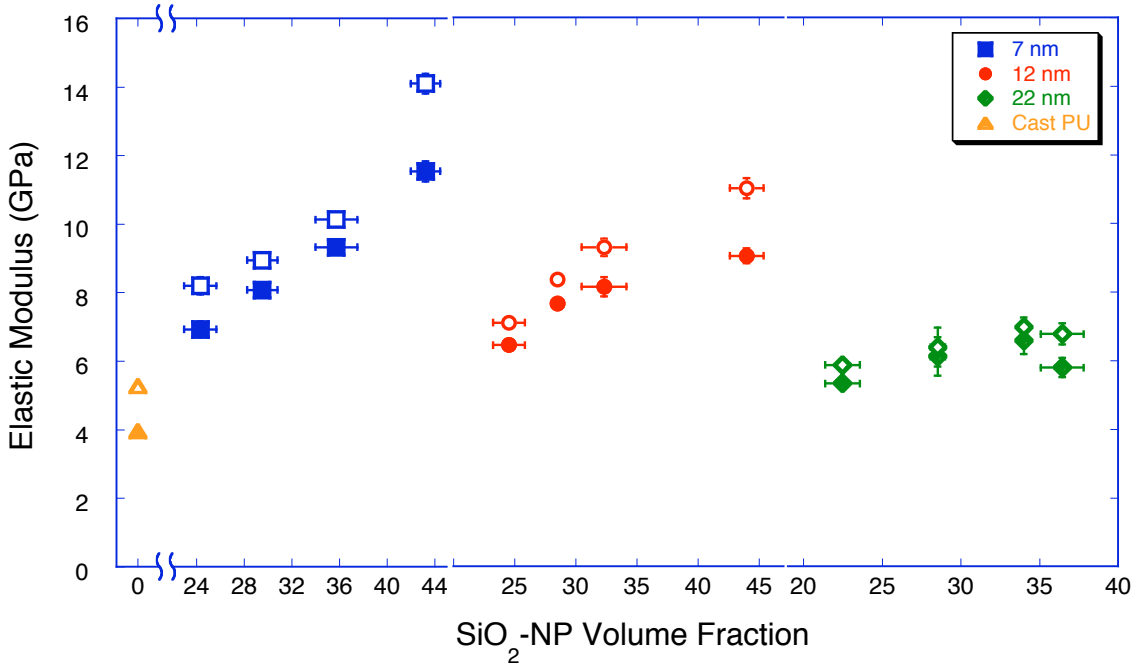

Figure 4.5: Elastic modulus of PU/SiO_2-NP as a function of volume percent of SiO_2-NP. Open = out-of-plane; close = in-plane

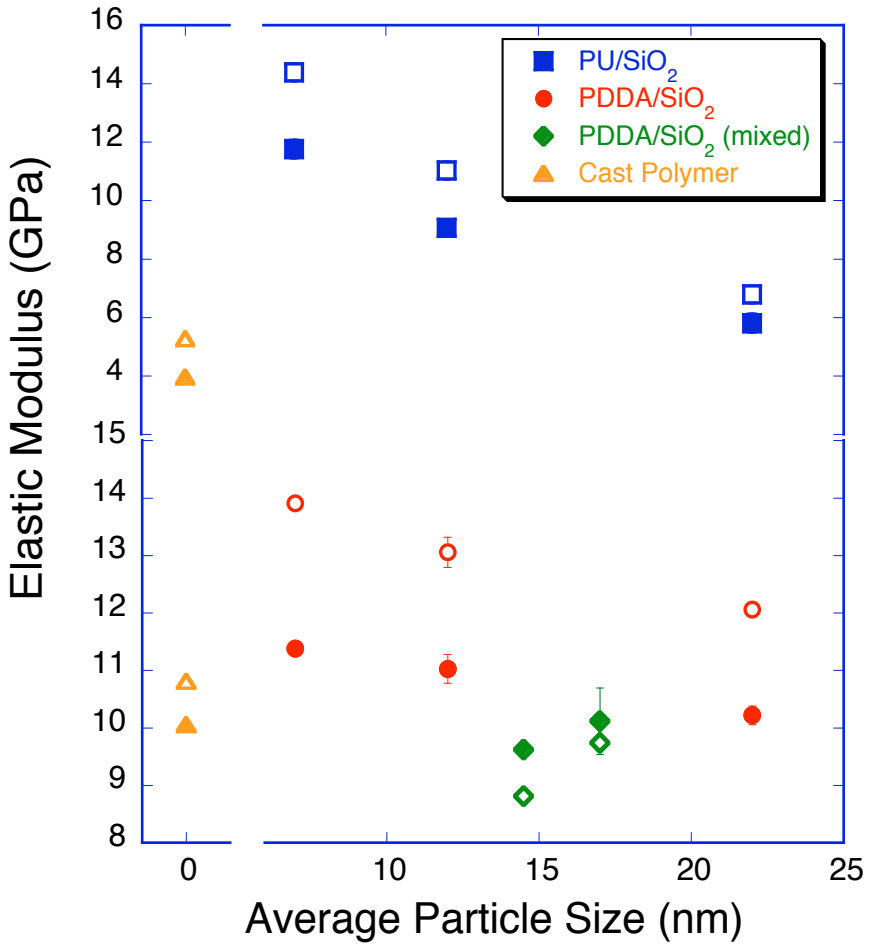

Figure 4.6: Elastic Modulus as a function of particle size for PU/SiO_2-NP, PDDA/SiO_2-NP, and mixed PDDA/SiO_2-NP (the particle size is averaged for plotting purpose), Open = out-of-plane; close = in-plane

The effect of particle size and volume fraction on the elastic modulus of PU/SiO_2-NP and PDDA/SiO_2-NP films can be seen in Figures 4.5 and 4.6. The most noticeable feature from these two figures is that for polymer/SiO_2-NP LBL films the out-of-plane moduli are higher than that of the in-plane moduli for all films containing mono-disperse particle sizes, but not so for the films containing mixed particle sizes. This differs from our previous findings[3] for polymer/cellN LBL films as well as other common composites where the in-plane moduli are higher than that of out-of-plane.[12-16] As a first assumption, this may be because the out-of-plane modulus for PU is higher than its in-plane modulus,

which is translated to the composited films. If this were the case, the composite films with lower SiO_2-NP concentration or thicker polymer layers would yield a bigger difference between the in- and out-of-plane modulus than thinner polymer layers. According to Figure 4.5 this is not so. The opposite is observed for all three particle sizes. Therefore, further explanations are needed to understand this phenomenon.

For composites, load is typically supported by both the fiber and the matrix where the stiffness of the material depends largely on load transfer from the fiber to the matrix.[13,16-18] In particularly in the case of short fiber composites, the effective modulus contribution is significantly reduced as a result of the fiber length, fiber discontinuity, and for LBL films, porosity.[18] In the case of poly/cellN LBL films, the higher in-plane moduli result from the fiber overlapping and the embedded nature of the fibers thus load transfer occurs from fiber to fiber as well as fiber to matrix. For the out-of-plane direction, the stiffness is discontinuity between fibers and the matrix, and the weaker constituent therefore determines the composite modulus. Alternatively, the in and out-of-plane moduli can be also described as springs in series and in parallel, respectively. Similar to the cellulose LBL films, load transfer occurs primarily between the particle and polymer matrix at their contact points. Based on the above packing density analysis we concluded that the interparticle distances within each deposited layer are large. The in-plane gaps between SiO_2-NP may be partially filled with polymer that sags into these gaps, but the space accounts for ~30% porosity in the material, which is close to percolation threshold. Hence, in the growth plane there is very little direct load transfer between the particles. In-plane, the majority load is transferred via the adjacent, top and bottom, polymer layers, which can stretch, flex, and buckle. Moreover, since the SiO_2-

NP are negatively charged across the entire surface, particles can roll on the polymer layer. This great flexibility and variety in the available modes of deformation provides for a large in-plane compliance. Considering rules of mixture for the in-plane elastic properties, due to the spacing between SiO_2-NP these contribute very little to the stiffness in parallel to the polymer layer. To the extent that polymer penetrates into the gaps between particles a certain fraction of the load is transferred between NP-polymer-NP in series. The appropriate model for in-plane modulus would therefore resemble closer that of springs in series. The out-of-plane moduli are higher because there is more direct NP-polymer-NP contact. During deposition SiO_2-NP must settle onto polymer and vice versa. Based on the attractive forces that govern deposition, the mechanical effect of porosity is reduced in the growth direction. Described by a rule of mixture, the out-of-plane modulus includes a stronger element of NP-polymer-NP in series. To the extent that polymer penetrates the gaps between nano-particles, load can be transmitted from NP to polymer to NP via shear forces, allowing for polymer and SiO_2-NP to act in parallel, but the extent to which this is the case may be small. The porosity increases with increasing particle size. Under these conditions the columnar arrangement of nano-particles in growth direction is less likely, which may explain why composites with larger particles exhibit less of a difference between in-plane and out-of-plane modulus.

4.3 Size Effect of SiO_2-NP on Mechanical Properties

Figure 4.5 gives an idea of interfacial effects on the overall mechanical stiffness of nanoparticle LBL films. The volume percent of SiO_2-NP is adjusted by varying the thickness of the PU layer, as controlled by the dilution of the polymer precursor. The

more dilute the precursor solution, the thinner the PU layers, and the higher the SiO_2-NP fraction. The packing density of particles in each layer is indirectly affected by the polymer layer thickness, as detailed below. For low SiO_2-NP content, the PU layers can be as thick as 20 nm or as thin as 1 nm at high SiO_2-NP volume fraction. It should be noted that a minimum of 1 nm in PU layer thickness is necessary for mechanical stability of the film. At first glance, Figure 4.5 resembles that of many modulus vs. fiber volume fraction plots. The addition of more fiber or NP, in this case, yields a higher elastic modulus especially in the case of 7 and 12 nm particles. However, a closer examination of the plot reveals strong correlation between the effect of particle size and volume fraction on the mechanical properties of PU/SiO_2-NP LBL films: modulus increases as a function of SiO_2-NP volume fraction for 7 and 12 nm particles, but stays relatively constant for 22 nm.

This behavior can be explained in the context of the structural model established thus far. First, we should emphasize the fact that the nano-particle volume fraction has a somewhat different meaning than it does for bulk composites produced by a random mixing of the two constituents. Given the importance of polymer layer thickness and coating contour for the mechanical behavior of the films, instead of SiO_2-NP volume fraction it is preferable consider the thickness of the polymer layer as the controlling variable. At the lowest SiO_2-NP concentrations, thick polymer layers provide an even substrate for the adsorption of SiO_2-NP; the coverage density of polymer surface by particles should not be affected by the packing of spheres in the next SiO_2-NP below this polymer layer. This provides high levels of interfacial contact between the particle and polymer, and allows for the initial increase of modulus from the cast PU. The film

stiffness is enhanced by the increase in concentration of the stiffer constituent. This trend is most prominently observed for the smaller particle sizes as with SiO_2-7nm and SiO_2-12nm. As the polymer layer thickness is reduced to achieve higher SiO_2-NP loadings, the polymer surface becomes corrugated, delineating the particles in the layer below. This reduces the surface coverage density by nano-particles. The uneven surface may provide fewer sites for the particles to attach in a stable manner, and the possibility of desorption due to a more circumferential coating of the particles by polymer was mentioned earlier. Importantly, as a result, the porosity of the system increases, as is revealed by the data in Table 4.1. This effect is less noticeable the smaller the size of the nano-particles, because the polymer layer thickness is still large in comparison, even at high dilutions. Thus, the modulus rises faster and more linearly for that of 7 nm SiO_2-NP films, and this trend is only moderately reduced for the 12 nm particles. The change in behavior is most visible for the largest particle size, 22 nm, where the modulus remains relatively constant with the increase in particle concentration. As the particle size increases, the distance between the polymer layers increases. For thick polymer layers, the particles can still be surrounded by a relatively large amount of polymer. When the amount of modulus enhancing component, SiO_2-NP, increases, less polymer is available to "coat" the particles to ensure good load transfer, therefore this would cause the decrease in modulus for larger particles at high volume fraction. Furthermore, the thinner the polymer layer the larger the difference between in-plane and out-of-plane elastic modulus. The thinner the polymer layer, the better the NP-polymer-NP connections, and consequently the load transfer in the out-of-plane direction, while the increasing porosity more strongly affects the in-plane modulus.

4.4 PDDA/SiO_2-NP and PU/SiO_2-NP

The elastic modulus was also determined for PDDA/SiO_2-NP LBL films; Figure 4.6 shows the elastic modulus as a function of particle size for PU and PDDA/SiO_2-NP films. Similar to PU/SiO_2-NP, for standard PDDA/SiO_2-NP films, the in-plane moduli are lower than the out-of-plane moduli. The elastic moduli decrease with increasing particle size for PU/SiO_2-NP films as well as PDDA/SiO_2-NP films. The modulus for PU/SiO_2-NP films decreases more dramatically with increase in particle size than for PDDA/SiO_2-NP films. The most notable feature is that the addition of SiO_2-NP to PU substantially increases its modulus, this was barely the case for PDDA/SiO_2-NP films For instance, in Figure 4.6, the addition of SiO_2-22nm did not enhance the in-plane stiffness of PDDA but for the same particle size this value was increased by a factor of 1.7 for PU/SiO_2-22nm films. This may be attributed to the high modulus of PDDA, while the addition of SiO_2-NP did not help to enhance its modulus, it did not depress this value either. A set of "blended" SiO_2-NP films were also made: [PDDA/SiO_2-7nm/PDDA/SiO_2-22nm] and [PDDA/SiO_2-12nm/PDDA/SiO_2-22nm]. The idea behind this was that the smaller particle layer in between the large particle layers would enhance the interfacial contacts between PDDA and SiO_2-NP as well as lowering the polymer chain mobility in the in-plane direction. Indeed, the corresponding elastic moduli are observed to have a higher in-plane than of out-of-plane value. The increase is more evident for the 7/22nm pairing, which is expected because 7 nm particles are able to filling the in pores better than that of 12 nm particles. While the in-plane modulus is higher for mixed particle films, the moduli of these films are lower than that of the unmixed PDDA/SiO_2-NP films. This may be a result of higher porosity resulting from particle mixing. This shows that the

relationship between in-plane and out-of-plane modulus is primarily the consequence of planar particle packing, while the absolute magnitude of the moduli are dependent on the overall volumetric packing.

4.5 Summary

We have demonstrated the effect of SiO_2-NP size and concentration has on the elastic moduli of PU and PDDA/SiO_2-NP films. Linear grown PU and PDDA/SiO_2-NP films were made using LBL self-assembly. The AR properties of SiO_2-NP films were observed using UV-vis absorbance measurements. It was found AR effect on glass slides exists for film with thickness of at ~70 nm independent of SiO_2-NP size. The in and out-of-plane moduli of SiO_2-NP LBL films were determined using Brillouin light scattering and sphere packing calculations. Several unique trends were observed from the moduli data: 1) the in-plane moduli are lower than the of out-of-plane moduli for all sets of films with the exception of "blended" particle films; 2) out-of-plane moduli increased as a function of SiO_2-NP volume fraction, but more slowly at higher SiO_2-NP concentration; 3) in-plane moduli followed a similar trend to out-of-plane moduli, but for larger particles and at high particle loading, the moduli decrease. These phenomena result from a more significant discontinuity in NP packing in the growth plane than in growth direction. Stronger electrostatic forces in the growth direction, imparting larger energy that is required to pull the polymer away from the particle than energy required to overcome the shear forces between the particle and polymer may account for the higher out-of-plane moduli.

References

[1] Kurt, P.; Banerjee, D.; Cohen, R. E.; Rubner, M. F. "Structural color via layer-by-layer deposition: layered nanoparticle arrays with near-UV and visible reflectivity bands," *Journal of Materials Chemistry* **2009**, *19*, 8920-8927.

[2] Podsiadlo, P.; Kaushik, A. K.; Arruda, E. M.; Waas, A. M.; Shim, B. S.; Xu, J.; Nandivada, H.; Pumplin, B. G.; Lahann, J.; Ramamoorthy, A.; Kotov, N. A. "Ultrastrong and stiff layered polymer nanocomposites," *Science* **2007**, *318*, 80-83.

[3] Sui, L.; Podsiadlo, P.; Huang, L. P.; Kotov, N. A.; Kieffer, J. "Brillouin Light Scattering Investigation of the Mechanical Properties of Layer-by-Layer Assembled Cellulose Nanocrystal Films," *Macromolecules* **2010**.

[4] Cebeci, F. C.; Wu, Z. Z.; Zhai, L.; Cohen, R. E.; Rubner, M. F. "Nanoporosity-driven superhydrophilicity: A means to create multifunctional antifogging coatings," *Langmuir* **2006**, *22*, 2856-2862.

[5] Podsiadlo, P.; Sui, L.; Elkasabi, Y.; Burgardt, P.; Lee, J.; Miryala, A.; Kusumaatmaja, W.; Carman, M. R.; Shtein, M.; Kieffer, J.; Lahann, J.; Kotov, N. A. "Layer-by-layer assembled films of cellulose nanowires with antireflective properties," *Langmuir* **2007**, *23*, 7901-7906.

[6] Zhang, L.; Li, Y.; Sun, J.; Shen, J. "Layer-by-layer fabrication of broad-band superhydrophobic antireflection coatings in near-infrared region," *J Colloid Interface Sci* **2008**, *319*, 302-308.

[7] Zhang, X. T.; Sato, O.; Taguchi, M.; Einaga, Y.; Murakami, T.; Fujishima, A. "Self-cleaning particle coating with antireflection properties," *Chem Mater* **2005**, *17*, 696-700.

[8] Bravo, J.; Zhai, L.; Wu, Z.; Cohen, R. E.; Rubner, M. F. "Transparent superhydrophobic films based on silica nanoparticles," *Langmuir* **2007**, *23*, 7293-7298.

[9] Forzani, E. S.; Otero, M.; Perez, M. A.; Teijelo, M. L.; Calvo, E. J. "The structure of layer-by-layer self-assembled glucose oxidase and Os(Bpy)(2)CIPyCH2NH-Poly(allylamine) multilayers: Ellipsometric and quartz crystal microbalance studies," *Langmuir* **2002**, *18*, 4020-4029-UNSP LA025507X.

[10] Galeska, I.; Hickey, T.; Moussy, F.; Kreutzer, D.; Papadimitrakopoulos, F. "Characterization and biocompatibility studies of novel humic acids based films as membrane material for an implantable glucose sensor," *Biomacromolecules* **2001**, *2*, 1249-1255.

[11] Marx, K. A. "Quartz crystal microbalance: A useful tool for studying thin polymer films and complex biomolecular systems at the solution-surface interface," *Biomacromolecules* **2003**, *4*, 1099-1120.

[12] Buryachenko, V. A.; Roy, A.; Lafdi, K.; Anderson, K. L.; Chellapilla, S. "Multi-scale mechanics of nanocomposites including interface: Experimental and numerical investigation," *Compos Sci Technol* **2005**, *65*, 2435-2465.

[13] de Villoria, R. G.; Miravete, A. "Mechanical model to evaluate the effect of the dispersion in nanocomposites," *Acta Mater* **2007**, *55*, 3025-3031.

[14] Fu, S. Y.; Hu, X.; Yue, C. Y. "A new model for the transverse modulus of unidirectional fiber composites," *J Mater Sci* **1998**, *33*, 4953-4960.

[15] Fu, S. Y.; Lauke, B. "An analytical characterization of the anisotropy of the elastic modulus of misaligned short-fiber-reinforced polymers," *Compos Sci Technol* **1998**, *58*, 1961-1972.

[16] Odegard, G. M.; Clancy, T. C.; Gates, T. S. "Modeling of the mechanical properties of nanoparticle/polymer composites," *Polymer* **2005**, *46*, 553-562.

[17] Garkhail, S. K.; Heijenrath, R. W. H.; Peijs, T. "Mechanical properties of natural-fibre-mat-reinforced thermoplastics based on flax fibres and polypropylene," *Appl Compos Mater* **2000**, *7*, 351-372.

[18] Mathews, F. L.; Rawlings, R. D. *Composite Materials: Engineering and Science*; Woodhead Publishing Limited: Abington, 2000.

CHAPTER 5

Elastic Modulus of Disc-like Particles in LBL Films

The previous two chapters talked about the effects of rod-like or sphere-like particles in LBL films, this chapter will we will talk about the effect of incorporating disc-like particles into linearly grown LBL films. In recent work by Podsiadlo et al., it was demonstrated that polyvinyl alcohol (PVA) when paired with MTM clay and cross-linked using glutaraldehyde created films of extraordinary strength.[1] It is noteworthy that the idea behind this pairing came from nature; the stratus structure of PVA/MTM resemble one of the strongest naturally occurring materials – nacre. Analogous to PVA/MTM films, in this chapter we discuss the concentration effects of MTM clay on the mechanical properties of PU/MTM clay films.

5.1 Film Growth and Characterization

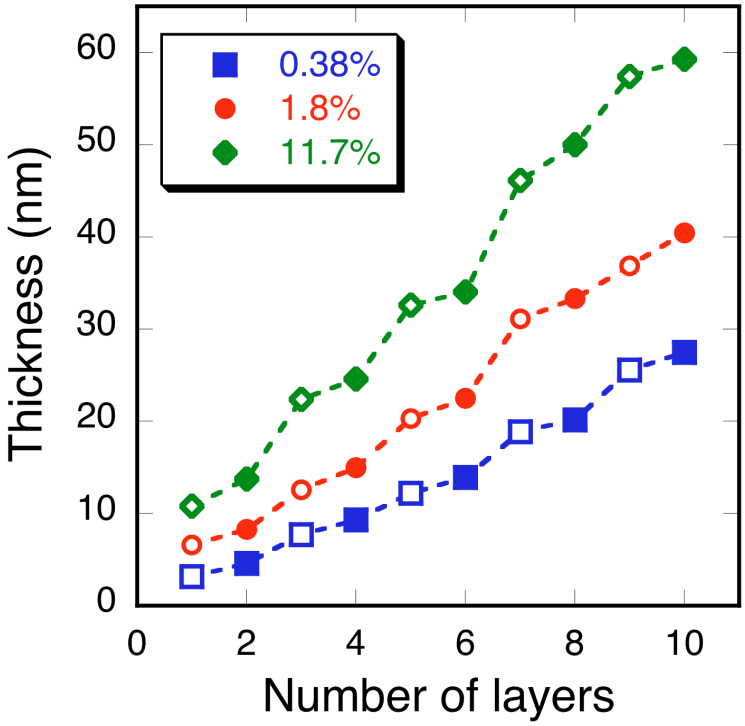

Figure 5.1: Thickness of PU/MTM clay films as a function of number of layers, using 0.38, 1.8 and 11.7 wt% solution concentrations of PU; open = polymer growth, closed = particle growth.

Kaushik et al showed the ability of varying the concentration of PU/MTM films while maintaining the layered stratus of MTM clay.[2] Initial film growth was monitored using Ellipsometry; Figure 5.1 shows the growth rate for the first 10 bilayers of PU/MTM for PU with a concentrations of 0.4, 6.0 and 11.7 wt%. Here, a linear film growth can be seen and the growth rate increases with increasing concentration of PU. This observation is similar to thickness data obtained for these samples using the SEM where for a fixed number of bilayers, the total thickness of the film is proportional to the dilution of PU.[2] The plate-like geometry of MTM clay can be seen in Figure 5.2, where the shape of the clay platelets are fairly irregular with a size of 0.3 – 1 μm in length; one plate is outlined in white and the edge on one plate overlapping another is indicated using an arrow. The volume fraction of MTM clay is calculated from the weight fraction of residual MTM

clay, the densities of clay and polymer using Equation 2.5;[2] a list of the volume fractions of MTM clay and their respective refractive index and densities can be seen in Table 5.1. The mechanical properties of these films were examined using similar BLS measurements as for polymer/cellN and polymer/SiO_2-NP. Figure 5.3 is an example of the Brillouin spectra for cast PU and PU-80x/MTM clay; while the 180º and 2α peaks are clearly visible for both spectra, the sharpness of the peaks diminishes with the addition of MTM clay indicating more diffuse scattering as a result of multiple scattering centers with in the sample.

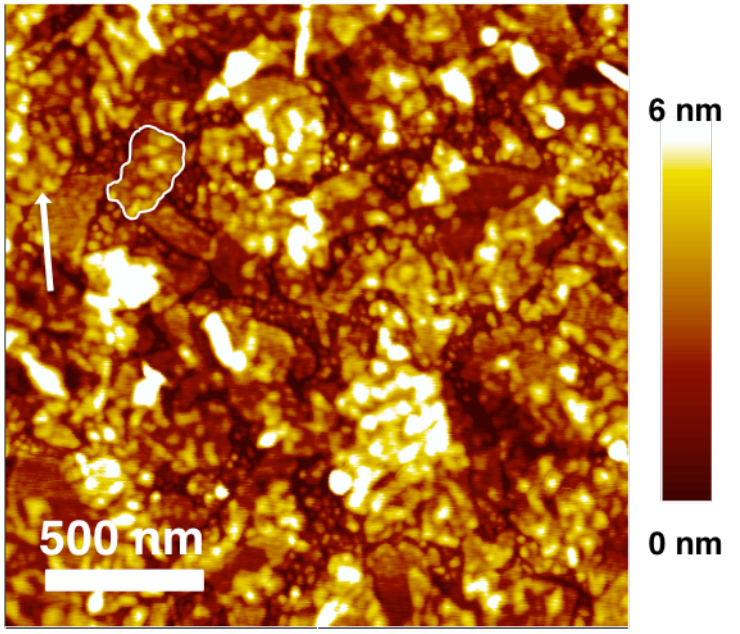

Figure 5.2: AFM image of 1 bilayer of PU-80x/MTM clay. The platelets are distinctive in the image as irregular sheets. A clay platelet is highlighted in white and the arrow indicates a region of clay platelet overlap.

Table 5.1: PU/MTM clay film properties

PU Dilution	PU Concentration	Volume % of MTM Clay	Refractive Index	Density (g/cm^3)
2.5x	11.7 %	5	1.46	1.09
4.3x	10.0 %	7	1.44	1.12
17x	6.0 %	9	1.44	1.14
43x	1.8 %	12	1.43	1.17
65x	0.7 %	20	1.41	1.27
80x	0.4 %	27	1.41	1.36

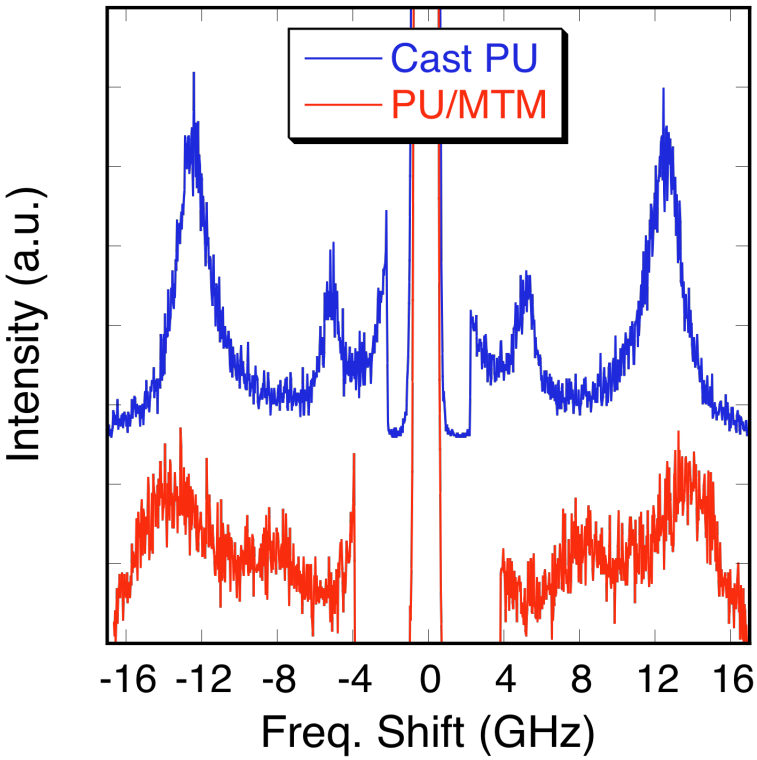

Figure 5.3: An exemplary Brillouin spectrum for $[PDDA/cellN]_{95}$ on a Si wafer taken in the backscattering geometry. Peaks correspond to frequency shifts from 2α and 180° longitudinal acoustic phonons.

Figure 5.4 is a plot of the elastic modulus of PU/MTM as a function of MTM volume fraction. It is evident that the initial addition of clay produced an increase in both the in-plane and out-of-plane modulus compared to the cast PU. However, the rate of modulus increase slows with further incorporation of MTM clay. This produces in-plane modulus vs. particle fraction curves with similar arched shapes than for the out-of-plane modulus. The in-plane modulus curvature deviates from the linear behaviors of systems that obey the traditional rules of mixture. This was also observed in previous work for PU/MTM clay LBL films.[2] On the other hand, Pozsgay[3] and Pukanszky[4] found a similar slow rate of increase of in-plane modulus for their works on clay or talc composites. They gave the decrease in fiber orientation as a possible reason for the deviation from linearity. This explanation is far less likely for LBL thin films, because of the layering process

disorientation of large platelet particles is not possible, and therefore an alternative explanation needs to be provided.

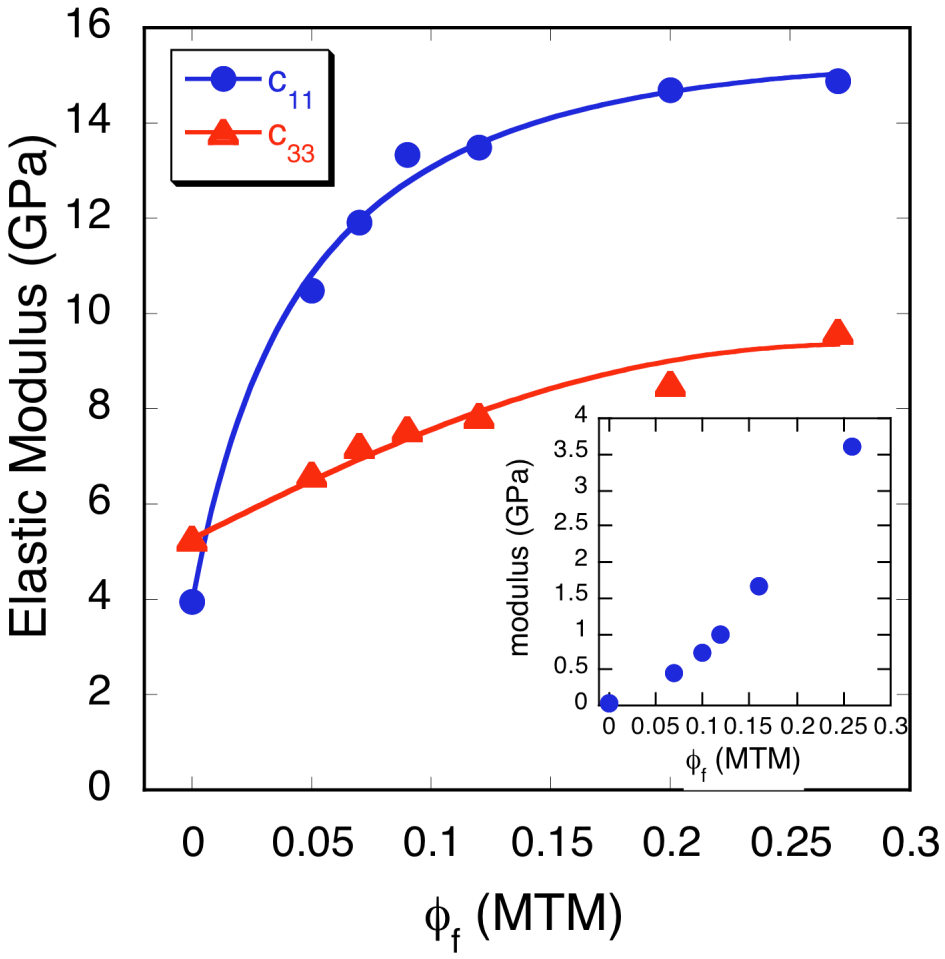

Figure 5.4: Elastic Modulus of PU/MTM clay as a function of MTM clay volume fraction; insert: elastic modulus as a function of MTM volume fraction for samples measured using tensile testing.[2]

The fast initial increase in the in-plane modulus signifies that clay particles provide continuous reinforcement at low volume fractions. Polymer material needs to stretch across the entire plane of the clay platelet in order to effectively transfer load into the next layer. But unlike cellulose nanocrystals or silica nanoparticles, clay platelets have a relatively large lateral dimension. Therefore this process becomes more difficult the thinner the polymer layers. This explanation does not entirely explain why the PU/MTM

modulus increases linearly with the MTM volume fraction in the work done by Kaushik. It should be also noted that for similar MTM volume fractions, the modulus of the composite range from 0.45 to 3.6 GPa in Kaushik's work, as shown in Figure 5.4, these values are much lower than the modulus obtained using BLS. In his work, Kaushik measured the modulus of the same systems using static tensile testing.[2] Brillouin scattering, however, measures visco-elastic behavior of material in an oscillatory fashion at gigahertz frequencies, where relaxation time is negligible as compared to those associated with traditional tensile testing. The modulus measured using BLS is based on adiabatic elastic deformations, whereas the one measured using tensile testing is based on isothermal deformations. Thus, the visco-elastic phenomena of PU and dissipative interaction between PU and clay play larger roles in the latter. The change in PU mobility with the addition of MTM platelets can be observed using Raman scattering. Figure 5.5 shows the Raman spectra of PU and PU/MTM clay LBL film, the peak at 1064 cm^{-1} corresponds to the stretching of C-O-C bonds in the PU backbone.[5] The C-O-C bond is highlighted in Figure 5.6, this is also the region most likely to flex and bend because it is adjacent to a simple ethylene group. Following the addition of clay, this peak is shifted to 1053 cm^{-1}. The downward shift of this peak can be interpreted as an increase in strain in the C-O-C bonds, therefore decreasing chain mobility of PU. While the addition of MTM impedes the mobility of polymer films initially, Forrest et al. showed that for thin films, the glass transition temperature, T_g, decreases with decreasing film thickness.[6] This decrease is due to a combination of the loss of orientational entropy of polymer chains, a change in interfacial interactions, and the increase in chain mobility. The higher the MTM loading the thinner the polymer layers between particles. Below a

certain threshold, the mechanisms that are responsible for the decrease in T_g become effective, and cause the polymer chains to become more flexible, thus reducing the characteristic relaxation time of the structure. While this increase in flexibility did not affect the tensile testing data for the PU/MTM films, because in this measurement the structure is always allowed to fully relax, the BLS measurements may be influenced by the shift in relaxation time. For low MTM concentrations and large film thickness, the relaxation time of the structure may be beyond the time scale probed by BLS, and the measurement yields the adiabatic modulus. As the polymer layers thin, the structural relaxation time begins to overlap with the period to the elastic oscillations probed, and the measured modulus value gradually drops below that corresponding to the adiabatic deformation, the more so, the higher the MTM concentration.

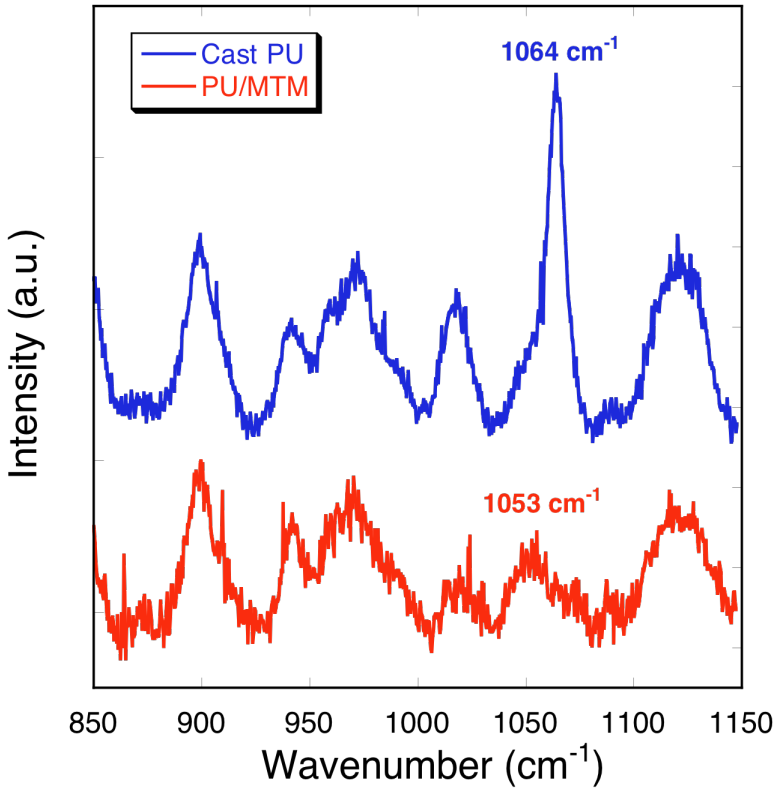

Figure 5.5: Raman spectra of cast PU and PU/MTM films

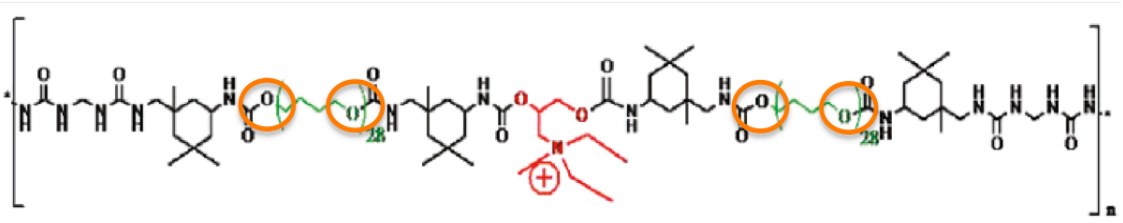

Figure 5.6: Structure of polyurethane backbone, C-O-C bonds are highlighted in orange.[2]

5.2 Modeling of Concentration Dependence on Elastic Modulus

As before, we begin with describing the elastic response of parallel layers of clay and polymer using the rules of mixture of elastic elements. We then refine this model to account for two additional factors: (i) the penetration of polymer into the clay layer, establishing load-transmitting connections between the MTM plates, and (ii) the decrease in relaxation times with decreasing polymer layer thickness, which increases polymer compliance. Kaushik reported that MTM layers deposited during LBL assembly consist of three layers of MTM sheets separated by water bridges.[2] These gaps allow for polymer to deposit in between the sheets of MTM as well as along the sides of the plates. The level of intermixing or polymer penetration depends on the amount of polymer present. Therefore, thicker polymer layers will result in more polymer penetrating into the clay layer. Concerning the increase in polymer mobility and compliance with MTM concentration, as a first approximation we assume a linear relationship between the relaxation time and polymer layer thickness.

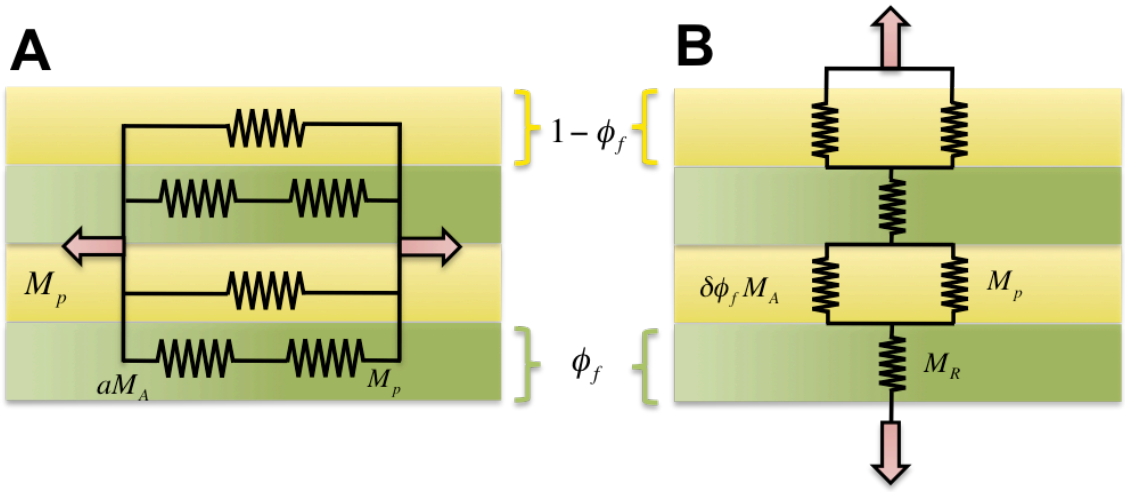

Figure 5.7: A) Springs in parallel for elastic modulus in the growth plane with mixed springs in series; B) springs in series with mixed springs in parallel, the yellow and green are the volume fractions of the polymer and fiber, respectively.

Similar to section 3.4 for polymer/cellN models, we can cast these phenomena into a modified rule of mixture of elastic elements in series and parallel. Figure 5.7 is a schematic of the spring systems for PU/MTM clay films. Equation 3.1 can be written in terms of volume fraction (ϕ_{clay}) and modulus of clay ($M^{//}_{clay}$),

$$c_{11} = \phi_{clay} M^{//}_{clay} + \left(1-\phi_{clay}\right) M^{//}_{p}, \tag{5.1}$$

Polymer insertion in between clay sheets can be addressed by modifying the $M^{//}_{clay}$ term,

$$M^{//}_{clay} = \frac{\phi_{clay}}{aM_R} + \frac{b\left(1-\phi_{clay}\right)}{M^{//}_{p}}, \tag{5.2}$$

where M_R is the modulus of clay along the long dimensions of the platelet (270 GPa), *a* allows for adjustment of the effectiveness of M_R during load transfer, and *b* is a factor which accounts for the fraction of polymer that has infiltrated the clay layer. Equation 5.2 assumes that the polymer that penetrated the clay layer acts in series with the clay platelets where small amounts of load transfer occur between sheets of clay. However,

Equation 5.2 alone does not take into account the relaxation of the PU as the polymer layer thins. A linear relationship between polymer modulus and layer thickness means modulating $M_p^{//}$ with a factor that is proportional to $\left(1-\phi_{clay}\right)$, since the thickness decreases as the MTM concentration increases. Therefore the in-plane elastic moduli for PU/MTM clay can be rewritten as,

$$c_{11}=\left(\frac{\phi_{clay}}{aM_R}+\frac{b\left(1-\phi_{clay}\right)}{M_p^{//}}\right)\phi_{clay}+\left(1-\phi_{clay}\right)^2 M_p^{//}. \tag{5.3}$$

The best-fit values for *a* and *b* of eq.5.3 to the data shown in Fig. 5.4 are listed in Table 5.2. The low value of *a* indicates that the amount of load transfer from clay to polymer is low. Factor *b* is similarly small, this suggests that only a small amount of polymer penetrates in between the clay sheets.

Table 5.2: Modifying Parameters of PU/MTM clay composites

a	b	α	γ	M_R(GPa)[1]	$M_{clay}^{\perp}$ (GPa)[7]
0.05	0. 02	0.93	0.08	270	5

The out-of-plane modulus can be described using elastic elements in series, i.e.,

$$c_{33}=\left(\frac{\phi_{clay}}{M_{clay}^{\perp}}+\frac{\left(1-\phi_{clay}\right)}{M_p}\right)^{-1}, \tag{5.4}$$

where $M_{clay}^{\perp}$ is the modulus of clay along the thickness of the platelets (5 GPa). Similar to our model for fiber fillers, we assume some penetration of clay particles into the polymer layer., which enhances the polymer modulus by an additional amount $\gamma\phi_{clay}M_{clay}^{//}$. Furthermore, as for the in-plane modulus, the polymer layer thickness affects the

polymer modulus due to the reduction of the relaxation time. We therefore consider $M_p^{\perp}\left(1-\phi_{clay}\right)$ as the effective modulus of the polymer. M_p can then be written as

$$M_p = \gamma\phi_{clay}M_{clay}^{//} + M_p^{\perp}\left(1-\phi_{clay}\right). \tag{5.5}$$

Equations 5.4, for the out-of-plane modulus, is then written as,

$$c_{33} = \left(\frac{\phi_{clay}}{\alpha M_{clay}^{\perp}} + \frac{\left(1-\phi_{clay}\right)^2}{\gamma\phi_{clay}M_{clay}^{//} + M_p^{\perp}}\right)^{-1}. \tag{5.6}$$

The α term here is used to express the effect load transfer of $M_{clay}^{\perp}$. What is interesting is that α has a value of 0.93 which suggest that $M_{clay}^{\perp}$ has a near perfect load transfer in the out-of-plane direction. On the other hand, γ only has a value of 0.08 indicating there may be some load transfer as a result clay penetrating into the polymer layer, but this effect is small. These factors suggest the interactions at the interface between clay and polymer is stronger in the out-of-plane direction. Because MTM clay resembles large flat plates, the interaction between polymer and clay at the interface is relatively regular, which allows for strong interaction between the clay particles and the polymer layers. The best fits of Equations 5.3 and 5.5 can be seen in Figure 5.4.

5.3 Summary

In this chapter, the elastic modulus of PU/MTM was measured as a function of the MTM volume fraction. It was found that, while the out-of-plane modulus follows trends similar to that published in literature, the increase of the in-plane modulus slows at high particle loading. Since BLS probes visco-elastic properties at a GHz frequency range, the

the increase in the structural relaxation rates for the polymer layer as a result of thinning may be accountable for this phenomenon. The best-fit of a modified rule of mixture model of out-of-plane modulus shows because of the planar geometry of the clay particles, an effective load transfer of almost 90% was observed.

References

[1] Podsiadlo, P.; Kaushik, A. K.; Arruda, E. M.; Waas, A. M.; Shim, B. S.; Xu, J. D.; Nandivada, H.; Pumplin, B. G.; Lahann, J.; Ramamoorthy, A.; Kotov, N. A. "Ultrastrong and stiff layered polymer nanocomposites," *Science* **2007**, *318*, 80-83.

[2] Kaushik, A. K.; Podsiadlo, P.; Qin, M.; Shaw, C. M.; Waas, A. M.; Kotov, N. A.; Arruda, E. M. "The Role of Nanoparticle Layer Separation in the Finite Deformation Response of Layered Polyurethane-Clay Nanocomposites," *Macromolecules* **2009**, *42*, 6588-6595.

[3] Pozsgay, A.; Frater, T.; Szazdi, L.; Muller, P.; Sajo, I.; Pukanszky, B. "Gallery structure and exfoliation of organophilized montmorillonite: effect on composite properties," *Eur Polym J* **2004**, *40*, 27-36.

[4] Pukanszky, B.; Belina, K.; Rockenbauer, A.; Maurer, F. H. J. "Effect of Nucleation, Filler Anisotropy and Orientation on the Properties of PP Composites," *Composites* **1994**, *25*, 205-214.

[5] Roohpour, N.; Wasikiewicz, J. M.; Paul, D.; Vadgama, P.; Rehman, I. U. "Synthesis and characterisation of enhanced barrier polyurethane for encapsulation of implantable medical devices," *J Mater Sci-mater M* **2009**, *20*, 1803-1814.

[6] Forrest, J. A.; Dalnoki-Veress, K.; Stevens, J. R.; Dutcher, J. R. "Effect of Free Surfaces on the Glass Transition Temperature of Thin Polymer Films," *Physical Review Letters* **1996**, *77*, 2002-2005.

[7] Luo, J. J.; Daniel, I. M. *Characterization and modeling of mechanical behavior of polymer/clay nanocomposites*; Northwestern Univ, Robert R McCormick Sch Engn & Appl Sci, Evanston, IL 60208 USA, 2003.

CHAPTER 6

Effect of Amorphous Interfaces in LBL Films

As mentioned in Chapter 1, as an alternative to the stratified layering of *l*-LBL, *e*-LBL allows one to construct films that have highly diffuse interfaces between layers or the layers are significantly intermixed. Because of the lack of structural interface, the mechanical properties of *e*-LBL films can be expected to be significantly different from those of films with distinctive layers. Picart and Richert first demonstrated the diffusion process underlying *e*-LBL films; in their experiments, confocal laser microscopy was used to image fluorescent tagged electrolyte to show the diffusion of weakly charged polyelectrolyte diffuses.[2,3] Later, Podsiadlo, et al. demonstrated the possibility of incorporating non-organic particles into *e*-LBL films using MTM clay,[1] In this chapter, we take the diffuse interface aspect of *e*-LBL one step further by using fumed silica (SiO_2-*f*) as the filler particle. SiO_2-*f* is a highly ramified nano-aggregate of silica molecules that form a branched network structure by sharing oxygen atoms between silicon atoms. These structures are known to exhibit fractal mass scaling, and have self-similar topologies. As a particle, SiO_2-*f* itself does not have a well-defined surface. The volume fraction of SiO_2-*f* is adjusted by varying the number of layers of SiO_2-*f* relative to that of polymer. The mechanical properties of these films were measured using BLS as a function of humidity.

6.1 Film Characterization

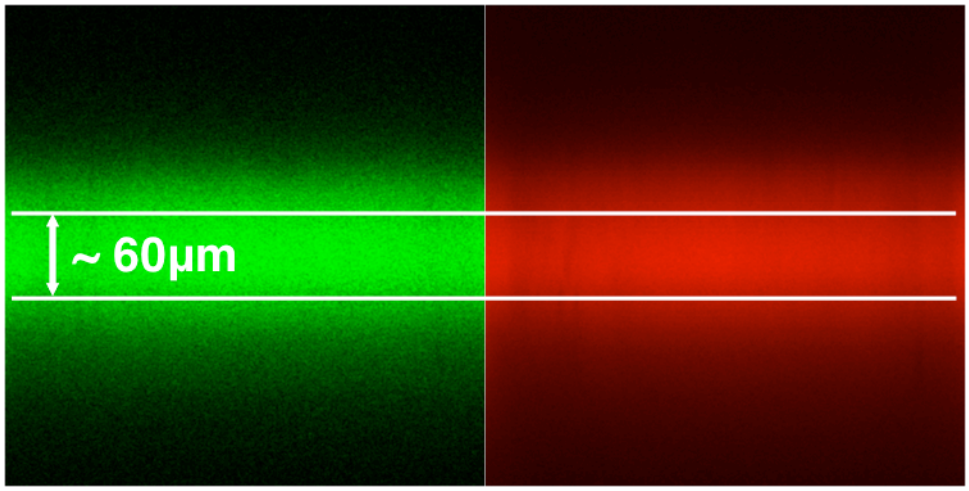

Figure 6.1: Confocal scanning laser microscopy image of $[PEO/PAA]_{30}$ film; here PEO and PAA are tagged with green and red florescent dyes using FITC and Rh B. The arrow indicates the cross-section of the film.

Prior to the addition of fumed silica, the structure of PEO/PAA films was characterized using confocal laser scanning microscopy. Figure 6.1 is an image of a 30 bilayer PEO/PAA film made using *e*-LBL where PEO and PAA are tagged with green and red fluorescing dyes. An even distribution of red and green dyes over the cross-section of the film can be observed. Similar to work by Podsiadlo for poly(ethylenimine)/PAA films,[1] it is therefore evident that PEO/PAA films are blended due to the interdiffusion of PEO and PAA polymers. Similarly, SEM images also supported this finding. The cross-sectional view of $[PEO/PAA]_{30}$ shown in Figure 6.2A shows a smooth and featureless surface. By comparison, the interfaces between the stratified layers of *l*-LBL assembled $[PEI/MTM]_{100}$ are clearly visible in cross-sectional SEM (Figure 6.2A insert). It should be also noted that the thickness of PEO/PAA (~60 µm) is much greater than that PEI/MTM (~4 µm) for a much smaller number of bilayers.

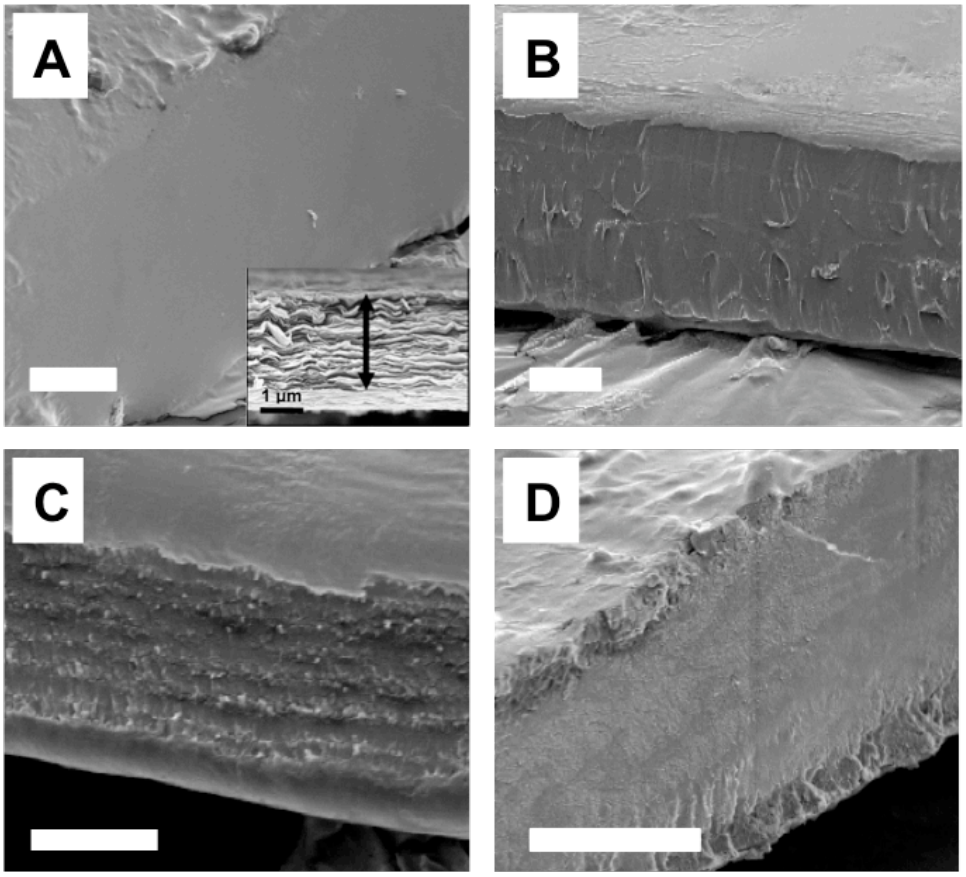

Figure 6.2: SEM images of A) $[PEO/PAA]_{30}$ (insert: *l*-LBL assembled $[PEI/MTM]_{100}$)[1], B) $[(PEO/PAA)_{10}/SiO_2\text{-}f]_3$, C) $[(PEO/PAA)_3/SiO_2\text{-}f]_{10}$ and D) $[PEO/PAA/SiO_2\text{-}f]_{30}$; the scale bars indicate 10 µm for A and B, and 20 µm for C and D.

Layers of SiO_2-*f* were introduced into PEO/PAA films at various volume fractions in order to change the interfacial quality of the films gradually — the out-of-plane modulus measure by BLS reflects the average adhesion between layers across the entire film. The detailed deposition process is described in Chapter 2. The incorporated layers of SiO_2-*f* can be seen in Figures 6.2B-D; cross-sections of $[(PEO/PAA)_{10}/SiO_2\text{-}f]_3$, $[(PEO/PAA)_3/SiO_2\text{-}f]_{10}$ and $[PEO/PAA/SiO_2\text{-}f]_{30}$ were imaged using the SEM, where 3, 10, and 30 is the number of SiO_2-*f* layers, respectively. The SiO_2-*f* layers shown in Figures 6.2B and C visibly run the length of the film as white diffuse lines. However, for higher SiO_2-*f* loading (Figure 6.2D), the SiO_2-*f* layers become less defined. Instead of

fine lines, broad irregular bands of light-gray features are visible. For Figures 6.2B and C, the thickness and spacing of the SiO_2-*f* lines depends on the number of SiO_2-*f* layers deposited.

As described in Chapter 1, the *e*-LBL assembly involves the diffusion of weakly bonded polymers in and out of the swollen film during deposition. While it is apparent that the PEO and PAA diffuse into each other from Figure 6.1, the SEM images indicate that SiO_2-*f* does not diffuse into the adjacent layers. They form relatively thin layers in between polymer layers. Therefore, these films are not entirely homogenous. However, at high particle loading, where a layer of SiO_2-*f* is deposited after every PEO/PAA layer, the interfaces become more "muddled" as a result of the mutual diffusion of PEO and PAA into one another. Although the total number of PEO/PAA layers is kept constant at 30 bilayers for all combinations of film layering, the overall thickness of the films decreases from 60 to 20 μm as more SiO_2-*f* layers are incorporated. This suggest that, while PEO and PAA easily diffuse into each other during immersion into the respective solutions, SiO_2-*f* acts as a diffusion barrier because it does not swell. The thicknesses of the individual PEO/PAA layers are indeed visibly thinner between SiO_2-*f* layers for higher SiO_2-*f* loading.

The amount of SiO_2-*f* incorporated was determined using TGA, as shown in Figure 6.3. The volume fraction of SiO_2-*f* is calculated from the weight fraction of SiO_2-*f* at the end of the TGA cycle using Equation 2.5, where the densities of SiO_2-*f* and PEO/PAA are 0.60 and 1.24 g/cm^3, respectively. The volume fraction of SiO_2-*f* increases fairly linearly with the number of SiO_2-*f* layers.

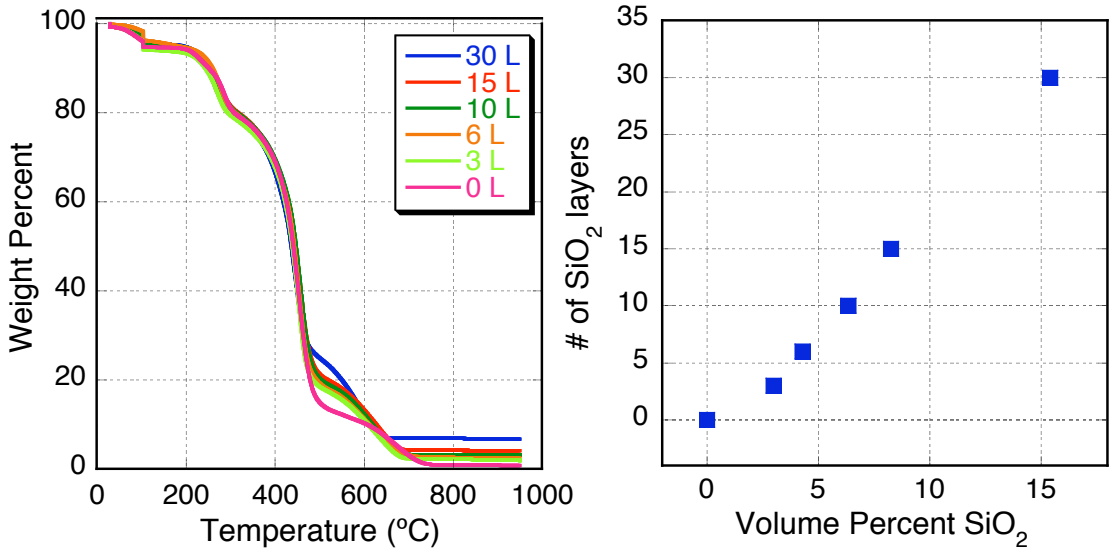

Figure 6.3: TGA measurements of PEO/PAA/SiO_2-*f* films, where the legend indicates the number of SiO_2-*f* layers (left); number of SiO_2-*f* layers as a function of SiO_2-*f* volume percent (right).

6.2 Effect of Humidity

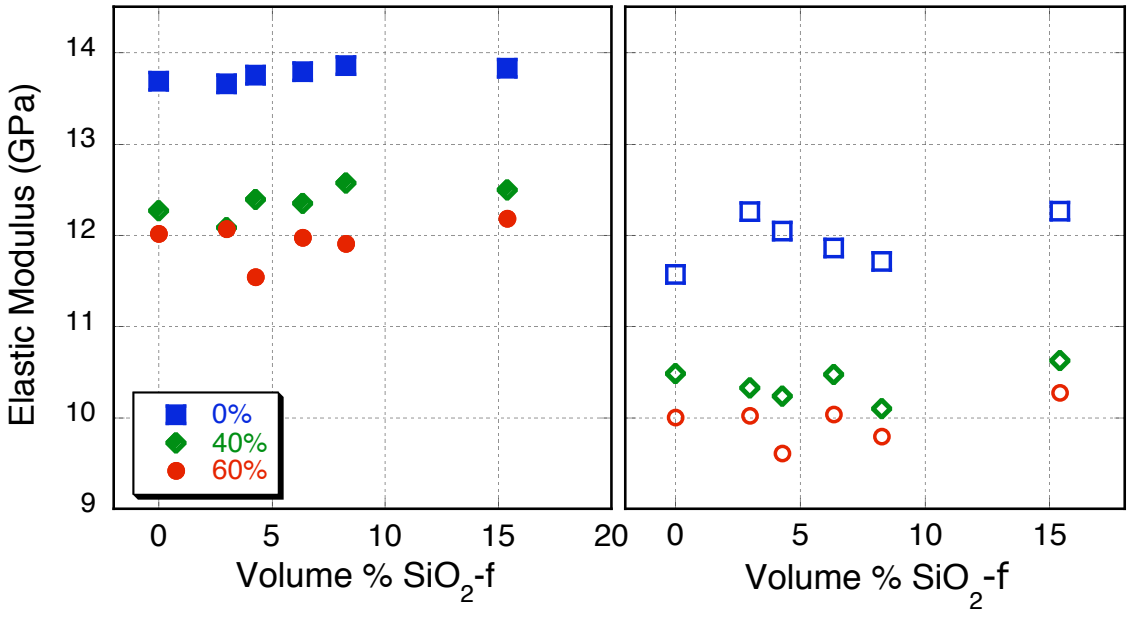

Figure 6.4: In and out-of-plane modulus of PEO/PAA/SiO_2-*f* as a function of volume fraction for films at 0, 40, and 60% humidity; closed = out-of-plane, open = in-plane modulus.

Figure 6.4 shows the stiffness of PEO/PAA/SiO_2-*f* films as function of SiO_2-*f* volume fraction. In the PEO/PAA/SiO_2-*f* films, the slight anisotropy is likely to result from PEO and PAA alignment during the interdiffusion process. However, there is little effect from the incorporation of SiO_2-*f* on the elastic modulus, at all three humidity levels, which suggest that SiO_2-*f* does not offer any additional structural support, nor does it deteriorate the mechanical properties of the polymer. More prominent is the effect humidity on the elastic response of these *e*-LBL assembled films. For films fabricated using *l*-LBL assembly where highly charged polymers and particles are bonded via strong electrostatic forces, the mechanical properties are generally unaffected by humidity. By contrast, PEO/PAA films are fabricated using weakly charged polyelectrolytes where an immense amount of diffusive intermixing takes place during deposition. This process causes orientation of polymer chains and leaves behind voids for the infiltration by and removal of small molecular species during operation. The intercalation of these molecules into the LBL films causes a change in bonding interactions and, consequently, the mechanical properties. Therefore *e*-LBL films show dramatic changes in stiffness and film quantity at different room humidity levels. For dry films at 0% humidity and the same films when the room was at 40 and 60% humidity, the elastic moduli show a more dramatically decrease at 40% humidity, but further increase in humidity provides little change in the moduli. Physically, the films can go from a soft plastic to a sticky gelatin like consistency.

6.3 Effect of Diffused Interface on Elastic Modulus

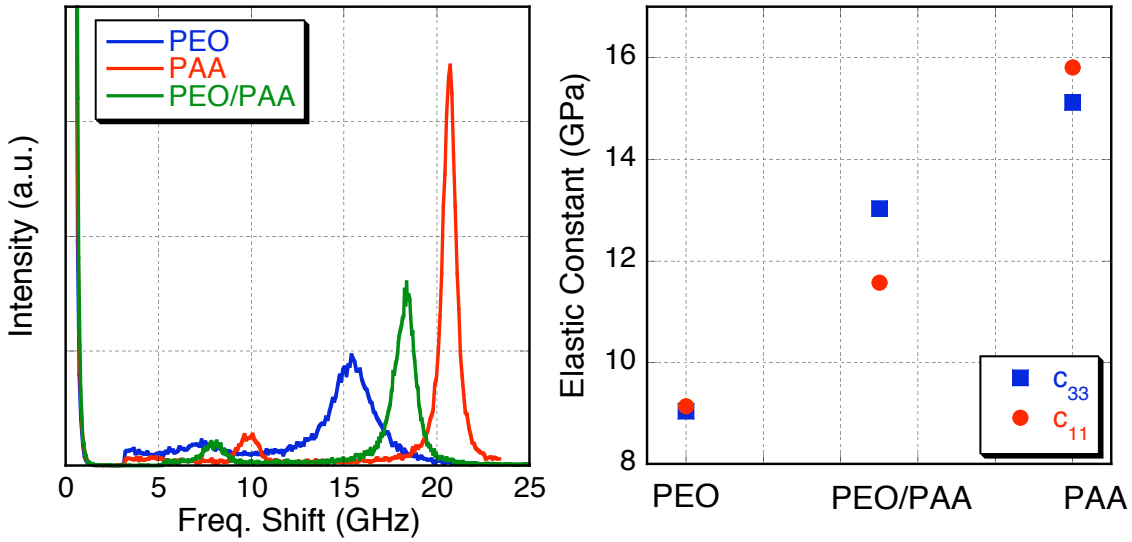

Figure 6.5: An example of anti-Stokes peaks of PEO, PAA, and $[PEO/PAA]_{30}$ (left) and their corresponding c_{11} and c_{33} at 0% humidity (right).

Unlike strong electrostatic interactions between oppositely charged electrolytes in *l*-LBL assembly, the ability for polymers to assemble at such a rapid rate as for *e*-LBL films depends on the diffusion of weakly bonded polymer across the continuum of the film. For this to happen, the interactions between constituents must be weak, such as hydrogen bonding.[4,5] The weak bonding and swelling of adsorbed polymers when in contact with water, as well as the lack of interfaces within the film presents interesting possibilities for their mechanical properties. An example of the anti-Stokes peak from BLS and their corresponding moduli can be seen in Figure 6.5 for *e*-LBL assembled PEO/PAA film along with the cast films of PEO and PAA. It is interesting that the stiffness of PEO/PAA films fall in between the stiffness of PEO and PAA. This suggests that there are about equal amounts of PEO and PAA deposited. The out-of-plane modulus is also slightly higher than that of the in-plane modulus, which indicates that

some degree of elastic anisotropy results from the swelling and interdiffusion process. Since linear chain-like polymer carries load predominantly through its backbone, the fact that the modulus is in the predominant diffusion direction suggest that polymer chains have oriented to some degree during the deposition process.

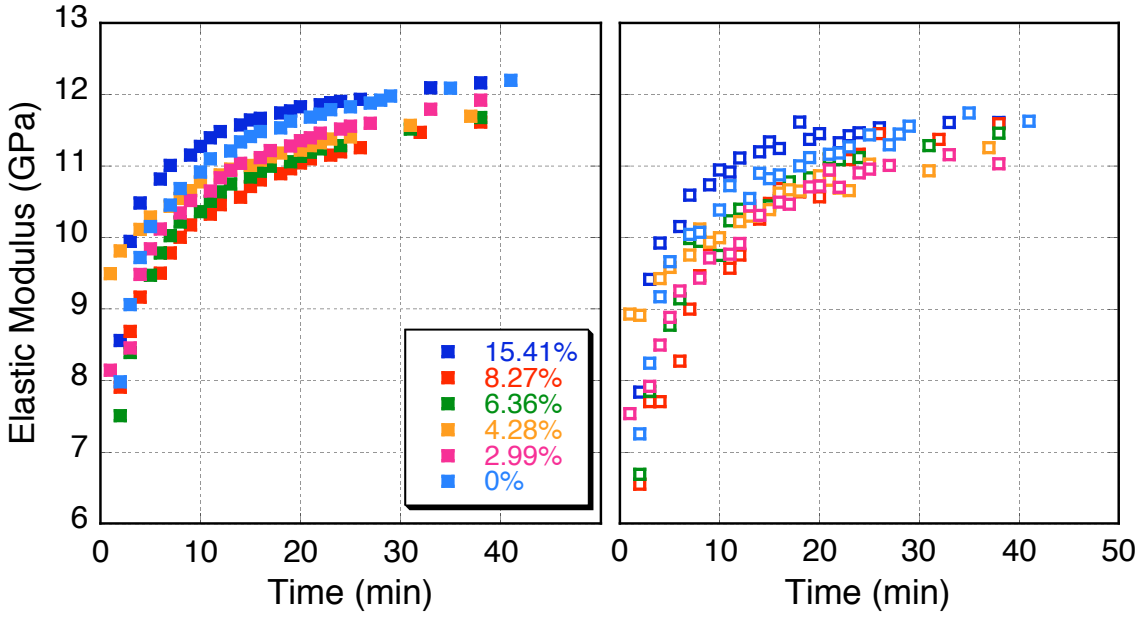

Figure 6.6: Elastic modulus as a function of dehumidifying time for $[(PEO/PAA)_x/SiO_2]_y$ films where films were allowed to dehumidify from 100% to 60% room humidity; the percentages indicate the volume percent of SiO_2-,; closed = out-of-plane, open = in-plane modulus.

For Figure 6.5, the BLS measurements of PEO/PAA were taken at 0% humidity; however, when compared to the same films measured at higher humidity levels, the stiffness of the material is lower. In order to study the effect of humidity on *e*-LBL films, films were kept in a 100% humidity chamber and were allowed to dehumidify to ambient humidity (60%). Figure 6.6 depicts this dehydration process of PEO/PAA/SiO_2-*f* films as a function of time, where the frequency shift was measured using BLS at ~1 min intervals. The difference between the elastic moduli of samples containing different SiO_2-*f* concentrations is small. The elastic modulus data also follow similar curves as the

film is drying out. The c_{33} slightly higher than that of the c_{11} like to that of the PEO/PAA film at 0% humidity. The reason for this, as stated before, may be the partial orientation of polymer chains perpendicular to the film plane as a result of the interdiffusion of the weakly charged polyelectrolyte while the substrate undergoes swelling behavior. Once deposited and dried, the oriented polymer chains provide low-migration energy passageways for small molecules, such as water, and the films can therefore absorb moisture at high levels. Water molecules that diffuse into the pores of these films further weaken the interactions between the polymer. Consequently, the mechanical modulus of the material decreases. As shown in Figure 6.6, the phenomenon is reversible. Here, a highly humidified film is placed in a relatively dry room, and the material dehydrates rapidly. This process can be monitored by means of measuring the elastic modulus, which gradually increases as the dispersive interactions between polymer chains are restored upon removal of the water. This effect is remarkably strong. By changing the relative humidity from 100% to 60%, the elastic modulus increases by ~50% above its starting value.

6.4 Summary

PEO/PAA and PEO/PAA/SiO_2-*f* films were made through *e*-LBL assembly process. The interface of these films were characterized using CLSM and SEM, it was shown that the PEO/PAA film have indistinctive or amorphous cross-sections where both constituents diffused through the entire film. In the case of PEO/PAA/SiO_2-*f* films, SiO_2-*f* formed thin, incremental layers within the PEO/PAA film; the number of and thickness between the SiO_2-*f* layers depend on the number of SiO_2-*f* layers deposited. It is also

visible that SiO_2-*f* does not diffuse. Conversely, the accumulation of SiO_2-*f* between layers does also hinder the diffusion of PEO/PAA across the interfaces; individual layers grow to be less thickness. The incorporation of SiO_2-*f* neither enhances nor deteriorates the elastic properties of the films. The effect of diffuse interface on the mechanical properties of *e*-LBL assembled films was studied for PEO/PAA and PEO/PAA/SiO_2-*f* films where the SiO_2-*f* content ranged from 0 to ~15 vo.%. Dehydration measurements of highly humidified *e*-LBL films showed that their elastic moduli are highly dependent on the amount of moisture present in the films while no distinguishable effects can be observed for the different volume fractions of SiO_2-*f*. The out-of-plane moduli are also slightly higher than that of the in-plane moduli as a result of polymer alignment during deposition.

References

[1] Podsiadlo, P.; Michel, M.; Lee, J.; Verploegen, E.; Kam, N. W. S.; Ball, V.; Lee, J.; Qi, Y.; Hart, A. J.; Hammond, P. T.; Kotov, N. A. "Exponential growth of LBL films with incorporated inorganic sheets," *Nano Lett* **2008**, *8*, 1762-1770.

[2] Picart, C.; Mutterer, J.; Richert, L.; Luo, Y.; Prestwich, G. D.; Schaaf, P.; Voegel, J. C.; Lavalle, P. "Molecular basis for the explanation of the exponential growth of polyelectrolyte multilayers," *P Natl Acad Sci Usa* **2002**, *99*, 12531-12535.

[3] Richert, L.; Lavalle, P.; Payan, E.; Shu, X. Z.; Prestwich, G. D.; Stoltz, J. F.; Schaaf, P.; Voegel, J. C.; Picart, C. "Layer by layer buildup of polysaccharide films: Physical chemistry and cellular adhesion aspects," *Langmuir* **2004**, *20*, 448-458.

[4] DeLongchamp, D. M.; Hammond, P. T. "Highly ion conductive poly(ethylene oxide)-based solid polymer electrolytes from hydrogen bonding layer-by-layer assembly," *Langmuir* **2004**, *20*, 5403-5411.

[5] Sukhishvili, S. A. "Responsive polymer films and capsules via layer-by-layer assembly," *Curr Opin Colloid In* **2005**, *10*, 37-44.

CHAPTER 7

Comparison of the Effect of Particle Geometries and Interfaces on Linear Grown LBL Films

The previous chapters dealt with the effect of incorporating particles into LBL films individually, in this chapter, we compare the effects of filler concentration and geometry on the in and out-of-plane stiffness of the films. Specifically, we varied the amount and kind of polymer deposited between the filler material, and the shape of the filler material (rod-like, spherical, platelet, and amorphous interface). Comparison of how these factors influence the mechanical properties of LBL composites provides additional insights into the nature of these materials, which may useful in guiding the processing strategies. We demonstrate that the stiffness vs. volume fraction deviates greatly from that of the traditional springs in parallel and in series interpretation of composite stiffness. We also show this deviation is depends not only on geometry of the particles, but heavily on the type of polyelectrolyte used as well.

7.1 Film Characterization

To demonstrate the structure of LBL films, the surface and interfaces of the LBL films are imaged. A schematic of the layering process are shown in Figure 7.1A – C; three bilayers can be seen for polymer/cellN, PU/SiO_2-NP and PU/MTM films. The orange mesh indicates PU layers, the blue and light blue mesh is used to indicate alternating layers of either PDDA or chitosan with PSS. One bilayer of PDDA/cellN, PDDA/SiO_2-22nm and PU/clay was deposited on Si wafer for imaging using the AFM, shown in Figure 7.1D – F. The film growth process was monitored using ellipsometry. The thickness of films grown on a Si wafer was measured after the deposition of every layer. The growth behaviors of the films are fairly linear, as shown in Figure 7.2; the growth rate is proportional to the solution concentration of the deposited polymer layer and the lateral dimensions of the particles. The thickness of the bilayers ranged between 3 to 23 nm.

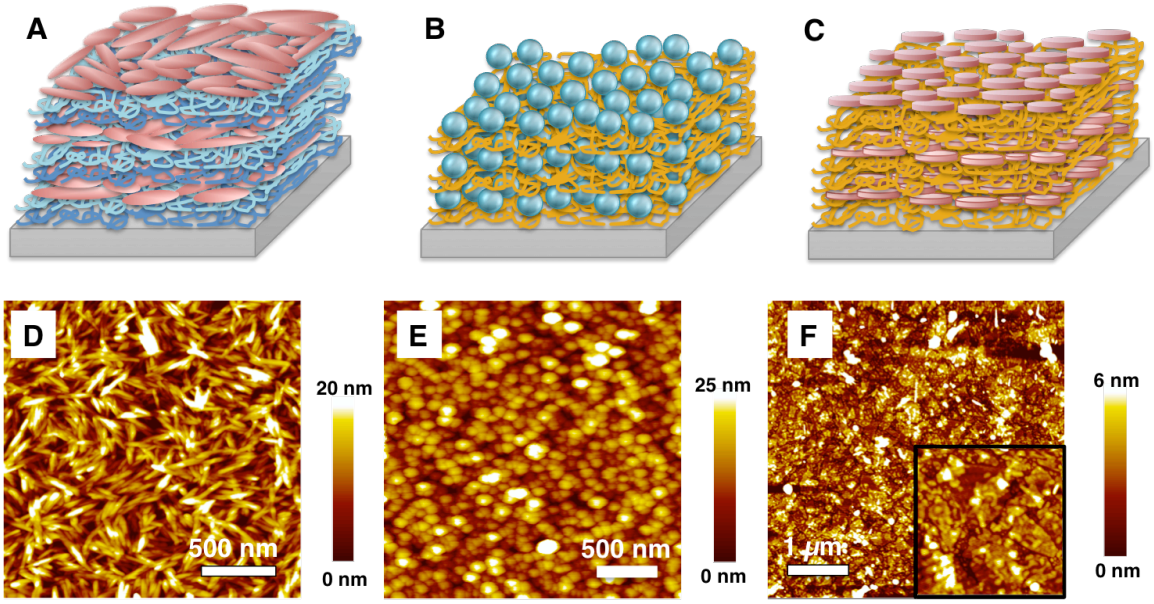

Figure 7.1: A – C) Schematic of film assembly for the different geometries; D – F) AFM images of 1 bilayer deposition of celln, SiO_2-NP and clay.

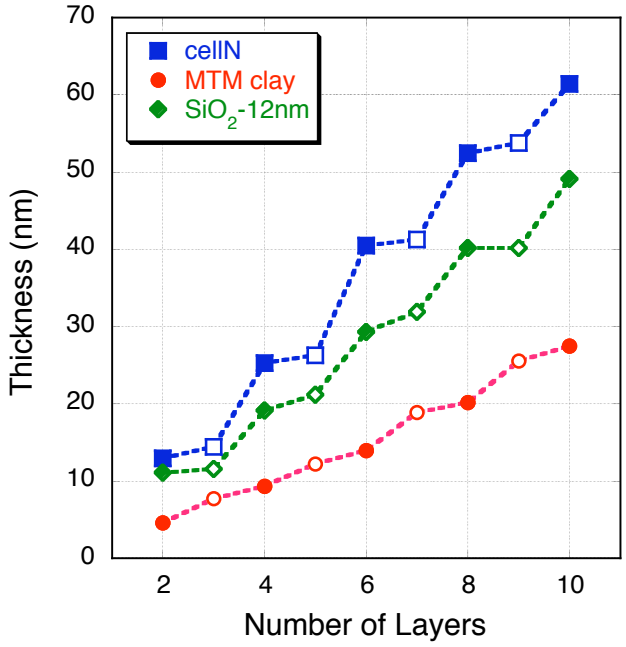

Figure 7.2: Thickness of PDDA/cellN, PU/MTM and PU/SiO_2-12nm films as a function of number of layers, using 1 and 0.38% solution concentrations of PDDA and PU; open = polymer growth, closed = particle growth.

7.2 Effect of Layering on Mechanical Properties of LBL Films

Unlike most traditional composites, the amount of filler material incorporated into a LBL film is not a predetermined quantity. Instead, the volume fraction of filler can be varied through changing the thickness of the polymer layer, this can be done using polymer solutions of different concentrations or pairings of two or more oppositely charged polyelectrolytes to create a polymer stratus in between filler layers. In other words, the thickness of the filler layer remains relatively fixed while the thickness of the polymer layer changes and thus varying the filler concentration per unit volume. This method of varying the filler concentration presents two congruent issues: in order to increase the filler volume fraction one would need to reduce the polymer layer thickness, however, the reduction of polymer thickness would decrease its adherence to the particle layer. In turn, the stiffness as a function of volume fraction behavior for nanocomposites comprised of this configuration is strongly dependent on the adhesive forces between

these different types of materials, particularly in the case of the transverse or out-of-plane modulus. Finally, changes in filler geometry may have a pronounced effect on the mechanical properties of the film because of the layering effect. To gain a better understanding of these issues we employed Brillouin light scattering to study the in-plane and out-of-plane elastic moduli of LBL films as a function of filler geometry and concentration. An example of the Brillouin spectra can be seen in Figure 7.3, the curves are smoothed for PDDA/cellN, PU/MTM and PU/SiO_2-12nm for easier identification of the peaks.

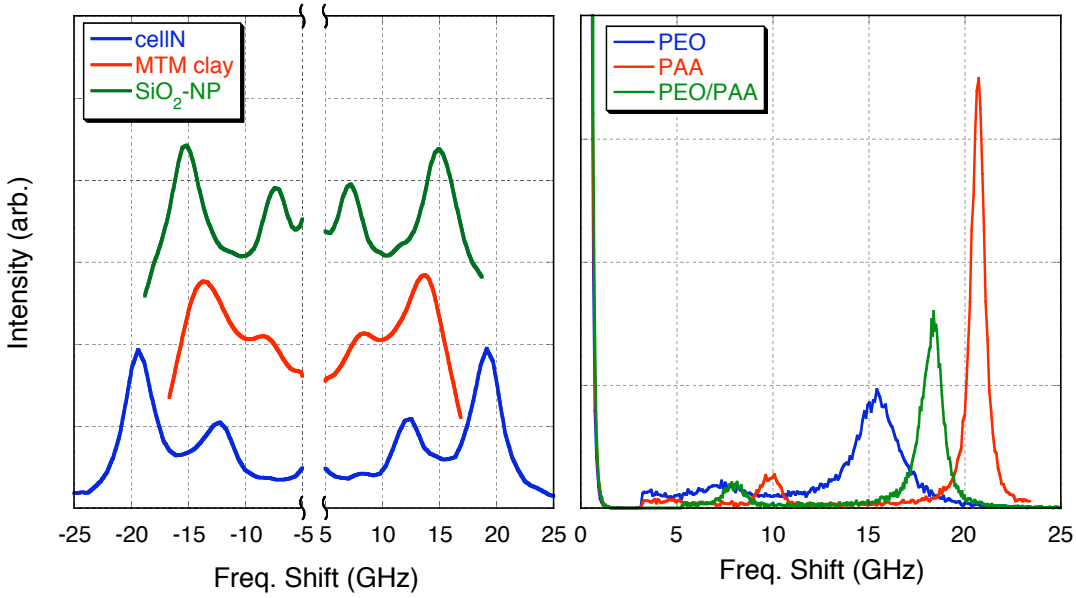

Figure 7.3: Exemplary Brillouin spectra for PDDA/cellN, PU/MTM and PU/SiO_2-12nm film (right) and PEO, PAA and PEO/PAA films (left). Spectra were taken in the backscattering geometry for samples made on silicon wafers. Peaks correspond to frequency shifts from 2α (inner) and 180° (outer) longitudinal acoustic phonons.

Figures 7.4 – 7.6 show the elastic modulus of LBL films (c_{11} or c_{33}), normalized with respect to that of the matrix (c_m), as a function of filler volume fraction. The incorporation of higher stiffness particles yields an increase of the polymer stiffness for all LBL films, the plots of modulus vs. filler volume fraction reveal that there are strong

variations in the effectiveness of such reinforcement depending on the particle type, its geometry, and the nature of the binding polymer.

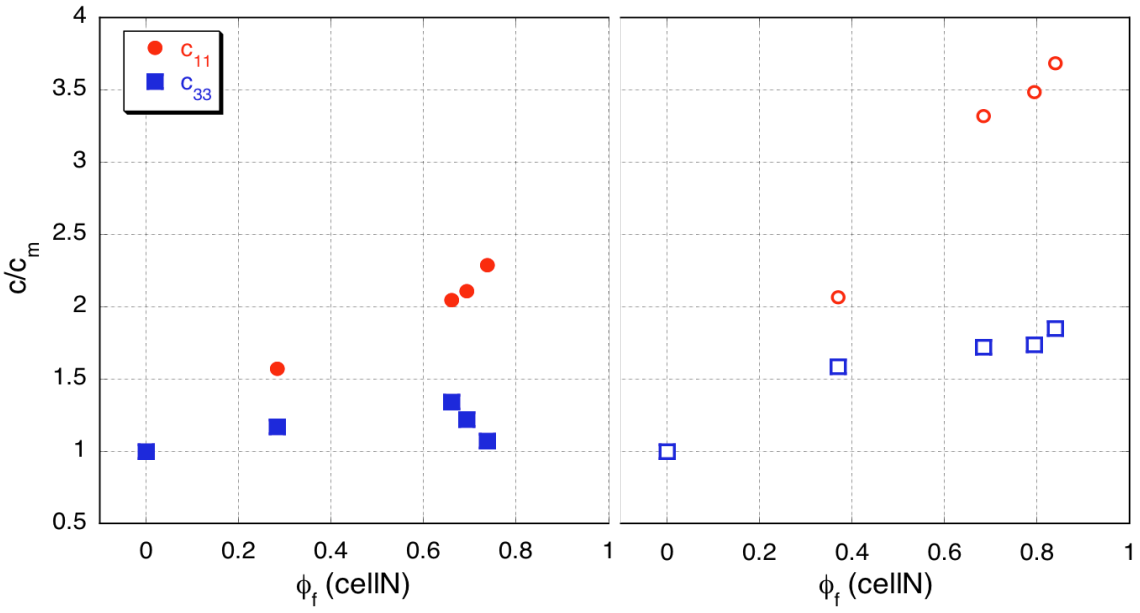

Figure 7.4: Relative elastic modulus of chit/cellN (left) and PDDA/cellN (right) LBL films as a function of cellN volume fraction.

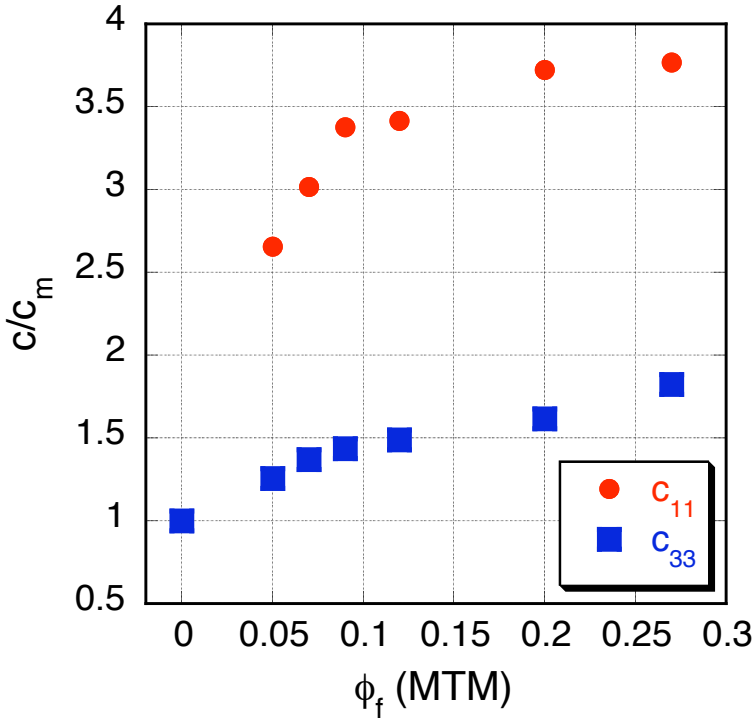

Figure 7.5: Relative elastic modulus PU/MTM clay LBL films as a function of MTM clay volume fraction.

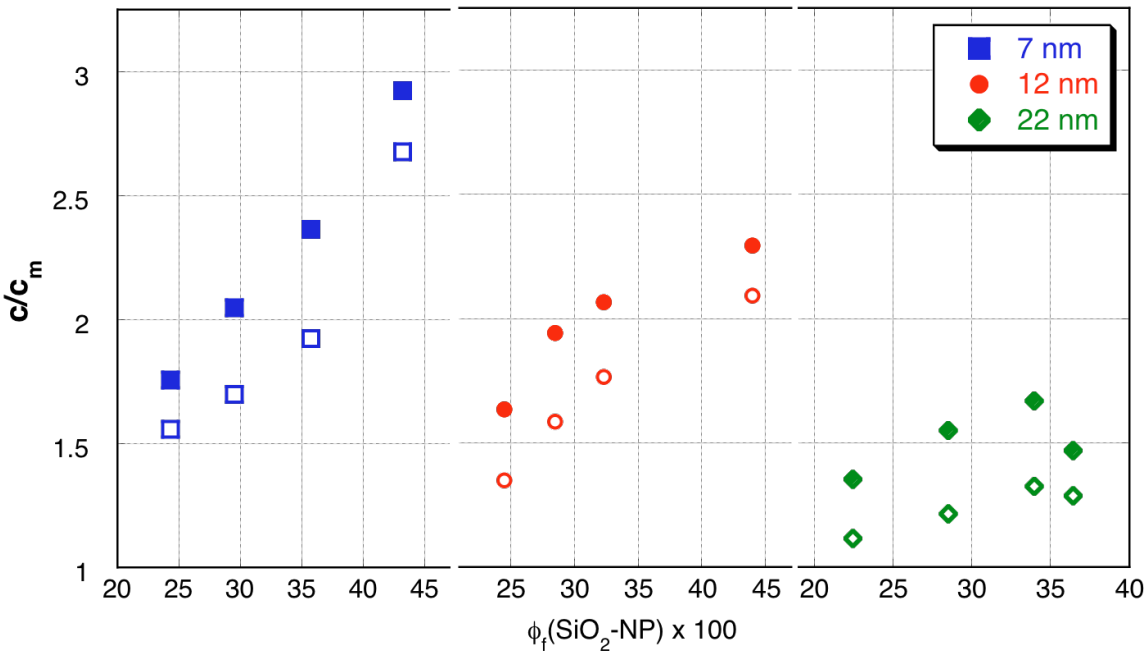

Figure 7.6: Relative elastic modulus of PU/SiO_2-NP as a function of SiO_2-NP volume percent; open = in-plane modulus (c_{11}), closed = out-of-plane modulus (c_{33}).

7.3 Effect of Change in Polyelectrolyte

Figure 7.4 is a plot of elastic moduli of chit/cellN and PDDA/cellN films as a function of cellN volume fraction. The in-plane moduli for both sets of films yield a linear response with the addition of cellN layers. The reinforcing effect of cellN fibers is significantly stronger in the case of PDDA films. This linear response is fairly consistent with traditional models for the in-plane modulus for short-fiber composites,[1-5] however the out-of-plane modulus deviates from such a behavior, especially for the chit/cellN films. While the out-of-plane modulus for PDDA/cellN films increases with increasing cellN volume fraction and eventually plateaus, this modulus for chit/cellN films actually begins to decrease at high cellN loading. The two sets of samples differ only in the polymeric material used with all other deposition parameters kept constant. Accordingly,

the stiffness plots reveal differences in the adhesion between polymer and fibers. A fundamental characteristic of linearly grown LBL film is that, with the exception of chemical bonding using a cross-linker, the layers are held together by relatively weak Van der Waal forces. Load transfer occurs at contact points between the particles and polymer. The number and strength of these contact points is directly correlated to the electrostatic charge densities of the polyanions and polycations. This is evident from Figure 7.4, where for the same number of cellN bilayers, PDDA films yield not only a higher modulus but also a higher particle loading of cellN. This may be because PDDA has a higher ionic strength than chitosan, PDDA readily dissolves in water whereas chitosan will only dissolve with the aid of acetic acid. The higher particle loading (as a function of number of cellN bilayers) for PDDA films is due to the electrostatic attraction of the particles during immersion in the solution and the higher modulus of PDDA/cellN reflects the stronger interactions between PDDA and cellN in the final product. This is even better illustrated at high particle loading for chit/cellN films. The out-of-plane modulus drops off dramatically in case chitosan is used as adhesive, while it stays relatively constant for PDDA. This indicates that the electrostatic charge of chitosan is weak and thus limiting the interaction between chitosan and cellN.

7.4 Effect of Geometry and Particle Size

The geometry of the incorporated particles can also have pronounced influence on the stiffness of the LBL films. In Figure 7.4, the two sets of films differ in the polymer used for film build up. Figures 7.5 and 7.6 show normalized modulus data for films made by using the same polymer and similar polymer dilutions, but filler particles that

differ in their geometries. AFM (Figure 7.1D) and scanning electron microscopy[6] images show that cellulose nanocrystals have a rod-like structure with lengths ranging between 200 – 400 nm and a diameter of 5 nm. Our AFM images (Figure 7.1E), as well as previous studies using wide-angle X-ray diffraction,[ref.] reveal that MTM clay has a disk-like structure with dimensions of 100 – 1000 nm in diameter and 1 nm in thickness. The single layer of MTM clay deposited for imaging consists of three layers of silicate separated by 0.28 nm water bridges.[7] Finally, AFM (Figure 7.1F), transmission electron microscopy, and a Zetasizer characterization demonstrates that SiO_2-NP have a sphere-like structure with diameters of 6.20, 13.38, and 24.17 nm. However, as before, they will be referred to by their nominal diameters provided by the manufacturer. AFM images also reveal close, densely packed layers of cellN, MTM clay and SiO_2-NP after deposition of one bilayer.

For PU/MTM and PU/SiO_2-NP films, different dilutions of PU solution were used to vary the polymer layer thickness. Figure 7.5 is a plot of the elastic modulus as a function of volume fraction of MTM clay for PU/MTM clay films, normalized with respect to that of pure polymer. Here the stiffness curves show trends similar to those for PDDA/cellN films, in particular concerning the out-of-plane modulus. Like PDDA/cellN films, the out-of-plane modulus increases monotonously with the addition of MTM with no obvious decrease at high particle loading. The main difference is found in the in-plane modulus, instead of exhibiting the traditional linear curve as a function of volume fraction, the function resembles that the out-of-plane curve, but with a more pronounced reinforcement effect from the MTM clay. There are two ways to interpret the deviation of the modulus vs. MTM volume fraction from linearity: one is that the modulus tails off

prematurely and the full potential of reinforcement is not achieved; the other way is that initially, for small loading fractions, there is a higher than linear reinforcement effect, which eventually adjusts to a trend more in line with the rules of mixing. Which of these applies here is difficult to say, but we can offer the following analysis. First, let us point out that the linear regime for the composites loaded with cellN extrapolates to about 25% of the axial modulus of the fiber itself at 100% fiber loading. By comparison, the elastic modulus of MTM is of the order of 250 GPa, which on the normalized scale of Figure 7.5 would correspond to an ordinate value of ~50. Obviously, the in-plane modulus tapers off long before that and levels at a value that is about an order of magnitude smaller. We therefore believe that the first explanation applies here. This illustrates that as a result of the large diameter of the clay particles, comparably thicker polymer layers are required to hold the film together in order for proper load transfer.

Finally, PU/SiO_2-NP LBL films, Figure 7.6, display yet another trend for relative stiffness as a function of SiO_2-NP volume fraction. Unlike for the previous films, where the in-plane and out-of-plane moduli differ greatly, they differ comparably little with the addition of SiO_2-NP. In addition, the in-plane modulus is smaller than the out-of-plane modulus, unlike for the other two particle geometries. For cellN fibers and clay platelets, the tremendous overlap between particles allows not only for particle-polymer load transfer but for particle-particle load transfer as well. However, spherical nanoparticles exist as discrete entities where little to no interactions occur between individual particles. Therefore, mechanistically speaking, the stiffness of these LBL films is fairly isotropic. Another immediate observation is the effectiveness of the incorporation of SIO_2-NP decreases with the increase in particle size. While data reported on the in-plane modulus

is congruent among previous works,[2,8-10] thus far, there has been little to no information available on the out-of-plane modulus of these films.

7.5 Summary

BLS reveals new and surprising information about the mechanical and interfacial properties of nanostructured composites. Based on these results, we have demonstrated that the variation of polymer used and particle geometry had striking effects on the stiffness as a function of particle volume fraction. Factors such as using polyelectrolyte with different ionic strength yields different effect on the in- and out-of-plane moduli. This directly affects the interfacial adhesion between the polymer and particles. However, the interfacial adhesion is not limited to the charge attraction between the particle and the polymer. The particle surface coverage by polymer layer and particle aspect ratio also contributes to the interfacial adhesion as observed in the case for PU/MTM clay. Finally, for particles with small aspect ratio, porosity produced during the self-assembly process becomes dominant.

References

[1] Cox, H. L. "The Elasticity and Strength of Paper and Other Fibrous Materials," *Brit J Appl Phys* **1952**, *3*, 72-79.

[2] Jiang, Y. P.; Tohgo, K.; Yang, H. "Study of the effect of particle size on the effective modulus of polymeric composites on the basis of the molecular chain network microstructure," *Computational Materials Science.*

[3] Krenchel. *Fibre Reinforcement*; Akademisk Forlag: Copenhagen, 1964.

[4] Matthews, F. L.; Rawlings, R. D. *Composite Materials: Engineering and Science*; Woodhead Publishing Limited: Abington Hall, 1999.

[5] Sudduth, R. D. "Influence of nanoscale fibres and discs on intrinsic modulus and packing fraction of polymeric particulate composites and suspensions," *Mater Sci Tech-lond* **2003**, *19*, 1181-1190.

[6] Podsiadlo, P.; Choi, S. Y.; Shim, B.; Lee, J.; Cuddihy, M.; Kotov, N. A. "Molecularly engineered nanocomposites: Layer-by-layer assembly of cellulose nanocrystals," *Biomacromolecules* **2005**, *6*, 2914-2918.

[7] Kaushik, A. K.; Podsiadlo, P.; Qin, M.; Shaw, C. M.; Waas, A. M.; Kotov, N. A.; Arruda, E. M. "The Role of Nanoparticle Layer Separation in the Finite Deformation Response of Layered Polyurethane-Clay Nanocomposites," *Macromolecules* **2009**, *42*, 6588-6595.

[8] Cho, J.; Sun, C. T. "A molecular dynamics simulation study of inclusion size effect on polymeric nanocomposites," *Comp Mater Sci* **2007**, *41*, 54-62.

[9] Ji, X. L.; Jing, J. K.; Jiang, W.; Jiang, B. Z. "Tensile modulus of polymer nanocomposites," *Polym Eng Sci* **2002**, *42*, 983-993.

[10] Vollenberg, P. H. T.; Dehaan, J. W.; Vandeven, L. J. M.; Heikens, D. "Particle-Size Dependence of The Young Modulus of Filled Polymers: 2. Annealing And Solid-State Nuclear Magnetic-Resonance Experiments," *Polymer* **1989**, *30*, 1663-1668.

CHAPTER 8

Conclusions and Future Work

The creation of stronger and more mechanically stable films ultimately depends on the materials used for composite fabrication and the manner in which they are assembled. Layer-by-layer assembly offers a prolific fabrication technique where the film structure can be controlled down to the nanometer scale. The studies conducted in this thesis allowed us to investigate the elastic modulus of LBL films as we vary their structural features. We have presented a unique and innovative way to study the mechanical properties of LBL films using Brillouin light scattering. It not only allows us to obtain the in-plane modulus, but the less commonly known out-of-plane modulus as well. The effectiveness of load transfer between particle and polymer matrix was examined using four different types of particle geometries. Different moduli trends were established for these particles as a function of their volume fraction.

For LBL films fabricated using rod-like cellN fibers produced films the highest overall moduli were achieved, producing two- and three-fold increases in moduli for chit/cellN and PDDA/cellN, respectively. For both systems, the elastic modulus is independent of the film thickness and unaffected by heat treatment. Both types of cellN films showed a linear increase for in-plane modulus as a function of particle volume fraction. We also observed an unprecedented decrease in the out-of-plane modulus at

high particle loading for chit/cellN. These results indicate stronger interfacial bonding in the case of PDDA/cellN LBL films, the better adhesion between the polymer and particle allowed for more effective load transfer. The importance of adhesion is also manifest for nano-composites with disc-like fillers. A sub-linear increase of the in-plane modulus as a function of filler concentration is observed for PU/MTM clay composite, suggesting that despite the large diameter of MTM clay, load transfer between plates becomes inefficient as the polymer layers thin.

The in-plane modulus for polymer/SiO_2-NP shows a similar response to polymer/cellN films, particularly for small particles size, the enhancement from SiO_2-NP rapidly degrades as the particle size increases. The out-of-plane modulus follows the same general trend as a function of particle loading as the in-plane modulus, and interestingly, it is also higher than the in-plane modulus in all cases, with the exception of mixed particle size films. This is due to the fact that the spatial distribution of porosity in the structure prevents load transfer in-plane more so than out-of-plane. This is a consequence of the directionality of the deposition process.

Finally, the effect of interface definition on the elastic properties of LBL films was studied using *e*-LBL, where film assembly is governed by the interdiffusion of weakly charged polymers. Fumed silica was also incorporated into these films at variable volume fractions. Unlike for SiO_2-NP, the amount of SiO_2-*f* in the films has little effect on the elastic properties of the material. Instead, dehydration of fully humidified *e*-LBL films shows that the elastic modulus changes substantially with humidity. The reason for this phenomenon is that the weakly bonded polymers have become oriented perpendicular to the substrate during the interdiffusion, creating channels that allow for

the swift transport and intercalation of water molecules. Changes from dry (0% humidity) to wet (100% humidity) environments can turn *e*-LBL assembled films from a stiff Parafilm® like material to a soft gel like material with a gooey consistency.

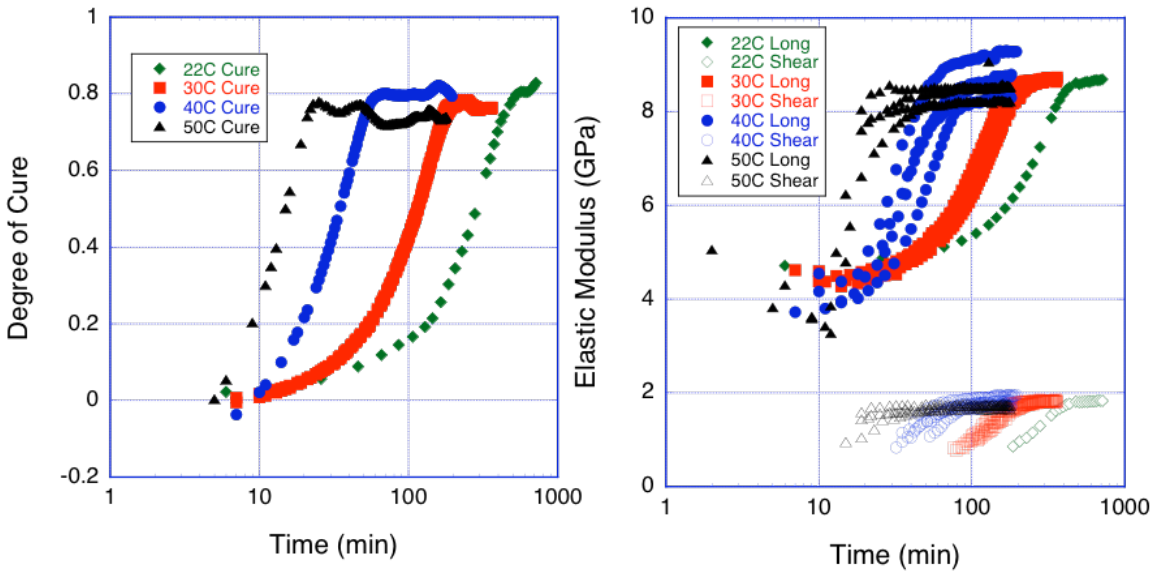

Figure 8.1: Degree of cure and elastic modulus for reactions between DCPD and Grubbs catalyst as a function of curing time; reactions took place at 22, 30, 40, and 50 ºC where the temperature was adjusted using a small furnace.[1]

Although, we believe that this work offers an initial view of the mechanical properties of layered materials, it illustrates the importance of interlayer interactions between the constituents and what it means for the enhancement of their mechanical properties. However, there is much to be discovered in the area of layer-by-layer assembled thin films. In this thesis we briefly explored the effect that using nanoparticles of two different diameters can have on the in- and out-of-plane moduli. More complicated structures can be studied in terms of different particle pairing and varying polymer layer thickness with in a film. It would also be interesting to see the connection between the chemical structures of LBL films and their mechanical behaviors. Aldridge et al. developed a novel concept of relating chemical structure to the elastic modulus of

dicyclopentadiene (DCPD) and Grubbs' catalyst during cure using concurrent Brillouin and Raman scattering, as shown in Figure 8.1.[1] A comparable study would be examine the load transfer between the polymer matrix and particles by monitoring the change in mechanical properties of LBL film as a function chemical changes of a LBL film under uniaxial stress via concurrent Brillouin and Raman scattering. Figure 8.2 shows work on strained carbon nanotube epoxy composite where the G' band is monitored using Raman spectroscopy. The G' band shifts to lower wavenumbers for a sample under tensile stress.[2-4] In a preliminary study we subjected PU/MTM clay films to a uniaxial load and collected Ramam spectra at various degrees of strain. Figure 8.3, shows the appearance of a peak at 1150 cm^{-1}, which increases in intensity as the strain increases. This indicates a change in the chemical structure. Following work by Aldridge, both changes in structure and mechanical properties can be monitored for LBL films under stress using our concurrent RLS/BLS setup.

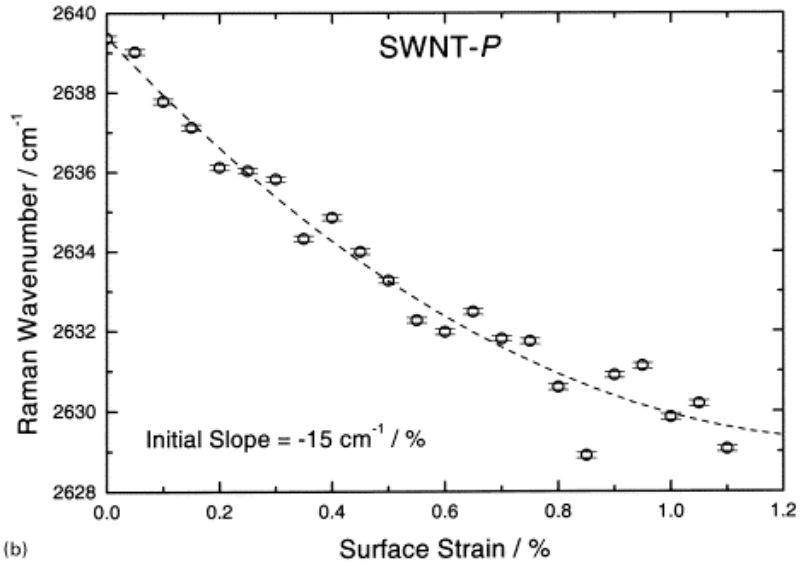

Figure 8.2: Raman shift of the G' peak position of SWNT dispersed in epoxy resin.[2]

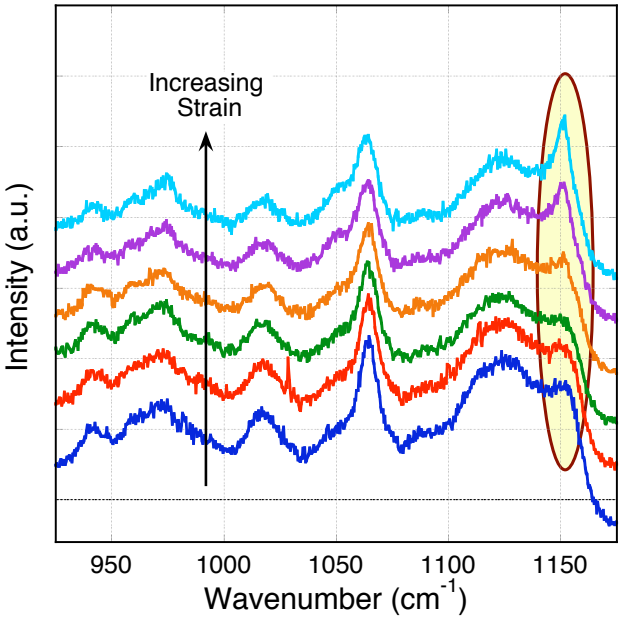

Figure 8.3: Relative elastic modulus PU/MTM clay LBL films as a function of MTM clay volume fraction.

Furthermore, another appealing study is that of the ion transport properties of *e*-LBL assembled films. LBL has been proposed as a fabrication technique for battery electrodes and electrolytes, which depend on the swift transport of lithium ions. This thesis already illustrates the change in elastic modulus of PEO/PAA films as a result of water diffusing out of the system, which is facilitated due to the orientation of polymer chains during the deposition process. The channels so created can also serve to support the transport of lithium ions. In fact the small SiO_2-*f* aggregates may also aid in channeling conducting ions across the membrane and their ion conductivity can be measured using impedance spectroscopy. This may open up new ways for designing and fabricating battery electrolyte materials.

References

[1] Aldridge, M. F.; Shankar, C.; Zhen, C. G.; Sui, L.; Kieffer, J.; Caruso, M.; Moore, J. "Combined Experimental and Simulation Study of the Cure Kinetics of DCPD," *J Comp Mater* **2010**.

[2] Cooper, C. A.; Young, R. J.; Halsall, M. "Investigation into the deformation of carbon nanotubes and their composites through the use of Raman spectroscopy," *Compos Part A-appl S* **2001**, *32*, 401-411.

[3] Ajayan, P. M.; Schadler, L. S.; Giannaris, C.; Rubio, A. "Single-walled carbon nanotube-polymer composites: Strength and weakness," *Adv Mater* **2000**, *12*, 750.

[4] Schadler, L. S.; Giannaris, S. C.; Ajayan, P. M. "Load transfer in carbon nanotube epoxy composites," *Appl Phys Lett* **1998**, *73*, 3842-3844.